Feasibility of Using Lodox to Perform Digital Subtraction Angiography

by

Megan Lilian Van Den Berg

Submitted to the Faculty of Health Sciences at
the University of Cape Town in partial fulfillment of the requirements for the degree of
Master of Science in Medicine in Biomedical Engineering

July 2003
Cape Town, South Africa

Declaration

Feasibility of Using Lodox to Perform Digital Subtraction Angiography:

I, MEGAN LILIAN VAN DEN BERG, hereby declare that:

(a) the above thesis is my own unaided work both in concept and execution, and that apart from the normal guidance from my supervisor, I have received no assistance except as stated below:

(b) except as stated below, neither the substance nor any part of the above thesis has been submitted in the past, or is being, or is to be submitted for a degree at the University of Cape Town or any other university.

The thesis has been presented by me for examination for the degree of Master of Science in Medicine in Biomedical Engineering.

Signed by candidate

Sign= *Signature removed*

31/07/2003

Date

Acknowledgements

I wish to thank the following people for their assistance and guidance – this thesis would not have been accomplished without them:

Professor C.L. Vaughan, Hyman Goldberg Professor of Biomedical Engineering, University of Cape Town, for your constant guidance and encouragement as my thesis supervisor and for all the work you put into this dissertation to make it a success. The amazing way you work with people and your delegation and time management skills have taught me loads - thank you.

African Medical Imaging for funding this project.

Erik Meijering for posting me a copy of your PhD thesis. You were most helpful and generous.

My fellow students in the Biomedical Engineering Department, for their innovative ideas and support and for being incredible "sounding boards" on many occasions (and for insight into fixing my motor car!).

Greg Flash for helping me with all the seemingly endless computer issues and for helping me find legitimate software.

Wayne Nin for helping me with Latex and programming ideas.

Ben Wright for proof-reading and suggestions. For all your encouragement.

Linda Martindale for proof-reading many chapters and for your constant encouragement.

In this particular time of my life I would not be handing in this dissertation if it weren't for the Lord Jesus Christ and His guidance, promises and faithfulness in my life. So thank you God for helping me not panic when I lost everything and for encouraging me through to completion when I felt like giving up and when it seemed so far to the end. Thank you for Your word that is 'life to those that find it and health to all their flesh' and that it is 'active and powerful' and accomplishes what it is sent to do. For putting incredible people into my life.

Cathy van Staden for operation "revive thesis". For bringing me food, praying with me and helping retype the few hard copy chapters found into my new system. You're a star!

Prof Steve Beningfield and Gillan Bowie, Dr Andrew Nicol, Prof Gerhard de Jager and the "Lodox team". The former two for helping me obtain phantoms but everyone for all your generous amounts of time and willingness to offer expert advice when needed.

Lastly but definitely not least: To my wonderful parents for standing by me on this long journey from the very beginning. Thanks for being there and for supporting me in all my decisions and for proof-reading this hefty document, wow!

Abstract

Many cases in trauma involve vessel imaging to determine integrity and the origin of lesions or blockages. Digital subtraction angiography (DSA) is a tool used to improve the clarity of the vessels being imaged for better and easier decision making in diagnostics and planning. Lodox, a low dose x-ray system developed by Debex (Pty) Ltd, a subsidiary of de Beers, was designed specifically for the trauma environment. It therefore follows that, if possible, a function so readily used in trauma, such as DSA, should be added to the imaging repertoire of an x-ray system designed for use in this environment.

In this dissertation the feasibility of using Lodox to perform DSA is therefore explored. In doing so, the requirements of a trauma unit and the theory behind DSA were researched so as to obtain a better understanding into what would be required.

The equipment needed to perform DSA was investigated to determine whether the Lodox system was capable of running DSA with its current technology. The additional components and software necessary for it to do so were established. This was done by comparing the Lodox components with those of two commercially available systems: the Philips Integris Allura; and the Toshiba Infinix VC angiography systems.

A program to perform and test the implementation of a DSA facility was constructed using the relevant theory. Image registration and associated complications such as motion artefacts were the primary concern of such an operation. An algorithm proposed by Meijering (2000) was deemed the most appropriate and was therefore adapted for the purposes of this project. While the program developed is not optimal, it was nevertheless suitable for the purposes of this study.

The results of this dissertation indicate that Lodox, in its present state, is only suitable for acquiring peripheral angiography images. Certain software and hardware enhancements would be needed to enable the actual subtraction to be carried out and displayed on the Lodox console in real time. It also revealed that clinicians are indeed in favour of the addition of a DSA capability to the Lodox system.

Table of Contents

Declaration i

Acknowledgements ii

Abstract iii

Table of Contents vi

List of Figures xi

List of Tables xv

Nomenclature xi

1 Introduction 1

1.1 Problem Statement 2

1.2 Study Overview 3

2 The Trauma Unit and Digital Subtraction Angiography 5

2.1 The specific needs of trauma 5

2.2 Arterial imaging in trauma 6

2.3 What is digital subtraction angiography (DSA)? 7

3 Digital Subtraction Angiography and Associated Technology 10

3.1 DSA system components 10

3.1.1 Fluoroscopic sub-system 12

3.1.2 Image processing sub-system 13

4 Image Quality Assessment Criteria 17

4.1 Image characteristics 17

4.1.1 Spatial resolution 17

4.1.2 Contrast sensitivity 22

4.1.3 Temporal resolution 23

4.1.4 X-ray exposure and dose 24

4.1.5 Noise 26

5 Motion Artefacts Encountered in Digital Imaging 29

5.1 Motion artefacts 29

5.1.1 Examples of motion artefacts 30

5.2 Patient related solutions 33

5.2.1 Choice of contrast media used 33

5.2.2 Holding breath 33

5.2.3 Immobilisation 33

5.3 Acquisition related solutions 33

5.3.1 Dual energy image acquisition 34

5.3.2 Hybrid subtraction 34

5.3.3 Synchronised gating 34

5.4 Retrospective image processing solutions 35

6 Registration and Subtraction 36

6.1 Transformations 37

6.1.1 Global and local transforms 37

6.1.2 Extrinsic and intrinsic methods 38

6.1.3 Optic flow and template matching techniques 38

6.2 Control point selection 41

6.3 Interpolation methods 42
6.3.1 Canny edge detection 45
6.4 Similarity measures 47
6.4.1 Correlation based measures 47
6.4.2 Difference based measures 51
6.4.3 Sign change measures 52
6.4.4 Mutual information 54
6.4.5 Histogram of differences-based measures 54
6.4.6 Displacement interpolation 57
6.4.7 Inconsistency detection and correction 57
6.5 Mask image warping 58

7 Development of the Image Subtraction Program 59
7.1 Program overview 59
7.1.1 Summary 68
7.2 Limitations and comments 70

8 Results 72
8.1 DSA system component comparison results 72
8.1.1 Commercial systems 73
8.1.2 Lodox 75
8.1.3 System comparison 81
8.2 Blood flow velocity 84
8.3 Phantom and Patient trials 85
8.3.1 Phantom trials 85
8.3.2 Patient trial 90
8.4 Questionnaire to clinicians familiar with Lodox 97

9 Discussion 102
9.1 Lodox and the needs of trauma 102

9.2 Lodox and DSA system components and imaging characteristics . . . 105
9.2.1 The Generator . . . 105
9.2.2 Analogue-to-digital converter (ADC) and its sampling frequency 106
9.2.3 The image processor . . . 107
9.2.4 The digital viewing station (DVS) . . . 107
9.2.5 Storage . . . 108
9.2.6 Temporal Resolution . . . 108
9.2.7 Noise . . . 109
9.2.8 Blood flow velocity . . . 109
9.3 Registration approach . . . 110
9.3.1 Similarity measures . . . 111
9.4 Program and results . . . 111
9.4.1 Phantom trials . . . 113
9.4.2 Patient trial . . . 115
9.5 Speed and efficiency of the program . . . 117

10 Summary **119**

Appendix A Component Details **122**
A.1 X-ray tube . . . 122
A.2 Image intensifier . . . 123
A.3 Scintillators . . . 124
A.4 Computed Radiography (CR) . . . 124

Appendix B Time-delayed Integration **125**

Appendix C Gross Translational Correction Testing **127**

Appendix D Crop Results Using Two Border Widths **131**
D.1 Automatic crop results . . . 131

D.1.1 T-tube tests 131
D.1.2 Femoral phantom tests 134
D.1.3 Patient trial tests 136
D.2 Manual crop results 137
D.2.1 T-tube tests 137
D.2.2 Femoral phantom tests 140
D.2.3 Patient Trial tests 142

Appendix E MTF curves for Lodox **145**

Appendix F Case Report Study **146**

References **150**

List of Figures

2.1 Angiogram of a hand 8
2.2 The DSA principle 9

3.1 DSA system block diagram 12

4.1 PSF and spatial resolution 18
4.2 The point spread density function 19
4.3 Edge spread function 20
4.4 MTF examples 20
4.5 Geometric unsharpness 21
4.6 Contrast sensitivity 23
4.7 X-ray dose measurements 25
4.8 SNR examples 27

5.1 Artefacts2 31
5.2 Worst case introduction of artefacts 32
5.3 Artefact examples 32

6.1 2-D transforms 38
6.2 Template matching concept 40
6.3 Regular grid method 41
6.4 Control point selection 42
6.5 Subpixel interpolation using bilinear interpolation 43

6.6 Triangulation example 44
6.7 Two triangulations 45
6.8 Correlation template 48
6.9 Correlation 49
6.10 Difference of histogram method 56

7.1 Program overview 60
7.2 Original image 61
7.3 Cropped images 62
7.4 Cropped and initial subtracted image 62
7.5 Bordered images 63
7.6 Region allocation 63
7.7 Border and edge points 64
7.8 Processing templates found 65
7.9 Final control point selection 66
7.10 Displacement vector correction 66
7.11 Displacement vector finding process 67
7.12 Displacement vector illustration 67
7.13 Delaunay triangulation 68
7.14 The warped mask image 69
7.15 The final subtracted image 69
7.16 Images using smaller borders 71

8.1 Commercial systems 73
8.2 The Lodox system 76
8.3 The Lodox system block diagram 77
8.4 Timing diagram 78
8.5 T-tube phantom 86
8.6 T-tube images 86

8.7 Initial subtraction of the T-tube images 87
8.8 (The final subtracted T-tube image 87
8.9 Phantom of the femoral head 88
8.10 Unprocessed subtracted femoral image 89
8.11 Trauma patient images 91
8.12 Patient trial image comparison 92
8.13 Magnified image from the patient study 93
8.14 Initial unprocessed subtracted patient trial image 94
8.15 Contrast and subtracted image comparison 95
8.16 The surgical procedure 96

A.1 X-ray tube 123
A.2 Image intensifier 123

B.1 TDI illustration 126

C.1 Translation test images 127
C.2 Shifted translation test images 128
C.3 Results of translation test1 129
C.4 Results of translation test 2 130

D.1 T-tube automatic crop test images 131
D.2 Automatic Crop Results 1 132
D.3 T-tube automatic crop results 2 133
D.4 Femoral phantom automatic crop test images 134
D.5 Femoral phantom automatic crop results 135
D.6 Patient trial automatic crop test images 136
D.7 T-tube manual crop test images 1 137
D.8 T-tube manual crop test images 2 138
D.9 T-tube manual crop results 1 139

D.10 Femoral phantom manual crop test images 140
D.11 Femoral phantom manual crop results 141
D.12 Patient trial manual crop test images 142
D.13 Patient trial manual crop results 143

E.1 MTF value graphs for Lodox 145

List of Tables

4.1 X-ray dose rates 26

7.1 Parameter values 64

8.1 Acceptable dose rates 80

8.2 DSA system comparisons 81

8.3 Blood flow velocity values 84

8.4 Program timing results 97

D.1 Program timing comparison 144

Nomenclature

ADC	Analogue-to-Digital Converter
ASD	Absolute Sum of Differences
CBC	Coincident Bit Counting
CC	Cross Correlation
CCD	Charged Coupled Device
CR	Computed Radiography
DAC	Digital-to-Analogue Converter
DFT	Discrete Fourier Transformation
DICOM	Digital Imaging and Communication in Medicine
DSA	Digital Subtraction Angiography
DSC	Deterministic Sign Change
DVS	Digital Viewing Station
EHD	Energy Histogram of Differences
ENT	Entropy of the Histogram of Differences
ERA	Emergency Room Angiogram
FDA	Food and Drug Administration
FEP	Front End Processor
FFT	Fast Fourier Transform
fps	Frames per second
GSH	Groote Schuur Hospital
IPP	Image Pre-Processor
LACT	Limited Angle Computed Tomography
MP	Medical Prototype
MTF	Modulation Transfer Function
NCC	Normalised Cross Correlation
OC	Operator Console

PACS	Picture Archiving and Communication System
pdf	Probability Density Function
PSF	Point Spread Function
ROI	Region of Interest
SID	Source to Image Receptor Distance
SNR	Signal-to-Noise Ratio
SR	Shift Register
SSC	Stochastic Sign Change
SSD	Sum of Squared Differences
TDI	Time-delayed Integration
TID	Time-interval Difference
VOD	Variance of Differences

Chapter 1

Introduction

Lodox-MP (Medical Prototype) is an imaging system specifically developed for use in emergency medical centres by Debex (Pty) Ltd, a subsidiary of De Beers South Africa. Its uniqueness lies in its ability to produce high definition x-rays at a considerably lower radiation dose from that of conventional and other digital x-ray machines currently available. It was originally produced to perform a full body scan in a short time span of under 14 seconds. Its attributes therefore address many of the needs of a desired trauma system in that it offers a means to rapidly acquire a low dose, high quality, x-ray image with equipment that is simple to operate and DICOM (Digital Imaging and Communication in Medicine) compatible. Because of its low dosage x-ray capability, it is also highly suitable for paediatric use.

Angiography is a procedure that is extensively used in trauma to ascertain the integrity and patency of vessels and the location of lesions or stenoses to serve as a guide for surgical planning. Vessel imaging is however not as straight forward as one would like since the vessels exhibit similar imaging characteristics to their neighbouring structures. Consequently, differentiation between these structures is not always discernible even to a trained eye. To compensate for this, the vessels' contrast characteristics are enhanced relative to their environment by the introduction of a radio-opaque dye into the lumen. The resulting angiographic image is then subtracted from an image taken prior to the influx of this contrast enhancing medium and the difference should ideally show only the vessels of interest. This procedure is referred to as Digital Subtraction Angiography (DSA). The ideal scenario is rarely if ever achieved without further mathematical processing, and the resultant images are generally lit-

tered with artefacts due to slight differences between the images concerned. One of the major contributors to these differences is patient motion. DSA, therefore, allows for even clearer vessel imaging in that the background information is subtracted from this contrast image so that structures such as bone do not obscure the view of the vessel that is of interest to the clinician.

Often quick decisions have to be made concerning a patient and his surgical needs. The imaging modalities employed to help determine these needs are often inundated with other patients of equal need and time is therefore absolutely crucial. A system that could accommodate the criteria associated with quick and efficient decision making would help those in the health care profession to more readily and accurately determine the target areas for treatment and surgery. This would in turn facilitate better patient outcomes which Gaines (2001), MacFarlane *et al.* (1989) and O'Gorman *et al.* (1984) have stressed are directly related to the degree of prompt vascular management delivered.

This thesis therefore draws these concepts together by investigating the feasibility of using the Lodox system to perform DSA and to ascertain what would be required in order for it to do so successfully.

1.1 Problem Statement

This thesis serves as a feasibility study into whether Lodox – a low dosage x-ray machine – is currently able to perform digital subtraction angiography. The following points therefore need to be investigated:

- Determine whether a DSA facility would be helpful in the trauma unit and whether it would in fact be used.
- Determine the requirements in a conventional DSA system in terms of its equipment components and decide whether the Lodox system needs hardware and software enhancements in order to perform this task
- Develop a prototype program, using Matlab, to implement digital subtraction to determine whether acquisition and subtraction can in fact be implemented.

1.2 Study Overview

This study describes the basic components, necessary programming techniques and algorithms needed to enable the implementation of a DSA facility in the Lodox system. The first six chapters provide a review of the literature and theory related to DSA. Chapter 7 describes the program developed to implement the theory and Chapter 8 outlines the results of the various studies relating to DSA technology, imaging characteristics, the trial results and responses of clinicians to a questionnaire. Chapter 9 provides a discussion on the results while Chapter 10 outlines the various conclusions in a summary of the dissertation.

Chapter 2 focuses on the requirements necessary for the system to be trauma specific and provides a description of the process of digital subtraction angiography (DSA). It also gives some insight into how clinicians categorise various arterial occlusions, many of which are more readily treated with the aid of DSA. Chapter 3 describes a generic DSA system with regards to the components and in Chapter 4, the variables used to assess image quality and those that interfere with it are presented. Chapter 5 discusses the artefacts often encountered due to patient motion and offers various solutions to minimise these effects. If good registration is not obtained prior to the subtraction process, artefacts may be introduced into the final image. The concepts used in solving the registration problem between two images therefore follows in Chapter 6. Here, transformation development, the methods used to decrease processing time, and the choice of similarity measure used in the matching algorithm explored by various authors, are described. The program developed using these concepts is outlined in Chapter 7.

Chapter 8 may essentially be divided into two main sections. The first addresses the component comparison and the second, the results obtained through the trials conducted. The first section therefore documents the specifications of three commercial systems – the Philips MCM80, the Philips Integris Allura and the Toshiba Infinix VC – that offer DSA capabilities and compares them with the Lodox system. In the second section, the results of the trials conducted, the methods and images obtained are set out. Answers to a questionnaire follow. This was aimed at clinicians who are familiar with the Lodox system and have had some experience with conventional DSA or angiography.

Chapter 9 provides a discussion on the findings of this dissertation. In it, the Lodox system is further compared with the angiography systems described in Chapter 8 while the needs of trauma and whether DSA would be a feasible facility to incorporate into Lodox are drawn together. The various similarity measure options are summarised, and the specific one relating to the difference of histograms measure is justified. Finally in Chapter 10 the conclusions and recommendations regarding the feasibility of incorporating DSA into Lodox are presented, followed by a summary of possible future research options.

Chapter 2

The Trauma Unit and Digital Subtraction Angiography

2.1 The specific needs of trauma

The trauma environment is one that offers 24 hour care for severely injured patients or those at risk from severe injury. The time constraints imposed on decision making and patient turnover therefore necessitate equipment that can operate in a variety of orientations and configurations, is easy to operate – not requiring extensive training beforehand – and offers real time displays of high resolution images that are DICOM compatible. Beneficial additions would include low radiation exposure rates to the patient and especially to the attending medical staff (see Dr Nicol's response in Section 8.4), as well as equipment that is suitable or adjustable to paediatric monitoring. The less the patient has to be moved to obtain all the relevant information relating to his or her current status, the better. A machine that can therefore perform multiple tasks is preferred.

2.2 Arterial imaging in trauma

The GSH (Groote Schuur Hospital) Trauma surgeons subdivide an arterial occlusion into three main groups: viable, non-viable and the threatened limb (Nicol, 2002). Each condition has specific clinical signs and treatment protocols associated with it.

The viable limb exhibits signs of normal sensation and function, is warm with a palpable or doppler found pulse, and usually requires standard radiographical treatment, for which the patient is able to wait. Non-viable injuries often display signs of gangrene, muscle rigor and/or skin staining. These injuries often lead to amputation of the necrosed tissue (Nicol, 2002; Rutherford *et al.*, 1995; Shackford and Rich, 1996).

It is the third of these groups, the threatened limb, that is of interest in this study. In the case of the threatened limb, there is normally a critical period of four to six hours in which the limb can be successfully treated before necrosis sets in (Skinner and Whimster, 1999; Norton *et al.*, 2001). The clinical signs include pain, decreased sensation and a loss of function. The limb is usually cold and pale with no indication of a pulse – either by palpation or with the use of doppler imaging technology (Skinner and Whimster, 1999; Norton *et al.*, 2001). It is when the patient injury falls into this category that the patient is sent to the operating theatre and an on-table Emergency Room Angiogram (ERA) is needed.

An ERA uses a manual single-contrast injection technique so that vessels of interest are made more visible, thus providing a map for the planning of surgical management. In some cases the complications may be obvious, for example with signs of ischaemia and gross haemorrhage. In other cases the complications may be more evasive, such as vasoconstriction or hypothermia. The ERA technique is helpful in identifying sites of vascular injury prior to exploration.

O'Gorman *et al.* (1984); Itani *et al.* (1992) and MacFarlane *et al.* (1989) all recommend the use of ERA in the trauma unit to evaluate the condition of patients with potential peripheral vascular injuries. They found it accurate and safe with the advantages of speed and low cost when compared with standard angiography. They also found the process did not interfere with other resuscitative, diagnostic and therapeutic procedures. It took only 5-10 minutes to perform and it was simple enough so as not to require trained physicians or technicians to carry out the procedure.

They reported that the availability of an ERA facility resulted in decreased patient queues and post angiogram hospitalisation. This therefore allowed for increased patient turnover and minimised the need to move a patient to an angiography suite for imaging; the patient could potentially be a multi-trauma case on life-support therapy with all the associated equipment that would have to accompany them to any angiography suite for imaging.

The trauma unit at Johannesburg Hospital, South Africa, introduced this technique in mid-1986 (MacFarlane *et al.*, 1989) where they found it was adequate in demonstrating traumatic vascular pathology. They also emphasised its usefulness in secondary and tertiary hospitals – peripheral centres that are without surgical services – to assess whether or not and how rapidly a patient should be transferred to another hospital for treatment.

2.3 What is digital subtraction angiography (DSA)?

Angiography is the radiographic procedure utilised in imaging vessels in the human body. Visualisation of vessels *in situ* has always proved an arduous task since they exhibit similar imaging characteristics to their surrounding structures. They are therefore not sufficiently differentiable from their environment for the purposes of diagnosis and surgical planning. Robb and Steinberg (1939) recognised this in their attempts to perform angiography using intravenous injections of contrast medium into the blood. They used the radio-opaque properties of this contrast medium to enhance the vessels for better visualisation of the cardiovascular system (Crummy *et al.*, 1980). Figure 2.1 illustrates an early angiogram of a hand taken in 1896 by Mr Haschek and Dr Lindenthal with the post-mortem injection of Teichmann's mixture, which consists of lime, cinnabar (mercury) and petroleum (Trevert, 2001; Goodman, 2002).

Better visualisation has since been made possible with the introduction of digital imaging. This has provided a way to perform Digital Subtraction Angiography (DSA). In this process, two images taken at different time intervals but of the same region of interest are subtracted from each other. The results are such that most of the information that is common to both images is removed.

Figure 2.1: An early angiogram of a hand (Trevert, 2001; Goodman, 2002).

In conventional DSA, the first image captured, hereafter referred to as the *mask* image, is scanned in a similar manner to a conventional x-ray image exhibiting the same information. Thereafter, contrast medium in the form of an iodine-based radio-opaque dye is injected either directly into the vessels of interest or via a more accessible entry point. These entry points could include the femoral artery or another superficial vessel close to the region of interest, should the specific area be inaccessible. After the injection of contrast, the bolus of solution is then 'tracked' by a series of x-ray exposures (frames) in which the vessels of interest are highlighted as the contrast medium flows through them. An automatic contrast injector is synchronised to the x-ray generator control to ensure that exposures will commence at a preset time after the injection is made.

The rate at which the bolus moves is determined by the blood flow rate and this in turn is determined by the vessel's location relative to the heart, its integrity and whether it is an artery or vein.

The second set of scans produce a series of images, hereafter referred to as the *contrast* or *live* images. They are compared to the mask image and the most suitable image is selected, this being the one which contains the most similar background information to that of the mask. The mask image is then spatially aligned with the second or contrast image and the two are subtracted.

The desired outcome is that the detail common to both images would be eliminated while the vessels containing the contrast medium would be enhanced. The ideal

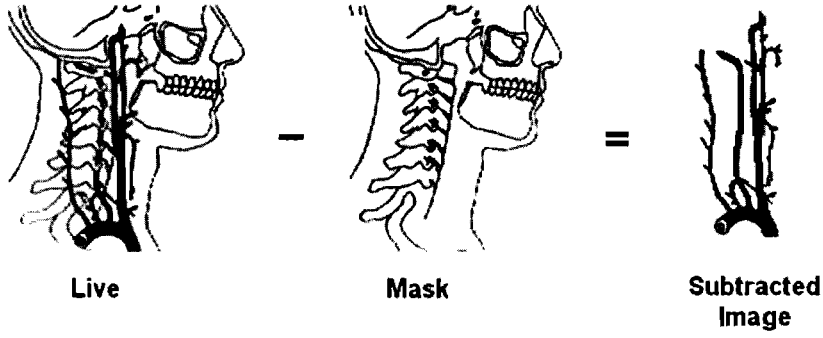

Figure 2.2: The basic principle of DSA (Sprawls, 1977).

scenario is illustrated in Figure 2.2 where the mask and contrast subtraction yields only the vessels of interest. This is however rarely ever encountered in practice and so extensive research into this area of registration and image matching has ensued (Crummy *et al.*, 1980; Harrington, 1982; Sprawls, 1977).

Chapter 3

Digital Subtraction Angiography and Associated Technology

As introduced in the previous chapter, digital subtraction angiography (DSA) essentially involves the acquisition and subtraction of two images - the mask and contrast images. DSA is an added function that is part of a standard angiography system. It is not found as a stand-alone system. In this chapter, angiography systems and their components used by the DSA function to acquire and subtract images are investigated. These will be referred to as components of a *DSA system* for convenience.

3.1 DSA system components

A description of the basic system components follows but, prior to this, the different scanning modes that have been used in the literature will briefly be discussed. This answers the question of how the contrast images are captured during a DSA scan. There are three standard processing modes found in DSA systems: serial or pulse mode, continuous mode and time-interval difference mode.

Serial or pulse mode is the most common mode used in DSA. It involves a series of short x-ray exposures at an image repetition rate of one to four frames per second (fps). This mode produces relatively low quantum noise (refer to Section 4.1.5) and minimal patient and organ motion artefacts.

The second mode is continuous or fluoroscopic mode but, since it is rarely used, this feature is no longer offered by some manufacturers. It involves images being acquired at relatively low, continuous doses at a frame rate of about 30 fps. As in serial mode, each post-injection image is subtracted from the pre-injection image or mask. Continuous x-ray exposures and the relatively low number of x-ray photons result in noisier images with poorer contrast resolution than those obtained through the serial mode. However, this approach is necessary for studies involving dynamic processes and rapidly moving anatomic structures such as the heart.

The third is Time-interval Difference (TID) mode. TID mode imaging differs from continuous and serial mode imaging in that successive images are subtracted from the previously scanned image instead of from a pre-injection mask. Each image is subtracted from a continuously updated mask corresponding to the time variations in the area of anatomy. The primary use of TID-mode imaging is to display structures, such as the heart, that are rapidly changing with respect to the flow of contrast media.

Despite the continual increase in system complexity, subtraction of the image 'background' remains a function of primary importance in any DSA system. The quality and limitations of each component of the system may vary among machines from different manufacturers, but all essentially perform the same task of image acquisition and subtraction to reveal the vessels of interest.

A typical DSA system is made up of two main sub-systems: the fluoroscopic sub-system where image acquisition takes place, and the image processing sub-system. This is illustrated in the block diagram of Figure 3.1. The fluoroscopic sub-system consists of an x-ray generator and tube, an image intensifier and television system. The image processing sub-system is made up of an analogue-to-digital converter (ADC) and preprocessor, a viewing console and image storage facility. Manipulation and enhancement of digital images are carried out manually by the clinician on the viewing console and are subsequently saved to disk or developed onto film (Cohen *et al.*, 1982; Harrington, 1982; Ovitt *et al.*, 1980).

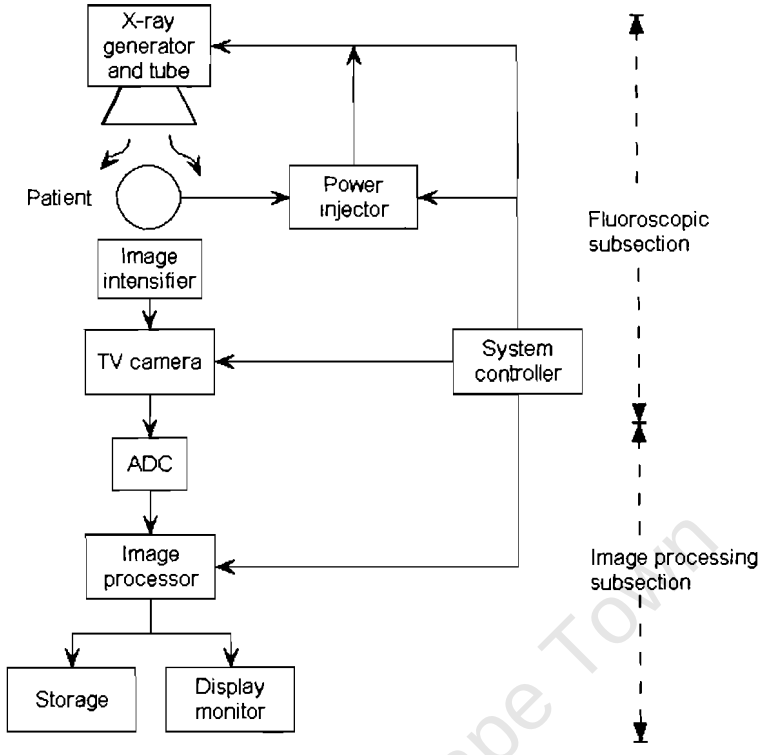

Figure 3.1: A basic block diagram of a typical standard DSA system.

3.1.1 Fluoroscopic sub-system

X-ray generator and tube

The x-ray generator supplies electrical power to the x-ray tube, the x-ray tube cooling unit and the motor of the rotating anode (provided one is present). It also provides accurate feedback of the x-ray tube current and voltage values required to ensure effective dose regulation and safe operation (Harrington, 1982). The basic theory behind x-ray tubes is described in Appendix A.

Image intensifier

A description of an image intensifier is also contained in Appendix A. The image intensifier converts the x-ray beam into a light image. The spatial resolution (see Section 4.1.1) and low contrast detectability are dependent on and therefore influenced by the thickness and composition of the intensifier's entrance screen (Siebert,

2002). The light produced by the intensifier is proportional to the amount of remnant x-ray photons. A diaphragm is used to control the amount of light reaching the television cameras from the image intensifier, thus preventing either inadequate lighting or saturation from occurring.

Television system

Image quality is dependent on the performance of the entire imaging chain (from the x-ray generator, image intensifier and TV camera to the computer and hard-copy device). The resolving power of the TV camera is, however, a major factor limiting image resolution. The television chain produces an intensified electronic video signal proportional to the number of x-rays that exit the patient. Because noise can degrade a signal and subtraction studies are usually performed on low-contrast images, it is imperative that electronic noise obtained through x-ray photon intensity fluctuations (quantum mottle) and the television chain (electronic noise) are minimised. The TV chain of a DSA system must therefore exhibit low lag and low noise characteristics. Excessive lag would produce 'ghosting' which are effectively artefacts produced as a result of the superposition of the present image information with that of a previously scanned image (Kaut-Roth and Faulkner, 2002; Harrington, 1982).

The amplified TV signal is subsequently sent to the image processing sub-system where the analogue images are converted to digital images that can be manipulated and stored.

3.1.2 Image processing sub-system

The analogue-to-digital converter

An analogue-to-digital converter (ADC) converts the analogue images obtained from the TV chain into digital form so that the image can be temporarily stored in digital memory or manipulated by the computer for display on the video monitor. The number of x-ray photons incident on the image intensifier during a scan are represented as

a voltage in the video signal. This voltage is used by the ADC to determine the individual pixel values in the digital image.

The efficiency of an ADC is determined by its conversion time (rate of conversion - μs) and its depth of digitisation (intensity resolution). The latter is related to the number of grey levels that it is capable of displaying. For example, systems may provide 256 (8 bits) or 1,024 (10 bits) grey levels (Harrington, 1982).

The sampling rate of the ADC determines the spatial resolution of the system. The size of the pixel matrix used to capture the image controls the sampling rate of the ADC. For example, if a 512 x 512 pixel matrix is used to digitise an image acquired at a rate of 30 frames per second, the sampling period of the ADC is 1/30 divided by 512^2 which gives approximately 100 ns. This corresponds to a sampling frequency of 10 MHz which limits the bandwidth of the system to 5 MHz. The incoming video signal will then need to be filtered by a low-pass anti-aliasing filter in the pre-processor to limit it to no more than 5 MHz (Lancaster, 2003).

An ADC generally has its own dedicated hardware to ensure an adequate digitisation rate. Increased frame-rates may be made at the cost of spatial resolution (Ovitt *et al.*, 1980).

Image pre-processor and viewing station

The image pre-processor (IPP) receives the uncorrected image from the ADC and processes and corrects it, removing all artefacts associated with the acquisition process. The registration and subtraction of images are performed here. The images obtained are then transmitted to a viewing station and to the database for storage.

The viewing station provides a facility to clinicians responsible for making the diagnosis. It displays the diagnostic information and allows for the manipulation of image features and easy image storage and access. Some of the manipulation features include window and level adjustments, edge enhancement, landmarking, image reregistration, image zoom, pixel shifting and a roadmap fluoroscopy capability. This list is by no means exhaustive but it encompasses the most common functions found in most angiographic systems (Philips Medical Systems, 1989; Harrington, 1982). A description of each of these feature functions follows:

Window and level adjustments: This is the simplest method of image manipulation. Variations in window level and width of the displayed image produce variations in the density and contrast of the image respectively.

Edge enhancement: Edge enhancement allows for better visualisation of small details by applying a high-pass filter to the image. This emphasises the edges of the image.

Landmarking: Mask image information (background information) is superimposed on the subtracted image to assist the radiologist to orientate himself or herself in preparation for invasive procedures.

Image reregistration: This manually operated tool helps to register the image in the event of misalignment between the mask and contrast images, thereby eliminating certain motion artefacts.

Image zoom: Image zoom allows for image magnification of a region of interest without varying the detail visibility.

Pixel shifting: This is used in the event of unacceptable patient motion between images.

Roadmap fluoroscopy: A roadmap fluoroscopy capability is mandatory for many procedures. Clinicians use it to guide them in their progress in inserting a catheter into a vessel. In this procedure a vascular path is tracked by injecting small amounts of contrast medium into the vessel and then running a continuous real-time fluoroscopy scan at low resolution. In these acquired images the catheter and contrast filled artery (or space in which the opening of the catheter lies) appear on the monitor.

Archiving of DSA images

Various systems offer different storage means. These may include hard or floppy drives, optical disks, magneto-optical disks (MODs), digital videotape recorders, magnetic tape cassettes, Digital Versatile Disks (DVDs), write-once read-many (WORM) and recordable compact disk (CD-R) drives. Some systems may be interfaced with a Picture Archiving and Communication System (PACS). Digital-to-analogue converters (DACS) are then utilised in order to convert the image into a video signal for display

on a TV monitor. Hard-copy x-ray films can be made on a multi-image camera or a laser imager.

Although the main components of a DSA system have been described briefly, it would not be complete if the automatic pressure injectors were not mentioned as these form an integral part in obtaining suitable images.

Automatic pressure injectors

To perform a typical bolus chase, contrast medium needs to be injected into the vessels at a preset rate. This ensures that it does not completely dissipate throughout the blood while the injection is still in progress, causing contrast dilution in the vessel which leads to unclear images and renders the imaging event obsolete. Automatic pressure injectors are used for this purpose. They not only provide a consistent and repeatable injection pressure for adequate bolus chasing, but they help to prevent inadvertent damage to the patient and catheter (Kaut-Roth and Faulkner, 2002). These injectors are linked with the generator so as to synchronise the start of x-ray emission with the injection of contrast medium into the vessel.

Chapter 4

Image Quality Assessment Criteria

4.1 Image characteristics

There are multiple ways of measuring image quality but no single gold standard exists. Quantifying it involves a compromise between image quality and dosage required knowing that better detectability is associated with higher x-ray fluxes (Schindehutte *et al.*, 1998; Lease, 2001; Brown *et al.*, 1999). Optimisation therefore necessitates a compromise between the parameters of signal-to-noise ratio (SNR) and resolution. In this section some of the major parameters affecting image quality are described. These include contrast sensitivity, spatial resolution, temporal resolution, x-ray exposure, dose rates and noise. Blood flow velocities will also be discussed as they relate to DSA in this study.

4.1.1 Spatial resolution

Spatial resolution is related to image sharpness. It is a measure of how well a system can record fine detail (ECRI, 2001; Harrington, 1982). For example, systems exhibiting low spatial resolution characteristics produce images with blurred structural boundaries, rendering two objects in close proximity in that image as one.

The matrix in an image processor consists of an array of pixels – the smallest element of an image. Spatial resolution is determined by the system's pixel size and is

expressed as a measure of the number of line pairs per millimetre (lp/mm) that are distinguishable. In order to determine the system's resolution, the matrix size must be considered in conjunction with the image intensifier. For example, if the field size of an intensifier is 15 cm (6 inches) in diameter and the matrix size is 512 x 512 then there are 3.3 pixels/mm or 1.6 lp/mm (Harrington, 1982).

Spatial resolution is measured using various methods. The most common are: the Point Spread Function (PSF), the Edge Spread Function (ESF) and the Modulation Transfer Function (MTF) (Smith, 1999; Nicer, 2003; de Villiers and de Jager, 2002).

The point spread function (PSF)

(a) (b) (c)

Figure 4.1: PSF and spatial resolution (Lancaster, 2003).

In the spatial domain, the PSF describes the degree to which an optical system blurs (spreads) a point of light. Therefore, the more concentrated the 'spot' in the image, the higher the resolution. Figure 4.1 illustrates three different point spreads. An ideal spot image as shown in Figure 4.2(a) with its profile plotted in Figure 4.2(b). Figures 4.2(c) and 4.2(d) show a non-ideal spot image and its profile respectively. These profiles provide a 1-dimensional PSF of each image. The resolution is defined by the width, w, in Figures 4.2(b) and 4.2(d), of the curve at the position where the PSF drops to half its maximum value (full width half maximum – FWHM) (Nicer, 2003; Lancaster, 2003; de Villiers and de Jager, 2002). The contrast with which an object is represented decreases as the object size approaches the FWHM (Lancaster, 2003).

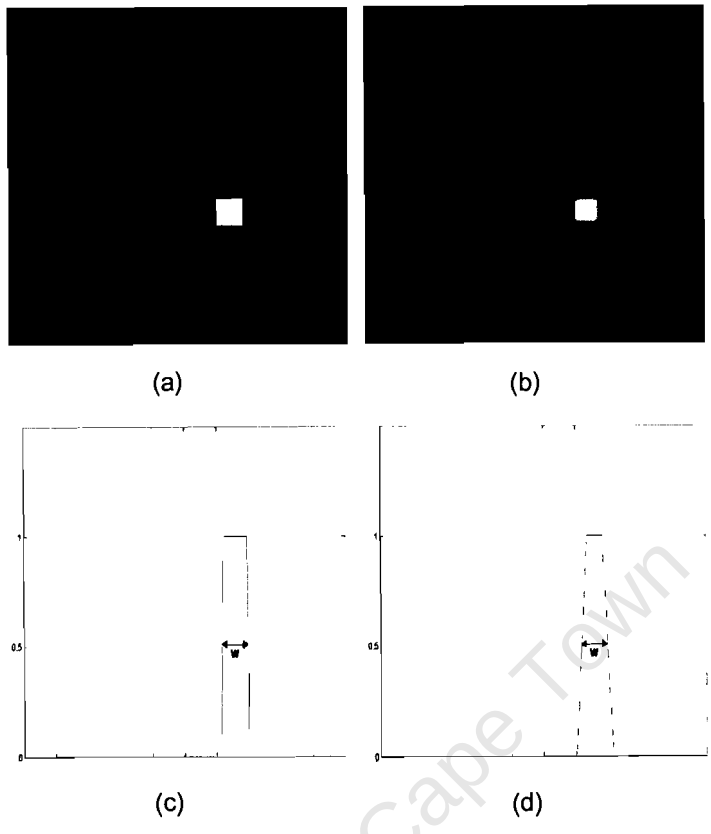

Figure 4.2: The point spread density function. (a) an enlarged ideal point source; (b) a non-ideal point source; (c) the profile of the ideal point source in (a); and (d)the profile of the non-ideal point source in (b).

The edge spread function (ESF)

The ESF is related to the PSF. It differs from it in that it considers an image of an ideal step function rather than an ideal point (depicted in Figure 4.3). As with the PSF, profiles can be drawn orthogonally through the line image and the resolution, at a specific point and direction, may be found using the width at half its maximum value (FWHM) (Nicer, 2003; Lancaster, 2003; de Villiers and de Jager, 2002).

(a) (b)

Figure 4.3: The edge spread function (ESF). (a) an ideal case; and (b) a non-ideal case.

The modulation transfer function (MTF)

The MTF is the magnitude of the Fourier transform of the PSF. It is therefore used to assess the overall spatial resolution of the imaging system by describing the change in contrast as a function of spatial frequency (Smith, 1999; Lease, 2001; Lancaster, 2003). As a measure it enables different systems to be readily compared – the better system providing the higher MTF. The MTF is expressed as a value in the range of 0 to 1 (optimal value) in spatial frequency units of 1/cm. For example, it usually starts at a value of 1 at 0 spatial frequency which represents a homogeneous background, and drops off in a system-specific manner to zero. An example of what the MTF measures can be seen in Figure 4.4. From this figure the concept of the MTF can be better understood as the measure of the amount of contrast that can be maintained by an imaging process that is performed at a specific resolution (Lancaster, 2003).

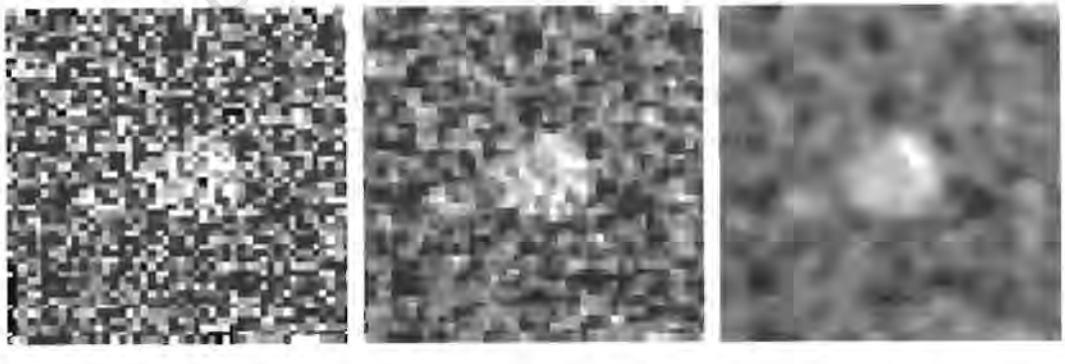

(a) (b) (c)

Figure 4.4: MTF where (a) is the results of a high MTF, (b) of a medium and (c) of a low MTF (Nicer, 2003).

Low spatial resolution may be due to a combination of factors (Harrington, 1982; Lease, 2001; Sprawls, 1977; Lancaster, 2003): patient motion, which is particularly pronounced with prolonged exposure time causing motion blurring; geometric blurring (intensity distribution) or receptor blurring.

Geometric blurring (intensity distribution)

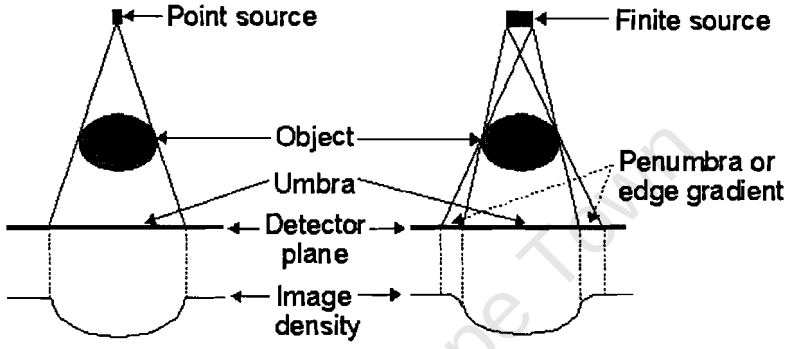

Figure 4.5: Geometric unsharpness is the loss of detail due to blurring by the x-ray tube focal spot. The umbra is the completely shadowed region behind the object, while the penumbra is the partially shadowed region surrounding the umbra (Lancaster, 2003).

Geometric blurring is caused because x-rays are emitted from an area source rather than a point source resulting in diffuse edges.

These blurred regions are referred to as penumbra, the magnitude of which is determined by the focal spot size and source-to-image receptor distance (SID). Maximising the distance between the focal spot and the object, and minimising the distance between the object and the image receptor, reduces geometric blurring (Lease, 2001; Hering, 1990; Nicer, 2003). This phenomenon is illustrated in Figure 4.5.

Receptor blurring

In digital systems receptor blurring results from signal diffusion between elements, the active area of elements and the pitch (centre to centre spacing) between elements. In screen-film radiography, light is usually spread by a screen before it is recorded.

Phosphor layer thickness and phosphor particle size, dye and pigment content in the screen (causing light absorption) and the screen film content therefore influence receptor blurring in this case (Lease, 2001; Sprawls, 2002).

According to Schindehutte *et al.* (1998), estimates of minimally acceptable numbers of line pairs per millimetre (lp/mm) for systems have varied from 2.5 lp/mm to over 10 lp/mm, depending on the views of the experts in the field concerned. Current computed radiography (CR) (see Appendix A) plate readers typically yield images with a 2.1 lp/mm spatial resolution and some good film screen systems have doubled or even quadrupled that resolution. Some CR plates can yield 5 lp/mm resolution from 35 x 43 cm (14 x 17 inch) plates with improvements as the size decreases. Pixel sizes of 50 μm (providing a resolution of 10 lp/mm) have also been achieved (Schindehutte *et al.*, 1998).

4.1.2 Contrast sensitivity

Contrast resolution is a measure of a system's ability to produce images in which one can distinguish small intensity differences. This measure is therefore based on the relationship between a region (or pixel) of interest and its surroundings (or neighbouring pixels). The more grey levels a system is able to record the better the resolution obtainable. For example, by increasing the image matrix size from 512 x 512 pixels to 1024 x 1024 pixels, the contrast resolution can be greatly improved, but this however entails storing four times more data. For imaging systems, this then requires a disk drive with greater capacity and a TV camera and monitor that can accommodate a substantially larger image. The dose must also be increased by a factor of four in order to maintain the same signal-to-noise ratio (SNR).

In a radiograph, the contrast between structures is dependent on the difference in their thickness, their density, their effective atomic numbers as well as the energy of the x-ray beam. The contrast values in a digital radiograph are not as important as in film radiography because, in the former case, images are digitised into numbers of grey levels. This allows for contrast enhancement by adjusting settings such as the window levels and width display (refer to the section of the image processing subsystem in Chapter 3) (Schindehutte *et al.*, 1998; Lease, 2001; Nicer, 2003; Hering, 1990).

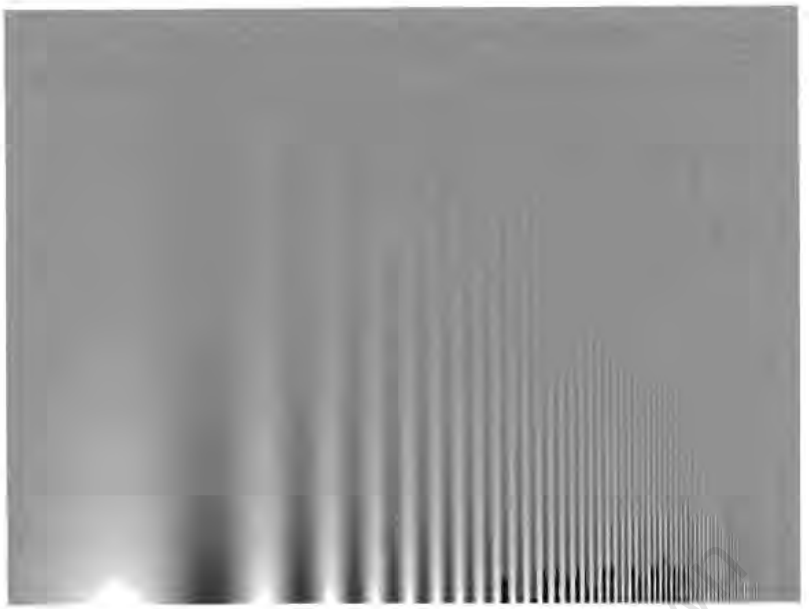

Figure 4.6: Contrast sensitivity variations (Campbell and Robson, 1968).

In Figure 4.6, the contrast is sinusoidally varied in the horizontal direction with peaks and troughs remaining constant along a given horizontal path through the image. The contrast is also logarithmically varied from 100% at the bottom to about 0.5% at the top. The spatial frequency is increased exponentially from left to right. It is therefore noted that the detection of contrast is not solely dictated by image contrast. If this were the case, the alternating bright and dark bars would appear to have equal height everywhere in the image. The bars, however, appear to be taller in the middle of the image.

4.1.3 Temporal resolution

Temporal resolution relates to the number of frames that a system can image per second. It is a measure of the ability of a detector and imaging system to accurately capture and display changing scenes such as in a conventional peripheral angiographic runoff study or a 3D acquisition.

The rate at which exposures are taken must be chosen such that the quality of the observed motion is sufficiently fine or apparently continuous between frames. If this chosen rate is too slow, rapid changes in signal levels generated by the movement

of structures between two successive frames would increase the number of artefacts introduced into these images.

The faster the acquisition rate, the poorer the signal-to-noise ratio (SNR), and the spatial resolution will also cause an increase in the introduction of motion artefacts. In attempts at improving the SNR and contrast resolution, a common method is sometimes used whereby several images taken sequentially over time are averaged. This produces results but at the expense of added artefacts as mentioned earlier (Harrington, 1982).

4.1.4 X-ray exposure and dose

Exposure data and dose rates are a combination of various factors. They are dependent on the kV range, pulse sequence, focal spot, beam filtering, image intensifier field size, SID and, not least, the anatomical area being scanned and the patient size. In other words, most of the system's parameters contribute to this measurement.

The exposure from a beam of ionising photons (x-rays) is defined as the quantity of x-rays that cause a certain charge to be produced in a block of air with a certain mass. Radiation energy is usually measured in keV with the conventional unit of exposure (though now obsolete) being the Roentgen (R). When discussing exposure, the terms entrance dose, absorbed dose and equivalent dose are referred to. These measurements are related to the amount of exposure that a mass of tissue experiences.

The *entrance dose* (Figure 4.7(a)) is the measure of the intensity of the x-ray beam. It describes the amount of energy that a unit mass of material is exposed to and is measured using an ion chamber.

The *absorbed dose* is the measure of energy deposited (absorbed) per unit mass of tissue. It is essentially the entrance dose less the dose received from the detector or exit dose as depicted in Figure 4.7(b) but is deemed unsuitable to contribute towards quantifying any form of health risk. As a result a measure called the equivalent dose is defined.

The *equivalent dose* is the product of the absorbed dose and a factor indicative of the affinity that the exposed tissue has to the radioactivity to which it is exposed. The unit used for the entrance dose and the absorbed dose is the Gray, Gy (where 1 Gy = 100

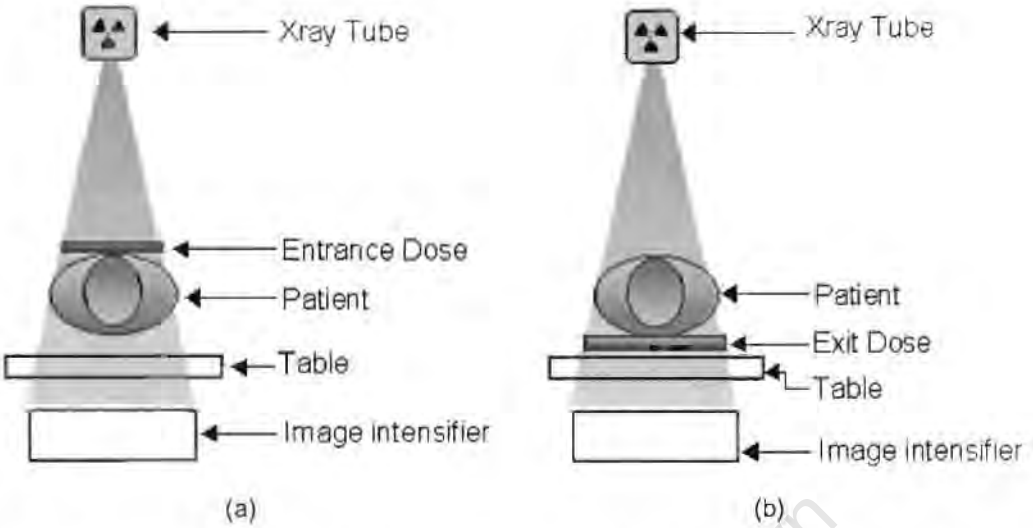

Figure 4.7: Two images showing the point at which (a)the entrance dose and (b) the exit dose is measured GE Medical Systems (2003).

rad), and the unit for equivalent dose is the Sievert, Sv (van Rooyen, 2001; Hering, 1990; Brown *et al.*, 1999). In the case of x-rays, these units (the gray and sievert) are numerically equal.

The radiation requirements for a DSA system's intensifier are of the order of 1 - 2 mR per image depending on the manufacturer (Schindehutte *et al.*, 1998). The varying values obtained for entrance dose rates in various journals range from 130 - 180 mR to 200 - 700 mR per image (Schindehutte *et al.*, 1998). For photons only (that is, x and gamma rays), the roentgen corresponds to an absorbed dose of about 0.87 rad in air, and 0.97 rad for soft tissue (Allard, 2003).

In the table below Brown *et al.* (1999) give a good indication of dosages and exposures experienced under various conditions. It shows the annual background radiation dose to be in the range of 1 mSv but it should be noted that this value is variable and depends on where an individual lives. The maximum annual dosage a member of the general population should experience is 1 mSv while those who work with radiation should not exceed a five year average of 20 mSv. Exposure rates of 0.5 Sv will cause nausea and sickness while doses of around 5 Sv will result in death in the months that follow this level of exposure.

In a DSA system the kilovolt values are adjusted via the operating console. This is important since it affects the dose. A high kV produces a "harder" x-ray beam that is

Table 4.1: Table showing typical figures for x-ray doses for five different conditions (Brown *et al.*, 1999).

Dose due to background radiation in one year(can vary greatly from place to place and arises from cosmic radiation, radio-active material in the surroundings and man-made radiation).	1 mSv	0.1 rem
Level set as the maximum dose to the general population in one year (a higher dose is sometimes allowed in one year provided the 5 year average does not exceed 1 mSv).	1 mSv	0.1 rem
Level set as the maximum dose to people who work with radiation (50 mSv is the maximum in one year).	20 mSv (5 year average)	2.0 rem
Dose exposure that will cause nausea, sickness and diarrhoea in some people.	0.5 Sv	50 rem
Dose exposure which will kill many people in the few months following exposure.	5 Sv	500 rem

richer in energy and more able to pass through the body. It is therefore similar to a strong filter in its dose reduction effects, except that image contrast decreases with high kVs (GE Medical Systems, 2003).

4.1.5 Noise

Noise is defined as any signal that does not carry any useful information. It is the main factor affecting image quality and limits the overall contrast resolution of the system. The effects of noise on an image are quantified in the signal-to-noise ratio (SNR), which is calculated using the number of x-ray photons detected by the image intensifier. The spectrum of the x-rays (radiation quality) emitted and the presence of scattered radiation adds noise to the image, thereby decreasing the SNR. In diagnostic radiology, scatter is therefore a major contributor to noise.

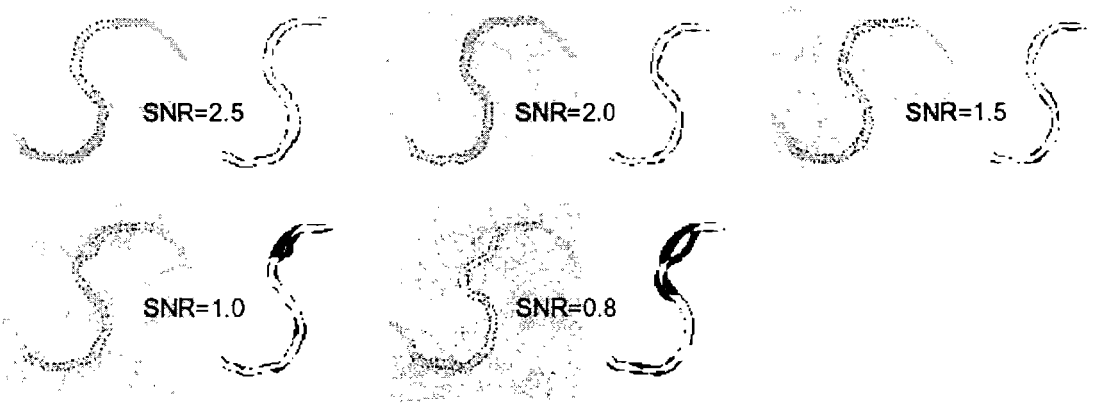

Figure 4.8: Examples of an image acquired with different SNRs. Artificial vessel with varying arrangements of noise (from top left to bottom right: SNR=0.8; 1.0; 1.5; 2.0; 2.5) (Hinz *et al.*, 2002).

In digital x-ray imaging, the image's signal is directly proportional to the amount of radiation transmitted through the object being scanned. The spectral distribution and the number of scattered photons reaching the image plane depend on three factors; the energy of the incident radiation; the area and shape of the radiation field; and the thickness of the material being radiated. In screen-film imaging, however, the film properties usually determine the magnitude of tissue differentiation.

Quantum noise, structural noise, electronic and digitisation noise are four of many sources of noise obtained throughout the imaging chain that are described here.

Quantum noise is the uncertainty that is introduced into the image because of the finite number of x-ray photons available to form each image; increasing the dose reduces quantum noise effects.

Structural noise is interference from portions of the patient's anatomy other than those being imaged.

Electronic and digitisation noise are associated with the TV camera's electronics and the digitising of the analogue output signal into a finite number of digital values for image manipulation and storage purposes respectively. The latter may be improved by increasing the bit depth of the digitised signal while in the former case, efforts have largely been directed toward improving the SNR of the TV camera so that the

system SNR is limited by quantum noise and not electronic and digital noise. *Frame integration* is a technique used to reduce the effects of electronic and quantum noise by averaging several successive frames together. Although this method has shown a significant improvement in SNR (digital systems require a SNR in the order of 1000:1) it has led to an increase in motion artefacts introduced into the image (Harrington, 1982).

Stickiness and lag are two aspects that decrease the accuracy of the digitised image. Stickiness is the tendency of high-brightness areas of the display to remain bright after the image is removed. Excessive image stickiness causes information to be carried over from one video frame to the next, especially during analogue-to-digital conversion at high frames rates.

Lag is related to the delay in the decay of the analogue output signal of the camera after the input image has been removed (Harrington, 1982; Kaut-Roth and Faulkner, 2002; ECRI, 2001).

Chapter 5

Motion Artefacts Encountered in Digital Imaging

5.1 Motion artefacts

Motion artefacts are what make digital subtraction angiography a challenging operation to perform. Although it would seem relatively simple to acquire at least two similar images for subtraction, because these images are of areas of a dynamic system, movement is inevitable. This movement may be due to patient body movement (voluntary motion) and/or the rotation and wavering of vessels caused by blood flow and relational organ movement (involuntary motion). This produces variations between the two images which, on subtraction, may produce artefacts that could obscure important details, thus complicating the diagnostic and planning processes. The primary concern is therefore associated with a two fold issue, that of voluntary and involuntary motion of the patient being imaged.

Voluntary motion is associated with gross patient movement and generally can be controlled with patient compliance. In most instances the patient is able to feel the contrast as it flows through the vessels. This is often uncomfortable and the patient may need to exercise considerable restraint to remain stationary during and between scans. In addition to this, the patient's condition may be such that he or she experiences some form of pain or other discomfort even though sedated. In the case of involuntary motion, however, vessel expansion and movement may result due to

the blood flow and relational organ movement, etc., and this cannot be controlled by the patient (Buzug *et al.*, 1998; Cox, 2000; Cox and de Jager, 1994; Maintz and Viergever, 1998; Meijering, 1999, 2001; Meijering *et al.*, 1999).

As a result a 2-D x-ray image cannot simply be shifted as a mere linear translation with respect to its successor in order to align the two although this is also done. Three-dimensional movement has to be considered before accurate registration can be attained. A good match is one in which artefacts obtained in the subtracted image are kept to a minimum, thus not obfuscating any detail in the image pair (Buzug *et al.*, 1998; Fitzpatrick, 1988).

In order to correct these artefacts in the subtraction images, a 2-D geometrical transform that completely accounts for the projective effects of 3-D movement is needed. As Meijering (2001) has commented, there are limitations in the extraction of such a transformation from the projection images. Buzug *et al.* (1998) doubted if a transform would ever be developed to the extent that it would entirely remove all artefacts due to this 3-D movement. Fitzpatrick (1988) stated that 3-D movement could not be described by a position-dependent shift in two dimensions. He therefore predicted that it was difficult to obtain ideal alignment of two images that exhibit this kind of difference between them (Fitzpatrick, 1988; Buzug *et al.*, 1998).

5.1.1 Examples of motion artefacts

Although a cooperative patient can often help to avoid gross movement artefacts, involuntary local motion of organs is inevitable. For example, most patients cannot resist the urge to cough or swallow, making the interpretation of DSA images of the carotid arteries extremely difficult. In imaging the lower peripheral vasculature, artefacts due to the lateral displacement of a leg may develop artefacts along the bone-tissue transitions that resemble vessels (Meijering *et al.*, 1999).

For example if the femur undergoes rotation as can be seen between the images in Figure 5.1 (the full image is shown in chapter 8 and it can be seen that this movement is due to rotation at the ankle joint) it appears, in the 2-dimensional image, that the femur has rotated anti-clockwise and in so doing has changed its angle. This in fact is not true due to the geometry of the femoral bone. To perform a linear rotation

(a) (b)

Figure 5.1: Trauma patient images (a) shows the mask image taken of the left lower limb of a trauma patient using Lodox technology. (b) shows a roadmap image taken prior to contrast injection to ascertain whether the catheter was positioned correctly.

in the plane of the image would then shift the surrounding structures unfavourably for matching conditions and the bone itself would never completely register, causing artefacts. An extreme example of this kind of mismatch can be seen in Figure 5.2 especially along the bone edges.

More examples of artefacts can be seen in Figures 5.3(a) and 5.3(b) where the arrows indicate a few of the more obvious artefacts acquired through the registration and subtraction process. It is clear that in both images, the majority of the larger artefacts were produced along the bone-tissue transitions as mentioned before, although in this situation they do not interfere with the clarity of the vessels being imaged.

Figure 5.2: Artefacts produced in a worst case malalignment

(a) (b)

Figure 5.3: Images obtained of (a) the ankle region of the lower limb (Hemmendorff *et al.*, 1999), (b) the shoulder region. The arrows indicate artefacts present in these images (Toshiba, 1995).

5.2 Patient related solutions

Several solutions have been proposed in order to minimise gross patient motion. These include considerations regarding contrast media used, breath-holding and patient immobilisation.

5.2.1 Choice of contrast media used

With regards to reducing patient motion initiated by the sudden sensation of heat caused by the contrast medium, the use of a non-ionic contrast medium has been suggested (Meijering *et al.*, 1999; Harrington, 1982). Studies have shown no difference in image quality, although it is not as cost effective as its iodine-based counterpart.

5.2.2 Holding breath

In some instances artefacts caused by respiratory motion have been avoided by applying generous amounts of oxygen before injection of the contrast. This has allowed patients to hold their breath for longer periods of time (Meijering, 2001).

5.2.3 Immobilisation

Strapping patients to the trolley, thus rendering them immovable, helps prevent motion artefacts in DSA images. For example, by strapping the leg in position, lateral rotation between images may be avoided.

5.3 Acquisition related solutions

A few solutions encountered in this regard are briefly described below. They relate to the use of multiple energy levels or a combination of energy and temporal images.

A third method makes use of a gating function in order to capture and align images accurately.

5.3.1 Dual energy image acquisition

Harrington (1982) and Meijering *et al.* (1999) mention the use of different energy levels to acquire the successive images. According to Meijering (2001), "the energy-dependent linear x-ray attenuation coefficient of iodine shows a discontinuity at 33 keV, whereas the attenuation coefficients of bone and soft tissue vary only gradually as a function of energy". This suggests two methods for DSA image acquisition. One is that x-ray images obtained at energy levels above and below this threshold will exhibit different contrast characteristics and a resulting subtraction should emphasise the iodine contrast in the image while reducing its background information (Meijering *et al.*, 1999; Harrington, 1982). The drawbacks to this technique are clearly stated in that it would only prove successful if the x-rays are nearly monoenergetic which puts high demands on the x-ray generator.

5.3.2 Hybrid subtraction

A second method involves the development of a "hybrid subtraction scheme" (energy and temporal images) whereby the dual energy subtraction can be used to remove soft tissue structures from both mask and contrast images, while temporal subtraction is used to eliminate residual bone structures (Lehmann *et al.*, 1981; Brody *et al.*, 1981a). The improvements are obtained, however, at the cost of increased patient exposure and a decrease in the signal to noise ratio (SNR) (Brody *et al.*, 1981b; Meijering *et al.*, 1999).

5.3.3 Synchronised gating

Another method that could be ernployed is "motion synchronised gating" of x-ray exposure. Cardiac pulsation can have an effect on the pulsatile motion of vascular structures resulting in artefacts. Meijering *et al.* (1999) suggest that these may be

avoided to some degree by acquiring images during the same cardiac phase such as end diastole.

5.4 Retrospective image processing solutions

Although the former sections suggest possible solutions to minimise the artefacts incurred during a scan, in most cases they will not be entirely eliminated. At this point retrospective correction in the form of image registration and grey-level distortion correction techniques may be used. The geometrical transform developed in this way would account for the changes caused by patient motion resulting in optimal alignment between the mask and contrast images prior to their subtraction (Meijering, 2001).

The simplest approach in this respect is probably a manually controlled translation of the mask image with respect to the contrast images, a technique often referred to as pixel shifting. Since in DSA systems, images are acquired, stored and processed digitally, this technique is fairly easy to implement. Pixel shifting, however, only provides a solution for situations where artefacts result from gross translational motion (Harrington, 1982). It thus reduces artefacts in some parts of the image while inevitably reinforcing or even creating new artefacts in the remainder of the image. This suggests that in most instances, patient motion is highly complex and cannot be modelled by so basic a transformation. It is therefore necessary that the registration techniques utilised or developed address more "local control" in order to be able to correct for more complex patient motion as discussed earlier.

Chapter 6

Registration and Subtraction

The objective behind the process of registration in DSA is to align two images, scanned at different time intervals, of the same region of interest. The structures being scanned in DSA are usually vessels of the human body – a dynamic system. Differences between the two acquisitions are therefore expected, resulting in spatial misalignment or geometric distortion. These changes contribute to scene ambiguity, and may arise due to an inconsistency in the irradiation of a scene or the imaging system used, or changes in the scene itself due to patient motion as discussed in Chapter 5 (Cox, 2000).

Cox (2000) emphasises the importance of differentiating between *matching* (the two scenes look the same) and *registration* (they are the view of the same scene) since there are multiple positions of match between image v (contrast image) and subimage T_u (of the mask image u) but only one position of correct register.

The solution is therefore non-trivial and there has been extensive research (Buzug *et al.*, 1998; Chiang and Sullivan, 1993; Cox, 2000; Dougherty *et al.*, 1999; Douglas *et al.*, 2002; Goshtasby *et al.*, 1986; Maintz and Viergever, 1998; Meijering, 2000; Venot *et al.*, 1998) into this field in an endeavour to find a solution that is both effective and computationally inexpensive.

In this chapter only two dimensional, monomodal, intra-subject registration concepts are considered as these apply to DSA. By the term monomodal reference is made to the registration of images acquired through the same modality i.e. that of x-rays

using a single acquisition machine throughout the procedure. Intra-subject registration indicates that all images involved in the registration task are acquired of a single patient (Maintz and Viergever, 1998).

6.1 Transformations

The process of registration (also referred to as image fusion, superposition, matching or merging) is based on the definition of the transformation that maps the points of one image onto corresponding points in a second image (Maintz and Viergever, 1998; Goshtasby *et al.*, 1986). Linear transformations can be used when it is assumed that the factors affecting optimal alignment of the images, with respect to the acquisition system (limited spatial resolution, noise, beam hardening, time-varying scatter, non-mono-energetic x-rays and actual grey values), are negligible (Maintz and Viergever, 1998; Ashburner and Friston; Meijering *et al.*, 1999). Linear transforms include rotation, scaling, reflection and translation and may also make use of uniform and non-uniform scaling and shearing. When there is a geometric variation in the structures of the image, curved transforms or warping may be applied (Maintz and Viergever, 1998).

The nature of the transforms mentioned above are such that *rigid co-ordinate transformations* only translate and rotate images. *Affine transformations* map parallel lines onto parallel lines while *projective transformations* map lines onto lines. *Curved* or *elastic transformations* map lines onto curves. Each transform is a special case of the one preceding it and can be used in different combinations. Curved transformations, however, are not usually represented using constant matrices. They are usually represented in terms of a local vector displacement field or a polynomial transformation in terms of the 'old' coordinates (Maintz and Viergever, 1998).

6.1.1 Global and local transforms

A transformation is considered global if the transformation applies to the entire image. These transformations are used most frequently in registration applications and are popular in many common medical images where the rigid body constraint is fairly

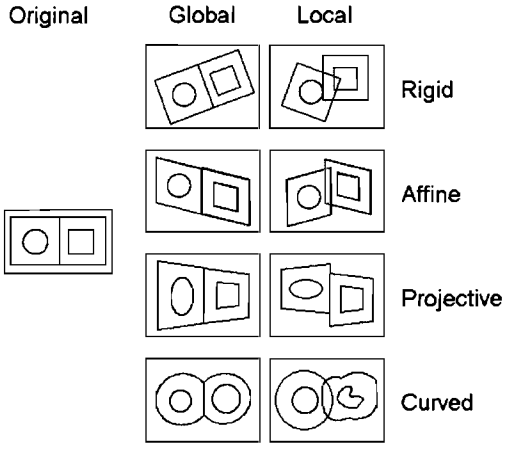

Figure 6.1: Examples of 2-D transforms adapted from Maintz and Viergever (1998).

well satisfied (Maintz and Viergever, 1998). If sub-sections of an image have their own transformation and cannot be described as having a global transformation, this particular transformation is referred to as a local transformation. According to Maintz and Viergever (1998), most rigid and affine approximations are global while curved transformations are local. The characteristics of the various transforms described above are illustrated in Figure 6.1.

6.1.2 Extrinsic and intrinsic methods

Two methods for image registration may be used, namely extrinsic and intrinsic based methods. In extrinsic based methods foreign objects, such as fiducial markers, are introduced into the image space while intrinsic based methods rely on patient generated image content, i.e. registration is based on a set of identified points or landmarks found in the image such as bony edges (Maintz and Viergever, 1998).

6.1.3 Optic flow and template matching techniques

Techniques to automatically compute the displacement of certain structures within two images may be found using gradient-based optic flow or template matching techniques (Maintz and Viergever, 1998; Cox, 2000; Meijering, 2000; Dougherty *et al.*, 1999).

Optic flow techniques

Meijering (2001) discusses the principles behind the optic flow technique and then concludes, as does Cox (2000), that it is unsuitable for digital subtraction of x-ray images such as in angiography. This is due to the necessary *a priori* assumptions made in this technique – namely that the structures in the image change only in position and not in intensity, and that the technique is sensitive to contrast. In the case of DSA, neither of these assumptions hold due to patient motion and contrast injection. It is not the purpose of this thesis to develop or test these points so it was decided to use what has been developed through template matching techniques found thus far (Cox, 2000; Meijering, 2000; Fitzpatrick, 1988; Dougherty *et al.*, 1999).

Template matching techniques

Template matching is based on the assumption that the local displacement of a structure in one image, u (mask image), can be estimated by defining a window of size K x L pixels in u, containing that structure, and then finding its corresponding position in v (contrast image). Figure 6.2 demonstrates this concept. The grey box represents the window of size K x L pixels extracted from the mask image. A region or search area, designated by A in the figure, is determined in which a corresponding match-position of the template is expected to be found. The template is then moved pixel by pixel in the direction indicated by the large black arrows and a similarity measure is used to determine whether a match has occurred. Position P indicates the position of best match of the template in the search area and thus in the contract image. This process can be made more robust in the presence of contrast by choosing the most appropriate window size and a similarity measure that is relatively insensitive to grey value disparities (an important consideration when performing DSA where contrast medium is used for vessel enhancement). It is also generally computationally expensive and suffers, as do optic flow methods, from problems associated with independently moving structures and aperture issues. To compensate, most motion correction techniques compute only optimal correspondence for a select set of windows rather than for each individual pixel. This does, however, limit the degree of complexity to which the transform may be developed and therefore patient motion corrected for and gives

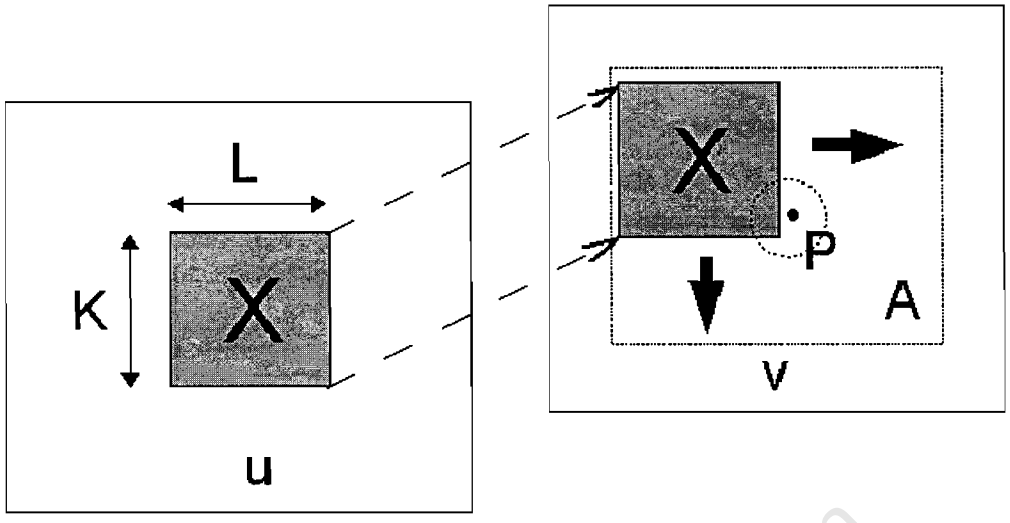

Figure 6.2: Illustration of the template matching concept. Here u is the mask image, and v is the contrast image. The grey box represents the template of size K x L with the large X as the control point in question. A is the search area and P is the point of best match.

unreliable results in homogeneous regions (Maintz and Viergever, 1998; Cox, 2000; Meijering, 2000).

The simplest approach is to utilise the entire mask image u as a template (global transformation) but this limits patient motion correction to gross translation and/or rotation using automated pixel shifting (Maintz and Viergever, 1998; Cox, 2000; Meijering, 2000; Tangkuampien, 2001). Local translation and rotation correction necessitates a more confined search region within the image.

Higher level methods make use of displacement vectors of control points constituting a sample set of the original vector field. These vectors are obtained by applying the template matching technique to small windows around each control point (in Figure 6.2, the X would represent a selected control point). The window size is determined by the minimum information required for obtaining reliable estimates for each corresponding control point's displacement. With the use of interpolation, a global geometrical transformation may thus be constructed (Maintz and Viergever, 1998; Meijering, 2000; Meijering *et al.*, 1999).

6.2 Control point selection

Control points provide a sample set of the entire image whereby computational time can be reduced and accuracy increased by allowing more localised searches. Two methods, regular grid point selection and feature-based point selection, were explored as regards control point selection.

Regular grid point selection

This approach is the simplest and most often performed. Regular grid point selection makes use of a regular grid defining a quadrilateral mesh. The control points are then selected at the points of grid-line intersections (illustrated in Figure 6.3) and are therefore chosen independently of the image content (Meijering, 2000; Tangkuampien, 2001). The finer the grid used, the more accurate the output achievable but the more computationally expensive the operation.

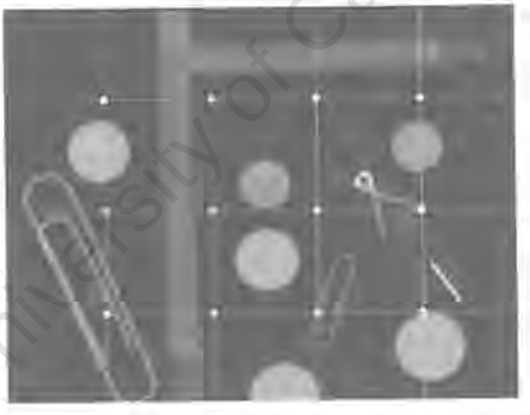

Figure 6.3: An example of control point selection using the regular grid method. Notice that the control points are located at grid line intersections.

Feature-based point selection

In the feature-based point selection method, sample points are selected based on certain similarity criteria. These criteria, unlike in the regular grid selection process, are dependent on image feature content. To ensure minimal false matches, the points chosen need to be unique, relative to their neighbours. This therefore produces a

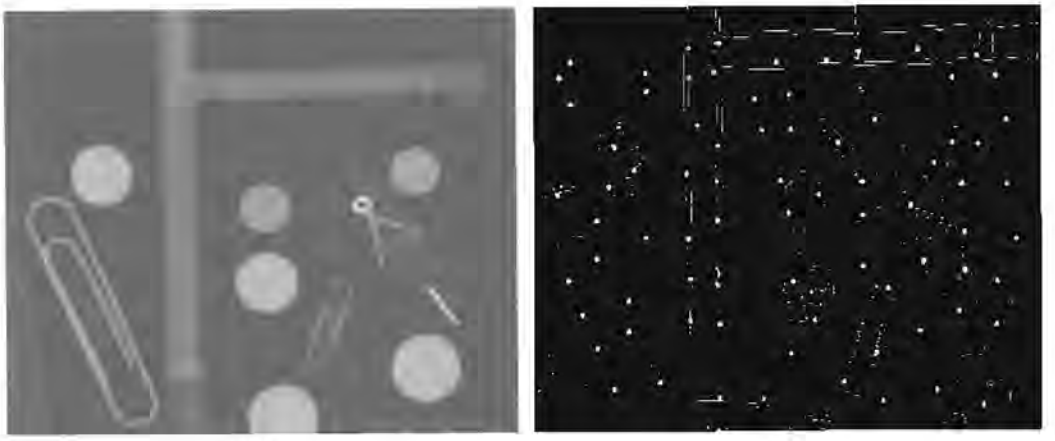

(a) (b)

Figure 6.4: (a) The image from which control points will be selected; (b) control points selected along the image edges.

set of irregularly distributed points. Figure 6.4(b) provides an example of a data set obtained from the image in Figure 6.4(a) by utilising image edges as the similarity criteria (Buzug *et al.*, 1998; Meijering, 2000; Cox, 2000; Tangkuampien, 2001).

6.3 Interpolation methods

A complete displacement vector field of the entire image domain is necessary in order to provide information for warping the mask image with respect to the contrast image. The entire displacement vector field can be established if two criteria hold: (1) it can be described by the displacement vectors of the selected control points; and (2) it can be assumed that the remaining pixel displacement vectors in the image can be obtained through linear interpolation (Meijering, 2000).

In the interpolation process, data are calculated at 'selected' locations while data for intermediate positions are approximated. Interpolation is therefore a form of sampling. The value of an interpolated pixel is a weighted average determined by the distance each pixel is from the point in question and its neighbouring pixels. Interpolation methods include: rectangular-based interpolation *e.g.* bilinear interpolation and triangular-based interpolation *e.g.* piecewise linear interpolation (Matlab Help File; Tangkuampien, 2001).

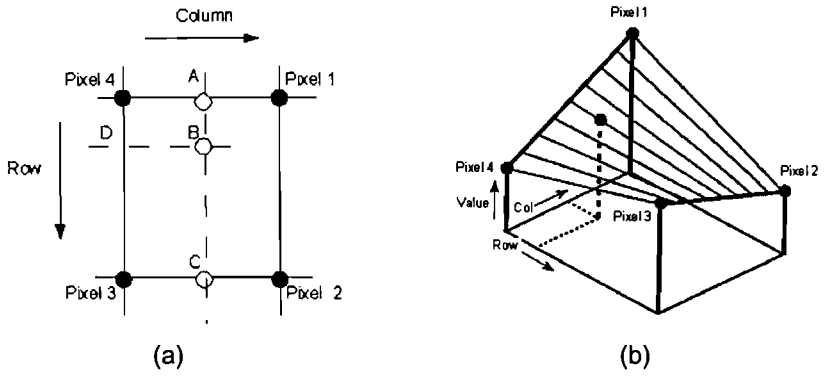

Figure 6.5: Subpixel interpolation using bilinear interpolation. In (a), the two intermediate values are found by linear interpolation in the horizontal direction. The final value is found by interpolating the intermediate values in the vertical direction. This is depicted in three-dimensions in (b) (Smith, 1999).
A = position: (pixel 4+pixel 1)/2, value: (pixel 4+pixel 1)/2; B = position: (pixel 4+pixel 1)/2, value: (pixel 4+pixel 1)/2; C = position: (pixel 3+pixel 2)/2, value: (pixel 3+pixel 2)/2; D = position in pixel in the original image

Rectangular-based interpolation

Rectangular-based interpolation methods are predominantly used when the set of sampled points are regularly spaced and the position and value of the intermediate points are known. In the bilinear method, interpolation takes place in a rectangular grid (as outlined in Section 6.2). The output pixel value is a weighted average of pixels in the nearest 2-by-2 neighbourhood. In other words the four neighbouring pixels are interpolated in two steps: first in the horizontal direction, producing two intermediate values; and then in the vertical direction, producing a single bilinear interpolated pixel value which is transferred to the warped image (Meijering, 2000; Cox, 2000; Tangkuampien, 2001; Smith, 1999). This is illustrated in Figure 6.5 where in (a) is a 2-D illustration and (b) a 3-D illustration of bilinear interpolation. Here, the first two intermediate values are found by linear interpolation in the horizontal direction. The final value is then found by interpolating the intermediate values in the vertical direction. This procedure can be used to uniquely define all the values between the four known corner pixels

Triangular-based interpolation

Triangular-based methods are usually utilised when dealing with irregularly spaced sample points. In this case neighbourhood relationships need to be established in

order to ascertain which points will exert influence over the interpolation of the intermediate points with unknown data values (Tangkuampien, 2001). Figure 6.6 shows an example where seven sample points (a) and the corresponding triangular mesh (b). Figure 6.6(c) illustrates the interpolated signal of these points with arbitrary chosen grey levels (Baum and Speidel, 2000).

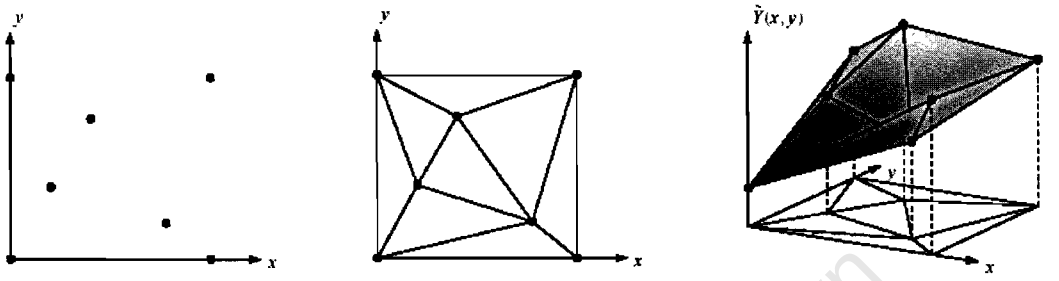

(a) (b) (c)

Figure 6.6: Triangulation of a set of sample points (Baum and Speidel, 2000)

Piecewise linear interpolation – a local transformation – is an example of triangular-based interpolation. In this type of transformation, different mathematical expressions are applied to different regions within an image. The Delaunay triangulation is an example of a piecewise linear interpolation technique and consists of a set of lines connecting each sampled point to its natural neighbours.

The Delaunay tessellation

The defining points (sampled points) or nuclei of a 2-dimensional Delaunay tessellation lie at the vertices of triangles. Two triangles may share an edge and more will share a vertex. The three vertices of each triangle lie on the circumference of a circle and no other vertex of the array lies within that circle. This is because the centre of the sphere is in the position of a vertex in the dual Voronoi tessellation, and this vertex is by definition equidistant from the three nuclei (Watson, 1981). Figure 6.7 demonstrates a set of such circumcircles (cirumcircle: a circle touching all the vertices of a triangle) that is used to form a Delaunay triangular mesh. Here (a) fulfills the Delaunay criterion while (b) does not due to the circle defined by S_1,S_3 and S_4 containing S_5 (Baum and Speidel, 2000).

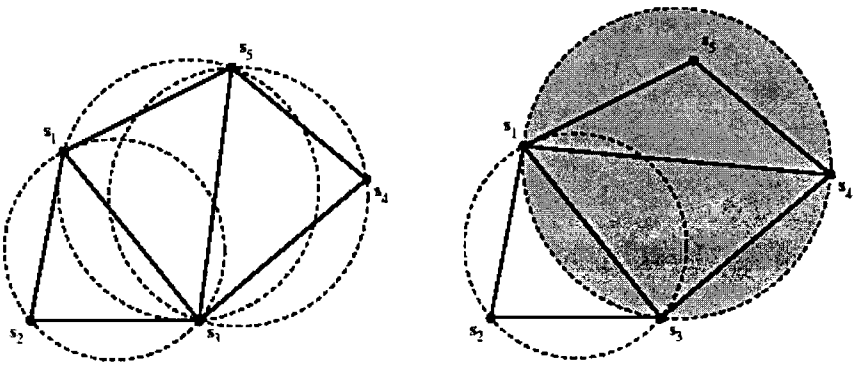

(a) (b)

Figure 6.7: Two triangulations and their circumcircles. (a) fulfills the Delaunay criterion but not (b) due to the included vertex S_5 (Baum and Speidel, 2000).

Zuiderveld *et al.* (1992) proposes the use of *posteriori* adjustments to unreliable displacement vectors using iterative relaxation while Buzug *et al.* (1998) and Cox (2000) use an *a priori* exclusion principle to exclude those regions in the control point selection process. This however results in an irregular grid. Buzug *et al.* (1998) compensated for this by using the vector fields to define affine transformations and thin-plate splines. Meijering (2001) argued that since the majority of the artefacts found in the subtracted image were along strong object edges in the two unsubtracted images, the control points selected should be based on these edges. He made use of the Canny operator for the edge detection algorithm and then extracted the control points from the resultant image. He then proceeded to construct a displacement vector field by linearly interpolating the local displacement vectors using the Delaunay tessellation algorithm (Buzug *et al.*, 1998; Meijering, 2000, 2001).

6.3.1 Canny edge detection

Edge detection is a fundamental imaging process. Consequently there are numerous edge detectors in use. These include: the Sobel, Prewitt, Roberts and Canny detectors to mention a few. This section provides a brief overview of the Canny edge detector which was used in the development of this dissertation.

The Canny method finds edges for local maxima of the image's gradient. The gradient is calculated using the derivative of a Gaussian filter. The method uses two thresholds, to detect strong and weak edges, and includes the weak edges in the

output if they are connected to strong edges. This method is less sensitive to noise, and more likely to detect true weak edges.

The method consists of three stages:

1. Directional gradients are computed by smoothing the image and numerically differentiating the image.
2. Peaks in the image gradient are determined.
3. Hysteresis thresholding locates edge strings.

Stage 1:
The image is smoothed by convolution with an appropriate Gaussian filter. The width of the filter determines the detector's sensitivity to noise – increased filter width results in decreased sensitivity to noise. Simpler detectors, such as the Roberts cross difference operator, are then used to determine the direction and magnitude of the gradient.

Stage 2:
The gradient magnitude at the particular pixel is then compared with that of its neighbours along the direction of the gradient. The pixel is considered an edge pixel if its magnitude exceeds either of its two closest neighbours; otherwise it is considered a background pixel.

Stage 3:
Weak edges are removed by hysteresis tracking. This process is dependent on the threshold values. For good results, the upper threshold T_U, and lower threshold T_L need to be set quite high and low respectively. However if these levels are too extreme in their respective directions, noisy edges and edge fragmentation may occur.

In summary, it is noted that the canny detector is dependent on 3 variables: the filter width and its two thresholds T_U and T_L. It is these two thresholds that make it more flexible than other detectors. By varying the lower threshold T_L weak edges, not always picked up by other detectors, are identified (Meijering, 2000; Tangkuampien, 2001; Matlab Help Files).

6.4 Similarity measures

The transformation of choice is based on the optical match of the mask template with its corresponding position in the contrast image. A similarity measure is used to determine this match. These measures have been extensively explored in the literature (Buzug *et al.*, 1998; Chiang and Sullivan, 1993; Cox, 2000; Dougherty *et al.*, 1999; Douglas *et al.*, 2002; Goshtasby *et al.*, 1986; Maintz and Viergever, 1998; Meijering, 2000; Venot *et al.*, 1998). For the purposes of this dissertation, only four main areas will be briefly described. They are all compatible with both monomodal imaging and template matching techniques and are: the 'classic' correlation based methods; the difference based measures; sign-change based measures and histogram based measures. The histogram of differences will be discussed in more detail because it was the similarity measure decided upon in this dissertation.

6.4.1 Correlation based measures

Correlation provides a means of detecting a known image signal in a noisy background. The resultant signal contains peaks that indicate regions of similarity between the two images being correlated. Mathematically, the measure M of correlation C, can be defined as follows:

$$M_c(j,k) = \sum_r \sum_s v(j,k)T(j+r,k+s) \tag{6.1}$$

where j and k are the row and column co-ordinates within the image respectively. T is a template of the mask image u; v is the contrast image over which the template is being moved, and r and s are pixel shifts in the horizontal and vertical directions respectively.

Cross correlation

The cross correlation function differs from the autocorrelation function in that it finds the correlation between two different images unlike the latter where one image is correlated with itself. The cross correlation function C between two images u and v,

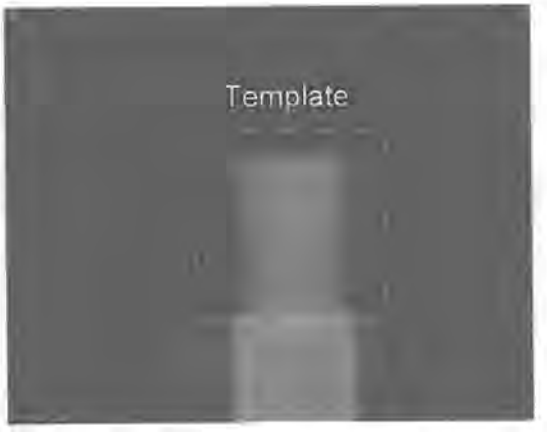

Figure 6.8: Template extracted from the mask image for the correlation process with the contrast image.

each of size K x L, can therefore be defined in terms of their inner product as follows:

$$C(u,v) = \sum_i u_i v_i. \tag{6.2}$$

where (u_i,v_i) are corresponding pixel pairs. A pictorial representation of this measure is found in Figures 6.8 and 6.4. Figure 6.8 shows the selection of the template image that will be correlated with the contrast image in Figure 6.9(a). The arrows indicated the two directions in which the mask is shifted to find its point of best fit. Figure 6.9(b) shows the result. The point of best match is indicated by the red cross. A profile through the image along a specific row passing through this point is given in Figure 6.9(c) with the peak at the point of best fit.

By normalising this function, the measure becomes invariant to the scaling of pixel intensity values and yields:

$$C_N(u,v) = \frac{\sum_i u_i v_i}{\sqrt{\sum_i u_i^2 \sum_i v_i^2}}, \tag{6.3}$$

To make it invariant to scale and offset values, the normalised cross correlation of zero-mean images is found:

$$C_{NZM}(u,v) = \frac{\sum_i (u_i - \bar{u})(v_i - \bar{v})}{\sqrt{\sum_i (u_i - \bar{u})^2 \sum_i (v_i - \bar{v})^2}}, \tag{6.4}$$

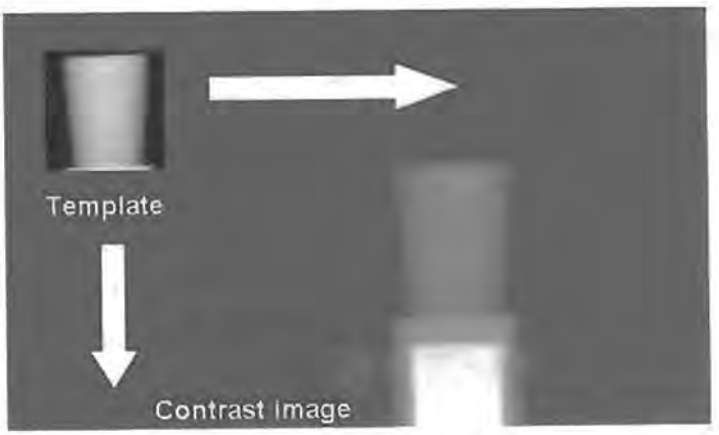

(a)

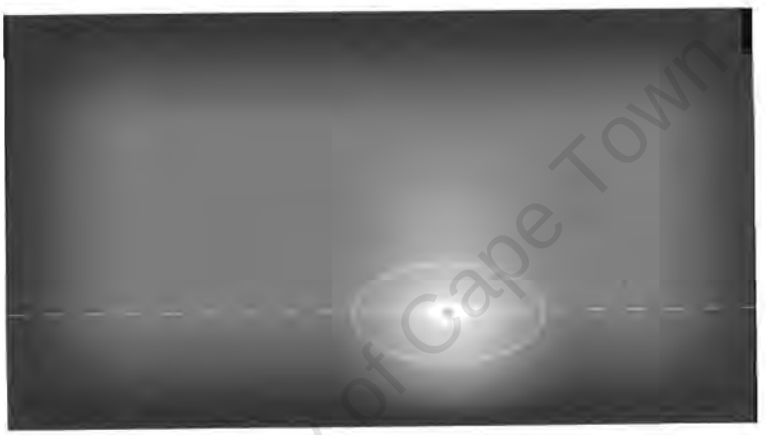

(b)

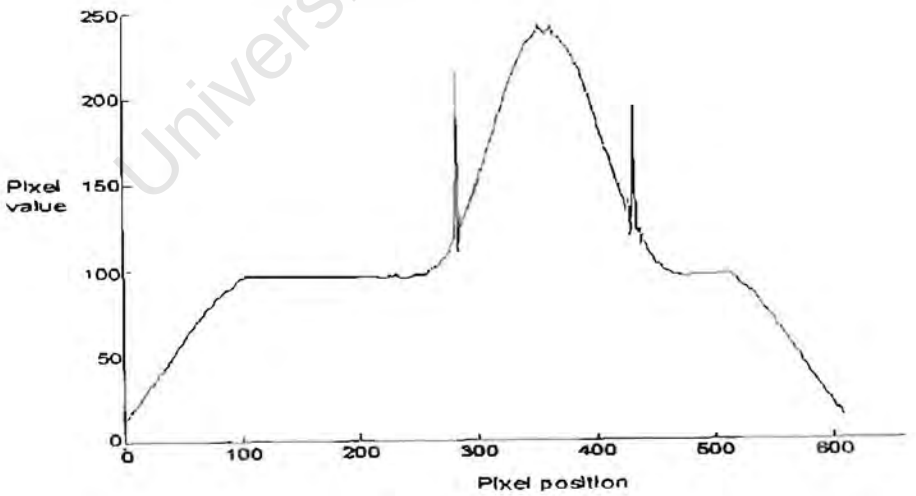

(c)

Figure 6.9: (a) The correlation process. The white arrows indicate the direction of the template's movement for correlation. (b) The resulting image of a correlation process. The red cross indicates the point of best match. The position of the profile plotted in (c) is indicated by the dashed line in (b) with the peak corresponding to the red cross, also in (b).

where

$$\bar{u} = \frac{1}{KL}\sum_i u_i \qquad \text{and} \qquad \bar{v} = \frac{1}{KL}\sum_i v_i \tag{6.5}$$

With KL being the number of pixels in the image window. A range of $[-1, 1]$ and c $= 0$ represents a total lack of correlation between the two images, c $= -1$ represents a correlation in images of reversed polarity and c $= 1$ a correlation of identical images with the expectation of scaling and offset (Cox, 2000; Stremler, 1990).

Phase correlation

Phase correlation utilises the Fourier shift property of the normalised cross correlation function (equation 6.3) to determine the relative shift between the two images. The Fast Fourier transformation (FFT) is more efficient than that of cross-correlation (which is similar in its mathematical representation to convolution) since it makes use of multiplication in the spatial-frequency domain rather than convolving in the spatial domain. The phase correlation C_p, of images T(j, k) and v(j, k) is given by the inverse Fourier transformation of the phase difference between them:

$$C_p(j,k) = \mathcal{F}^{-1}\left[\frac{V(\omega,\upsilon)\tau(\omega,\upsilon)^*}{|V(\omega,\upsilon)\tau(\omega,\upsilon)^*|}\right], \tag{6.6}$$

where image v(j, k) is an m_v x n_v image and T(j, k) is a known m_T x n_T template and $m_T < m_v$ and $n_T < n_v$.

A peak in C_p represents the presence of T in v, $\mathcal{F}$ is the Discrete Fourier Transform (DFT), V and τ are the DFTs of v and T respectively, and τ_* denotes the complex conjugate of τ.

If the two images T and v are identical but shifted with respect to each other by r and s in the horizontal and vertical directions respectively, then:

$$v(j,k) = T(j-r, k-s),$$

After applying the shift theorem, the Fourier transform gives

$$V(\omega_j, \omega_k) = \tau(\omega_j, \omega_k)e^{-j(\omega_j r + \omega_k s)},$$

Since V and τ are identical, this shows that the difference between the images is only due to a phase change. The phase correlation is then found using the inverse Fourier transform as described earlier and yields:

$$\begin{aligned} C_p(j,k) &= \mathcal{F}^{-1}\left[\frac{V(\omega,\upsilon)\tau(\omega,\upsilon)^*}{|V(\omega,\upsilon)\tau(\omega,\upsilon)^*|}\right], \\ &= \mathcal{F}^{-1}(e^{-j(\omega_j r+\omega_k s)}) \\ &= \delta(j-r,k-s) \end{aligned}$$

The DFT is thus a shifted dirac delta, δ(j, k), with its peak at the position of best match.

In practice, phase correlation gives a narrow peak which performs adequately in the presence of narrowband noise (Cox, 2000). Therefore the phase correlation measure exhibits the benefits of the normal cross correlation function in its invariance to pixel-value scaling and offset while also showing toleration to spurious low-frequency background intensity variations which are often regarded as narrowband noise (Cox, 2000).

Cox (2000) makes a generalisation that in sub-optimal statistics image pairs with low match correlation produce better results when correlation-based measures are used, while difference-based measures perform better when the match correlation coefficient is close to unity. Correlation is therefore suitable as a similarity measure in the instances of overall varying grey-value scaling and offsets but not if an edge is introduced into one of the images, as in the case of a contrast injection into the vessels. In DSA image acquisition, the results of this function are therefore unreliable.

6.4.2 Difference based measures

This is the most common similarity measure used and is based on the difference in intensity values between corresponding pixels. The simplest measure is that of the absolute sum of differences (ASD):

$$D_{ASD}(\mathbf{T},\mathbf{v}) = \sum_i |T_i - v_i|, \tag{6.7}$$

The sum of squared differences (SSD) is similar:

$$D_{SSD}(\mathbf{T}, \mathbf{v}) = \sum_i |T_i - v_i|^2, \tag{6.8}$$

Both of these measures are at a minimum under matching conditions. The main difference lies in the squared mean of the SSD which will weight large differences quite highly, making it more sensitive to noise when compared to the absolute sum of differences measure. The intolerance of both of these measures to outlying pixel values render them prone to false positive or false negative matches.

Cox and de Jager (1994) propose a measure called the variance of differences (VOD) defined as:

$$D_{VOD}(\mathbf{T}, \mathbf{v}) = \frac{1}{KL} \sum_i \left[(T_i - v_i) - \frac{1}{KL} \sum_i (T_i - v_i) \right]^2. \tag{6.9}$$

It is essentially the SSD measure with its sampled mean subtracted prior to summation and shows insensitivity to pixel offset differences between images T and v (Cox and de Jager, 1994).

6.4.3 Sign change measures

Stochastic sign change (SSC) and deterministic sign change (DSC) measures

This measure has been used mainly in the area of medical image registration (Cox, 2000) and was proposed for situations where matching is compromised due to obscuration of image details.

According to Chiang and Sullivan (1993) the sign change measures utilise sign changes in displacement vectors obtained from the pixel difference values between two image frames. This can be done directly or via the introduction of a sign change pattern. The latter method involves adding a fixed value periodically to the pixel difference values and subsequently computing the number of sign changes this produces in the displacement vectors. The displacement vector corresponding to the maximum number of sign changes is chosen as the displacement estimate.

If two images $F_1(j,k)$ and $F_2(j,k)$ differ only by additive noise that has a zero mean and symmetrical probability density function (pdf), then $S(j,k) = F_1(j,k) - F_2(j,k)$ will be subtracted image which exhibits random fluctuations according to the noise properties around zero. In the presence of minimal to zero noise, i.e. where the noise is too low compared to the precision of digitisation, the SSC gives a null response (this would not be suitable for the registration of x-ray images). As a result Venot and Leclerc (1984) and Venot *et al.* (1998) developed the discrete sign change (DSC) measure whereby they added a pattern to the difference and used this result to detect the sign changes. Chiang and Sullivan (1993) described this measure as a comparison between the number of corresponding bits in two different frames for a fixed amount of displacement. The displacement estimate is obtained when the number of matching bits reaches a maximum.

$F_3(j,k) = F_2(j,k) + q$ if $j + k$ is even,
$F_3(j,k) = F_2(j,k) - q$ if $j + k$ is odd.

$S'(j,k)$ is then defined as $F_1(j,k) - F_3(j,k)$ and the DSC criterion is calculated as the number of sign changes in $S'(j,k)$ scanned line by line or column by column. When $F_1(j,k)$ and $F_2(j,k)$ are similar, the DSC value is $N - 1$ for an N pixel zone (Venot *et al.*, 1998).

According to Meijering (2001), the DSC measure is confirmed as the superior measure when compared to that of cross correlation (CC), ASD and DSC as it proves insensitive to the inflow of contrast. Its disadvantage lies in its reliance on a parameter, q, that needs to be tuned.

Coincident bit counting

Chiang and Sullivan (1993) designed a measure that is independent of grey values. It is the measure of similarity based on the number of coincident bits in the binary representation of corresponding pixels in two images. It can be defined as follows:

$$S_{CBC}(\mathbf{T}, \mathbf{v}) = \sum_i bits(T_i \bar{\odot} v_i), \tag{6.10}$$

where $\bar{\odot}$ represents the exclusive nor operator. The authors state that one can decrease its sensitivity to noise and steepen the peak at position of match (in the event of template matching) by the exclusion of the lower or higher order bits respectively.

Meijering (2001) questioned the competence of this measure because he noted that it suffers from inconsistent weighting of intensity differences and is not as insensitive to noise as has been claimed.

6.4.4 Mutual information

According to Cox (2000), mutual information was used as a similarity measure by Viola and Wells III (1995). It is mentioned here for the purpose of completion but only as a comment. Cox (2000) discusses this measure in a fair amount of detail. Suffice to say that it is a measure of fit between "a model and an image in order to find the pose of an object". Maes *et al.* (1997) used it to register multimodal medical images and Cox (2000) notes that it is better suited to problems like these where large images from different modalities have to be registered. Consequently, it is inadequate for the purposes of DSA where monomodal image alignment and subtraction using template matching (smaller subimages) for sub-pixel accuracy is necessary for motion correction.

6.4.5 Histogram of differences-based measures

This measure takes into account the frequency of grey-level difference values rather than the individual pixel value differences. Therefore, in the case of optimal alignment only a small number of grey level differences will exhibit high relative frequencies, while the majority of differences will have a low relative frequency, resulting in a sharply peaked histogram. In the case of a mismatch a histogram with a larger dispersion will be depicted.

The normalised histogram of differences, $\mathcal{H}(g)$, is defined as:

$$\mathcal{H}(g) = \frac{1}{KL} \sum_{i} \delta(I_{di}, g) \tag{6.11}$$

where I_d is the difference image and g[−G, G] is any grey-value difference, and δ(j, k) is the Kronecker delta function:

$$\delta(j,k) \triangleq \begin{cases} 1 & \text{if } j = k, \\ 0 & \text{if } j \neq k. \end{cases}$$

Buzug *et al.* (1998) later proved that any measure was suitable as a similarity measure for registration provided is was a strictly convex, differentiable function. These are faster to compute and retain their similarity properties as far as similarity measures are concerned. They proposed several weighting functions namely:

$f_1(P_x) = P_x \log p_x$ – Lehmann *et al.* (1981); Buzug *et al.* (1998) used the Entropy Histogram of Differences (ENT),

$f_2(P_x) = P_x^2$ – the Energy of the Histogram of Differences (EHD) and

$f_3(P_x) = -\text{sqrt}P_x$

where P_x is the fraction of pixels with grey value g_x; $x = 1$ is associated with g_{min} and $x = N$ with g_{max}, the minimum and maximum pixel values of the difference image I_d, respectively.

They also argued that the function $f_2(P_x) = P_x^2$, leading to the EHD was both computationally cheap and yields accurate results. Their similarity measure of choice is therefore:

$$M_{energy}(r,s) = \sum_{x=1}^{N} p_x^2. \tag{6.12}$$

and is maximised.

These measures are computationally inexpensive while yielding accurate results. In the case of optimal alignment, only a small number of grey level differences have a high relative frequency, while the majority of differences have a low relative frequency which results in a sharply peaked histogram whether the window contains opacified vessels or not. The former case results in two peaks and the latter in one peak. In the case of misalignment the histogram will have a larger dispersion in both cases. This is illustrated in Figure 6.10.

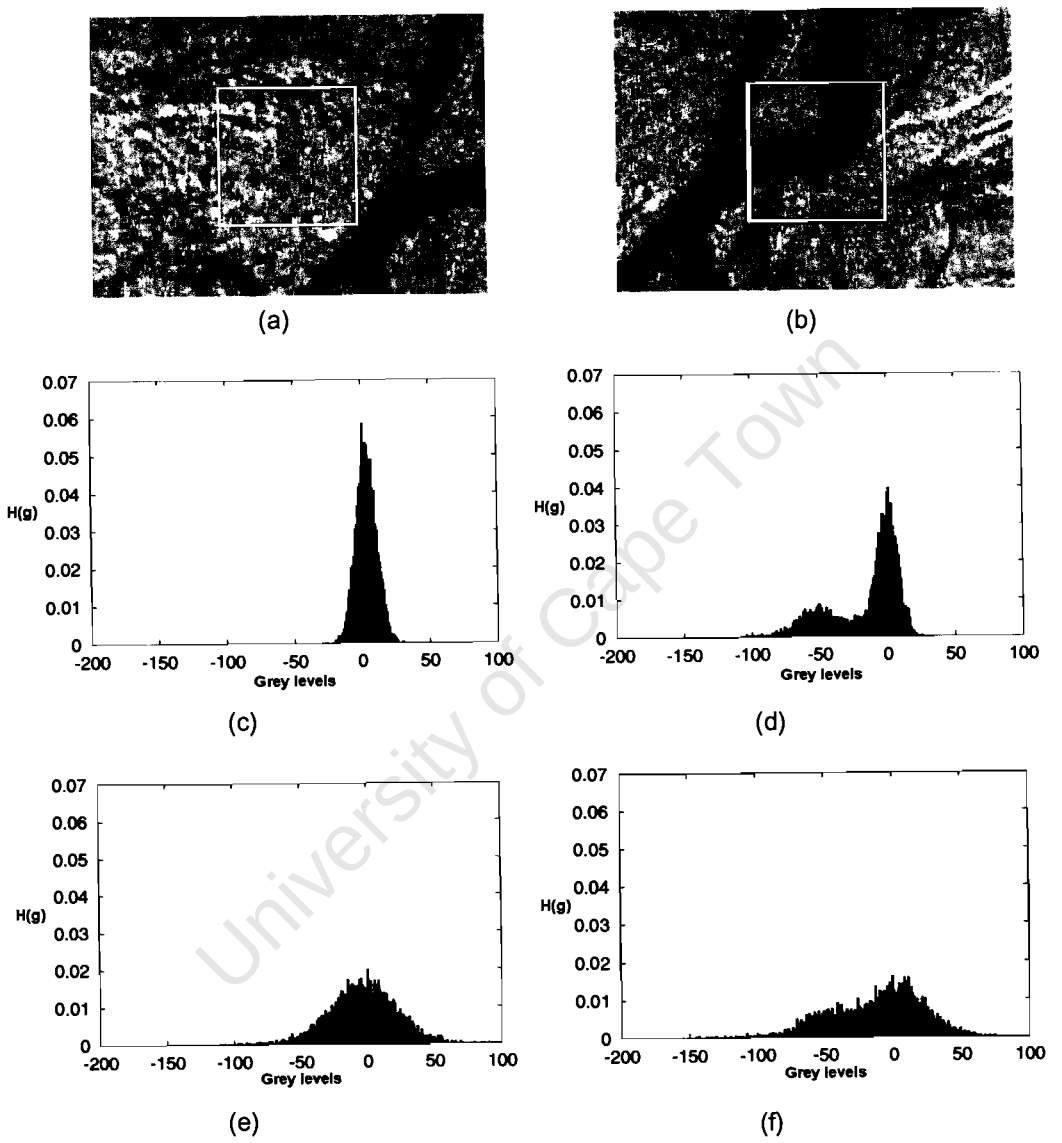

Figure 6.10: (a) and (b) are sections of a subtracted image. The white boxes show regions of interest: (a) without and (b) with contrasted vessels. Below are figures showing the normalised histograms. (c) and (d) indicate alignment and (e) and (f) indicate a case of misalignment of the original mask and original contrast images (Meijering, 2001).

6.4.6 Displacement interpolation

A suitable tessellation is necessary in order to perform the appropriate interpolation. In the case of irregularly distributed control points, triangles, whose vertices are the selected control points, are used to form a triangular mesh. The solution to this problem, however, is not always unique. Meijering (2001) found that the Delaunay triangulation was suitable for this purpose. It ensured that the smallest angles within the triangles utilised were both unique and as large as possible. This did not hold in cases where four or more points were co-circular and the Delaunay triangulation was not locally unique. In such cases an incremental algorithm described by Watson (1981) was suggested.

6.4.7 Inconsistency detection and correction

In the case where inconsistent vectors were present, the value of the Gaussian-weighted average of the vectors of the consistent natural-neighbours was substituted.

Consistency is determined using the criteria set out by Meijering (2001). This involves computing the length ρ, and the angle φ, between the vector d_j of every control point p_j and the corresponding vectors d_k of the natural neighbours $p_k, k = 1, 2, N_j$, of that control point in the Delaunay triangulation, provided that both d_j and d_k are not equal to the null vector:

$$\rho_{jk} = \frac{|\mathbf{d}_j|}{|\mathbf{d}_k|}, \tag{6.13}$$

$$\varphi_{jk} = arccos\left(\frac{\mathbf{d}_j, \mathbf{d}_k}{|\mathbf{d}_j||\mathbf{d}_k|}\right), \tag{6.14}$$

Consistency is then determined by testing for the following criteria:

$$\rho_{jk} > \rho_{max} \quad \vee \quad \rho_{jk} < \rho_{max}^{-1} \tag{6.15}$$

$$\varphi_{jk} = \varphi_{max}. \tag{6.16}$$

where $\vee$ is the point wise maximum operator. Displacement vectors for which more than half of the natural-neighbour vectors cause at least one of these criteria to be satisfied, are labelled as inconsistent.

In the cases where vector $\mathbf{d}_j$ or the natural-neighbour vector $\mathbf{d}_k$ is close to the null vector, and ρ_{jk} (the difference in length between $\mathbf{d}_j$ and $\mathbf{d}_k$) is more than ρ_{max} times the precision with which the vectors are computed, $\mathbf{d}_j$ is labelled as inconsistent. The inconsistent vector is then substituted by the Gaussian-weighted average of its consistent natural-neighbour vectors according to the equation

$$\mathbf{d}'_j = \omega^{-1} \sum_i \omega_i \mathbf{d}_i \tag{6.17}$$

where

$$\omega_i = exp\left(-\frac{\|\mathbf{p}_j - \mathbf{p}_i\|^2}{2d^2_{min}}\right) \tag{6.18}$$

and

$$\omega = \sum_i \omega_i \tag{6.19}$$

where $\mathbf{d}'_j$ is the substitution vector for inconsistent vector $\mathbf{d}_j$ and d_{min} denotes the distance between control point p_j and the closest of its natural neighbours having consistent displacement vectors.

6.5 Mask image warping

Warping an image is the spatial transformation of that image. Digital warping is used to correct distortions acquired during the imaging process due to the device used or, in this case, movement between two images or both. Subpixel interpolation is a technique used in warping because often the pixel positions will not always be integer values. Nearest neighbour interpolation can be used which effectively rounds this position value but bilinear interpolation offers better results and was described briefly in Section 6.3 (Smith, 1999).

In terms of the algorithm used in this dissertation, once the entire corrected displacement vector field d has been established, each triangle $\triangle_{i,j,k}$ in the mesh $D(P)$ is deformed by using their properties and by using the bilinear interpolation of grey levels as described in Section 6.3 (Meijering, 2001).

Chapter 7

Development of the Image Subtraction Program

The program developed for this dissertation was for African Medical Imaging and has essentially been modelled on the algorithm proposed by Meijering (2000).

The main objective of this program was a means for ascertaining the feasibility of incorporating this tool into Lodox and to test the theory outlined in the dissertation itself rather than the development of a final stage implementation tool. Thus, in the future, improvements can be implemented to ensure faster and more accurate results.

7.1 Program overview

Figure 7.1 provides an overview of the program developed which aims to register and subtract two digital x-ray images obtained through Lodox technology. The resulting image should clearly show the peripheral blood vessels into which contrast medium was injected. A number of artefacts have been eliminated and, although not optimised at present, could definitely be achieved in a future project as mentioned earlier.

The program begins by loading the DICOM images acquired through Lodox into the Matlab environment. At this stage the images look like the one illustrated in Figure 7.2. The inverted image is shown here as the non-inverted version is too dark to

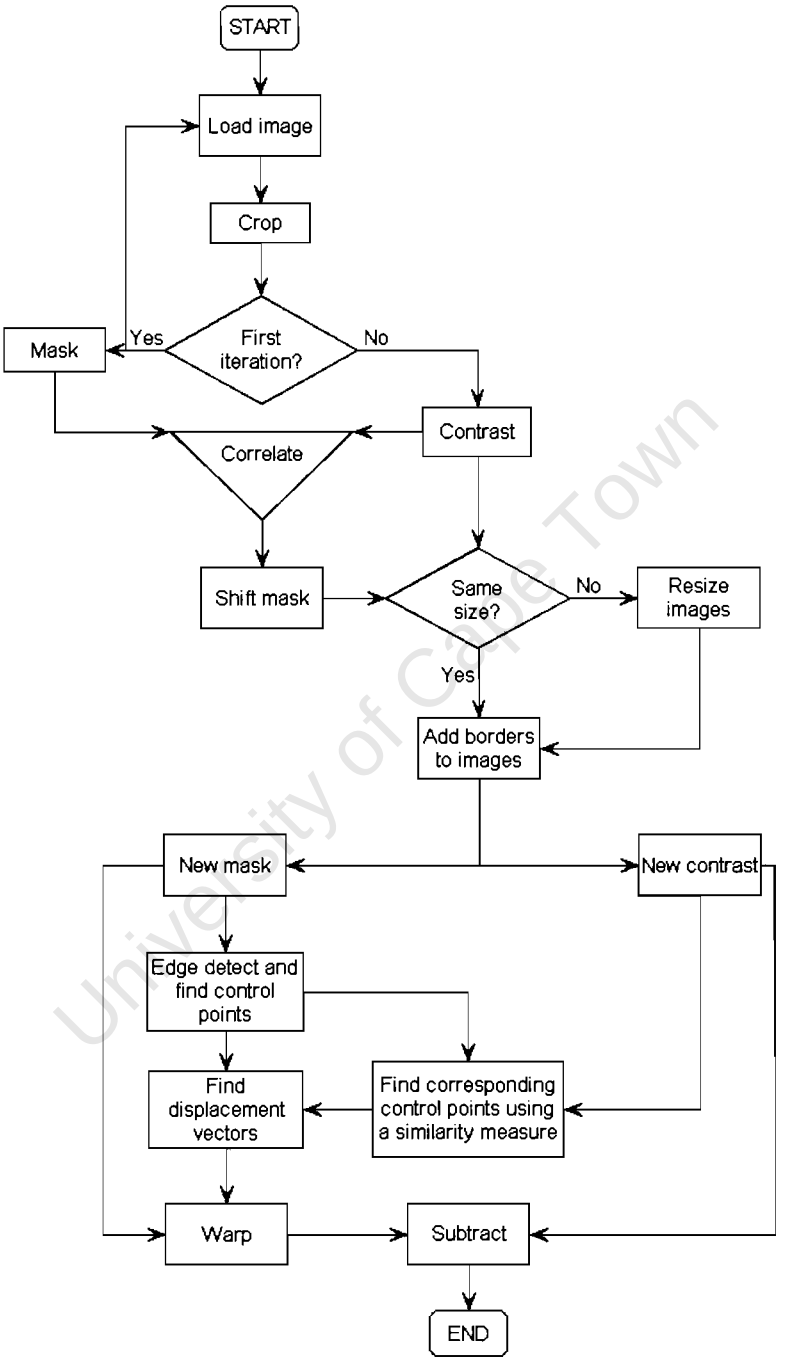

Figure 7.1: Overview of the program developed.

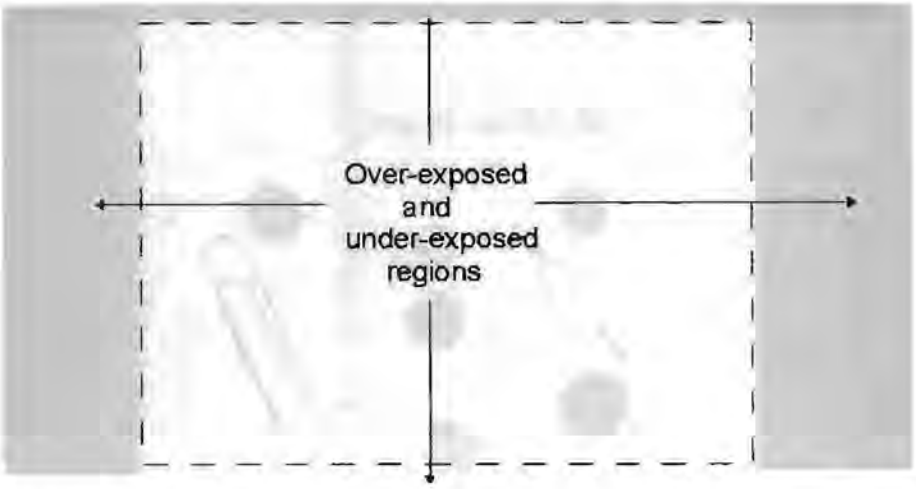

Figure 7.2: An inverted version of the 'raw' mask image loaded into the Matlab environment.

distinguish the contrast differences. The over-exposed and under-exposed regions seen predominantly on the right and left sides of the image affect the grey level scaling for display in Matlab. The images are therefore not too clear and since these areas are superfluous in the registration process, thus adding to computational cost, they were removed. An automatic cropping procedure proved to be a more complicated and arduous task than expected and often the results were not accurate enough or consistent enough for the registration procedure. Some of results of tests carried out between the automatic and manual cropping procedures on which this decision was based may be observed in Appendix D. Cropping was therefore predominantly performed manually.

Figure 7.3(a) shows a cropped and grey scaled version of this same image and Figure 7.3(b) the cropped contrast image. Although the overall pixel grey values are unchanged, it is easier to see the smaller changes in contrast. Figure 7.4 shows a subtraction of the two images at this point to indicate the difference in the structures' positions due to movement of the phantom between scans.

The cropped images were then correlated (global match – see Section 6.4.1) to adjust for larger scale movement changes i.e. those that are greater than 51 pixels. The more local processing for correction of finer movement changes makes use of a template of size 51 x 51. If the movement at this stage is larger than 51 pixels, the position will not be found as it will be not be contained in the search area. Correction

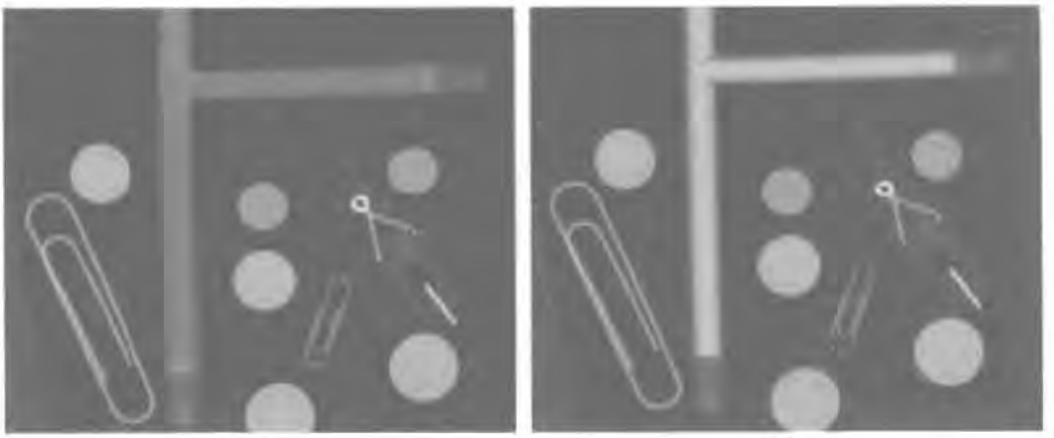

(a) (b)

Figure 7.3: (a) The cropped mask image and (b) the cropped contrast image.

Figure 7.4: The cropped mask and cropped contrast subtraction image prior to any processing.

for movement greater than 51 pixels is therefore carried out at this point. Images related to the testing of this translational correction can been seen in Appendix C.

The next stage involved the addition of borders (of zeros) around the image perimeter for the warping process utilised later. Figure 7.5 shows the bordered mask and bordered contrast images obtained. After the borders were developed and added, a set of border points were selected along its inside and outside perimeters Dmin pixels apart. Figure 7.7(a) only shows the inner perimeter points obtained. Following this, an initial set of control points was extracted from the exposure region, R_{exp} (see Figure 7.6). This was a multi-part operation involving the image edges because, as pointed out by Meijering (2000), these are the regions most prone to image artefacts in the subtraction process.

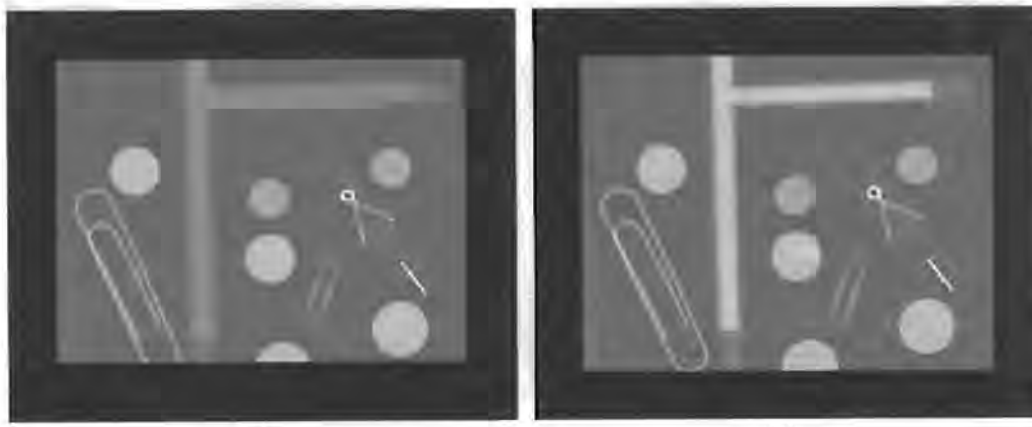

(a) (b)

Figure 7.5: (a) The mask image obtained with a border for later processing. (b) The bordered contrast image.

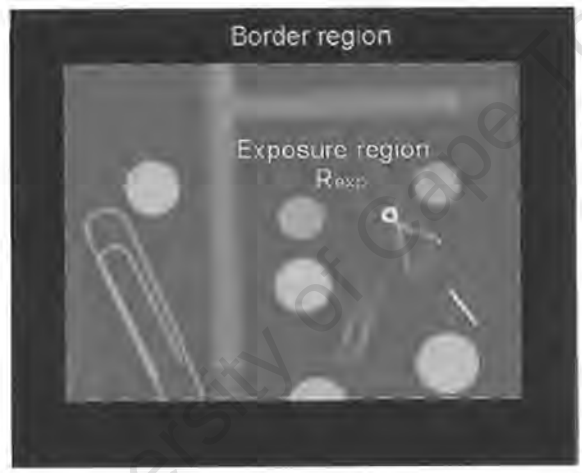

Figure 7.6: Image showing the exposure and border regions.

The Canny edge detection was used (see Chapter 6) for obtaining these edges in the mask image. The variable values used included a filter width value of σ (stated in Table 7.1) that was found on a trial and error basis and an upper and lower threshold value of T_U and T_L respectively. The latter two values were determined automatically by the Matlab inbuilt 'edge' function used with $T_L = 0.4T_U$.

The mask image was used in this process because it contains information that is common with the background information in the contrast (i.e. the regions not highlighted with contrast). This common information is what is needed in order to establish the differences between the two images and so compensate for this movement to align

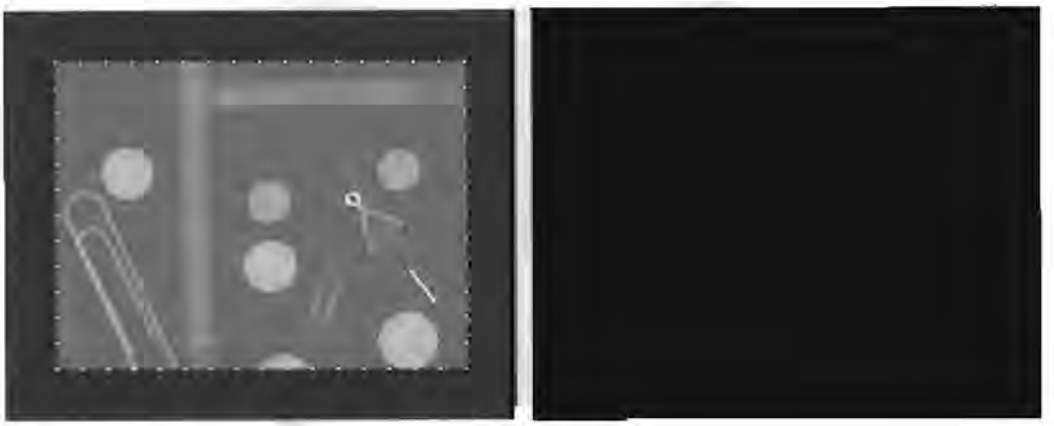

(a) (b)

Figure 7.7: (a) The inner perimeter border points selected from the mask image. (b) The edge image of the mask from which the control points will be found.

them. Figure 7.7(b) shows the edge-image of the mask. Once the edges of the image were obtained, an initial set of control points was extracted.

This process involved dividing the edge image up into a series of square blocks of size Dmax x Dmax as illustrated in Figure 7.8(a).

Each block was processed in turn by firstly dividing it (the Dmax x Dmax block) into a "grid" of smaller blocks, or templates, of size Dmin x Dmin as in the former case above. This is highlighted in Figure 7.8(b) - in the final selection of control points, a point must be no closer than Dmin from any of its natural neighbours and no further than Dmax away from them. An iteration will now be described.

Table 7.1: Table showing parameter values used in the program developed. These values were investigated by Meijering (2000) and Buzug *et al.* (1998).

PARAMETER	VALUE	PARAMETER	VALUE
Dmin	51	K	51
Dmax	204	L	51
mindist	102	σ	0.55

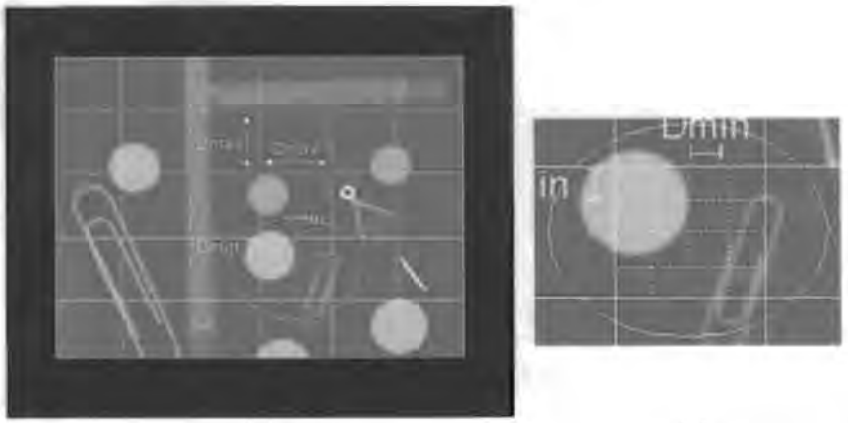

(a) (b)

Figure 7.8: Regions extracted for the template match procedure. (a) shows the Dmax x Dmax regions extracted. The encircled region is enlarged in the adjacent figure (b), to show an example of the Dmin x Dmin selected regions from one Dmax x Dmax block.

After the template has been extracted, the program determines whether it contains any edges. If it does not, a central point is chosen as a control point for that template. In the instance that the template does contain an edge, the template's grey scale equivalent is multiplied by the edge template so that the edge's actual grey values are established. The pixel chosen as the control point is then the pixel that displays the brightest value as an estimate to a sharpest possible edge. All the blocks and templates are worked through in this manner to obtain all the control points. Figure 7.9(a) shows an initial set of control points selected along the edges.

The next step was to refine this set of control points. This improves the computational load and eliminates superfluous points that are too close together and might complicate the formation of triangles in the triangulation phase. This process involves an analysis of the initial set of control points so that the points selected are no closer than Dmin apart and no further than Dmax from their nearest neighbours. The border points take priority and then each point in the exposure region is considered in turn. The results of this process are shown in Figure 7.9(b).

Points corresponding to the control points need to be determined in the contrast image. To do this, template matching was used in conjunction with the difference of histogram similarity measure (see Chapter 6). Figure 7.11 illustrates this process with Figure 7.12 depicting what the algorithm "sees" (to varying degrees) when there is a good or bad match. The two graphs show the resulting histograms of an ideal

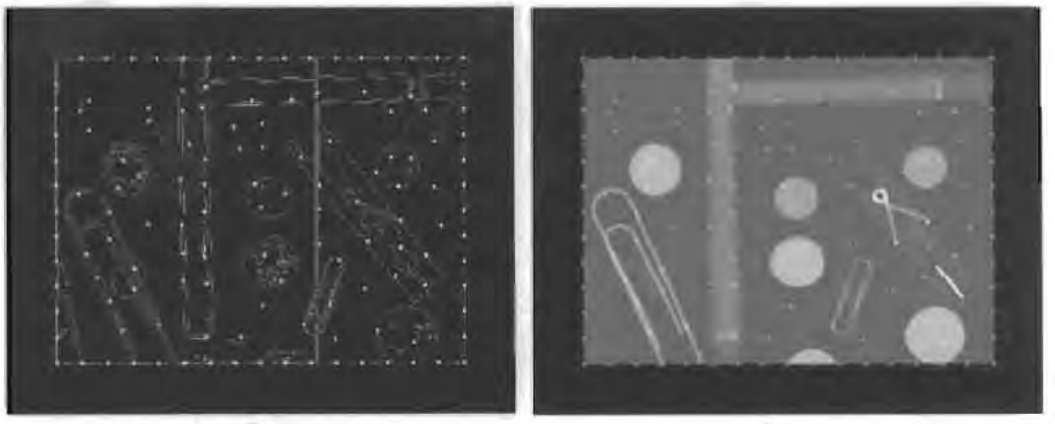

(a) (b)

Figure 7.9: (a) Initial control points obtained along the image edges with the inner perimeter border points. (b) The crossed points indicate the selected control points based on the minimum and maximum distance constraints of Dmin and Dmax respectively.

mismatch and match. This process is the most computationally expensive routine in the program.

Once the contrast's control points are found, the displacement vector field is calculated. When experimenting with this process, however, spurious vectors were corrected for with an example of the results depicted in Figure 7.10 where Figure 7.10(a)shows a few inconsistent vectors and Figure 7.10(b) shows them corrected for.

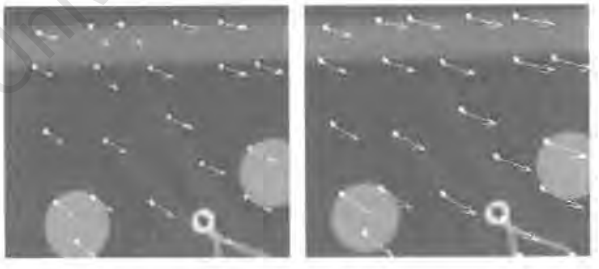

(a) (b)

Figure 7.10: (a) a section of the mask image with inconsistent vectors present. (b) shows the results of correcting for the inconsistent vectors using the Gaussian weighted average values of their consistent natural neighbours.

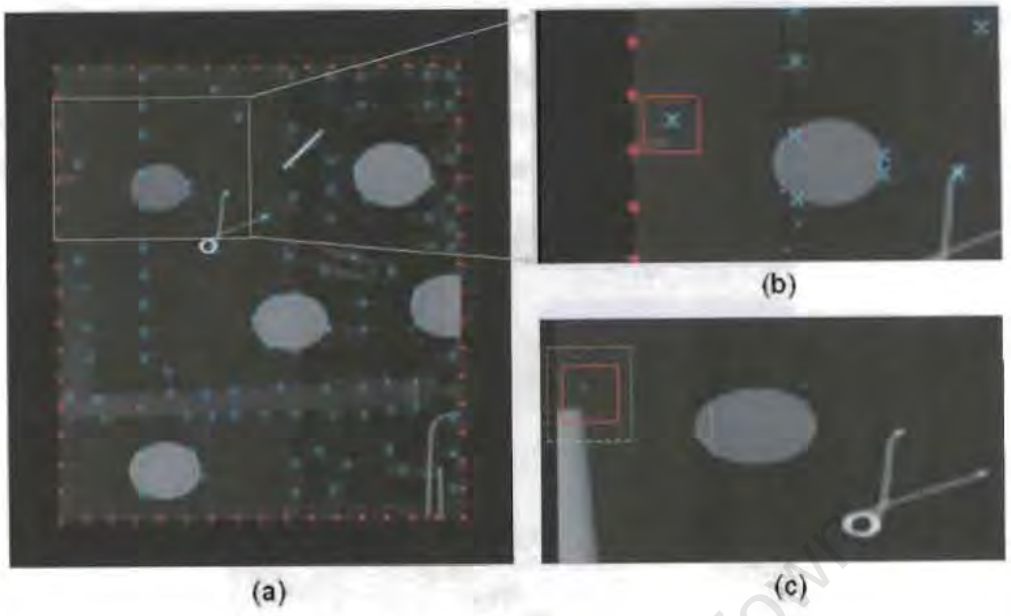

Figure 7.11: Figure (a) illustrates a section of the mask image showing the region from which a control point will be selected in order to find its correspondent in the contrast image. (b) Shows the control point selected by the red box whose co-ordinates will be estimated. (c) The green box shows the vicinity in which the search will be carried out in the contrast image while the red box shows the point of best fit that was determined using the histogram of differences similarity measure.

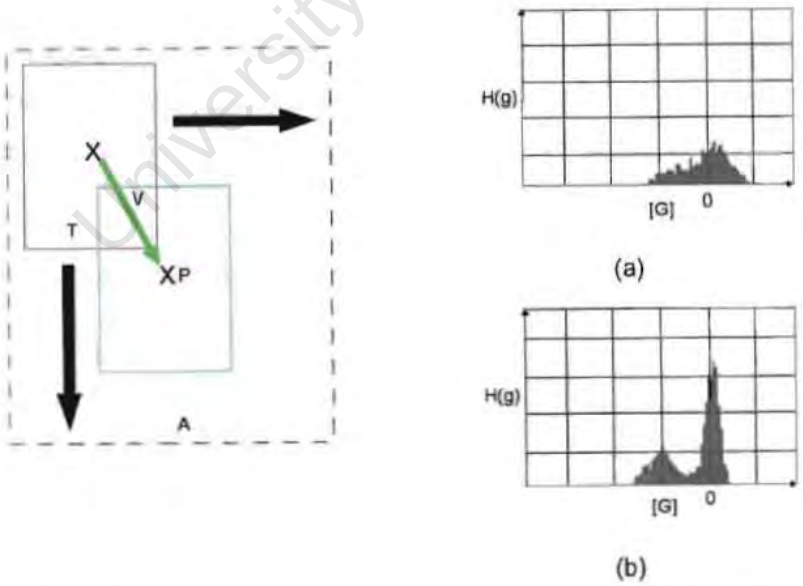

Figure 7.12: The displacement vector development concept – an extension from Figure 7.11(c). Figure (a) indicates "bad" match characteristics (i.e. when the template T containing control point X is positioned anywhere other than on point P. (b) indicates "good" match characteristics (i.e. when template T containing control point X is positioned on point P.)

by the Gaussian-weighted averages of its consistent natural neighbours as a substitute. The vectors are magnified in these figures for clarity. In the final program, inconsistent vectors were not corrected for as outlined in Chapter 6 which would partly account for a certain lack of accuracy in the results.

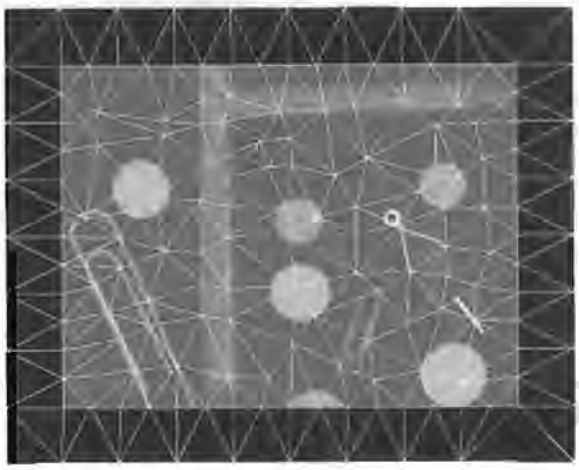

Figure 7.13: The Delaunay triangulation.

Using the Delaunay triangulation interpolation method, a transform was formed that was used to warp the mask image by deforming each triangle of the mesh. This was accomplished by moving the vertices by the displacement vector values of each control point and then interpolating the intermediate points of that triangle using the transform developed. The mask image was therefore warped triangle by triangle and resized before it was subtracted from the contrast image. The warped image is shown in Figure 7.14 and a few warped features are highlighted in Figures 7.14(a) and 7.14(b).

Figure 7.15 shows the results from the final subtraction. The results of the trials and tests run can be seen in Chapter 8.

7.1.1 Summary

This algorithm is based on that developed by Meijering (2001) and so this summary holds:

1. Calculate the gradient magnitude using canny detector with threshold of the mask image.

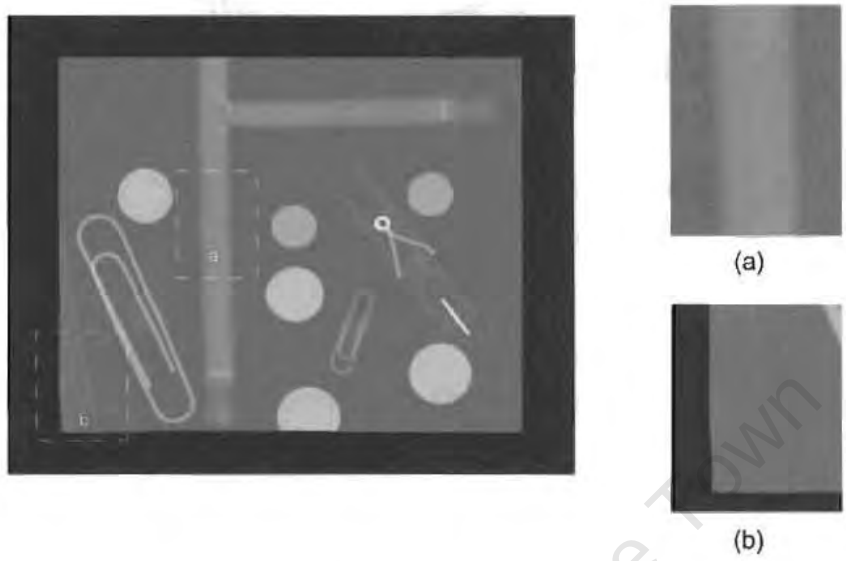

Figure 7.14: The warped mask image. Sectioned regions are magnified in (a) and (b).

Figure 7.15: The final subtracted image.

2. Extract a border around image and select border control points.
3. Extract control points in the exposure region R_{exp} using minimum and maximum distance constraints, Dmin, Dmax and mindist between neighbouring pixels.
4. Construct a triangular mesh using the incremental Delaunay triangulation algorithm with the control points obtained above.
5. Calculate the displacement vectors for the two images by maximising the energy of the histogram-of-differences similarity measure M from equation 6.12 in a KxL neighbourhood of these points.
6. Detect inconsistent vectors by computing the length of and angle between all vectors and their corresponding natural-neighbour vectors and by testing the criteria described in Section 6.4.6.
7. Correct inconsistent vectors by substituting them with a Gaussian-weighted average of the consistent natural neighbour vectors according to the equations in Section 6.4.7 of Chapter 6.
8. In order to obtain the motion corrected subtraction image corresponding to the contrast image, the mask image must be warped by deforming every triangle in the mesh. This can be done by using the displacements of the constituent control points and the linearly interpolated displacements at the remaining points in the image. Following this the linear interpolation of the grey values can then be used to account for grey level disparities.

7.2 Limitations and comments

It was later found that the results were in fact better when much smaller borders were added. Some results of tests conducted between the two different border widths may be observed in Appendix D. The padding added to make the images divisible by Dmin for the template matching and difference of histogram procedures was found to be more suitable. Figure 7.16 shows an example of the new borders used for the mask and contrast images.

The author did not implement the weighting of control points nor the error correction principle outlined in Chapter 6 and for the purposes of time reduction did not strictly

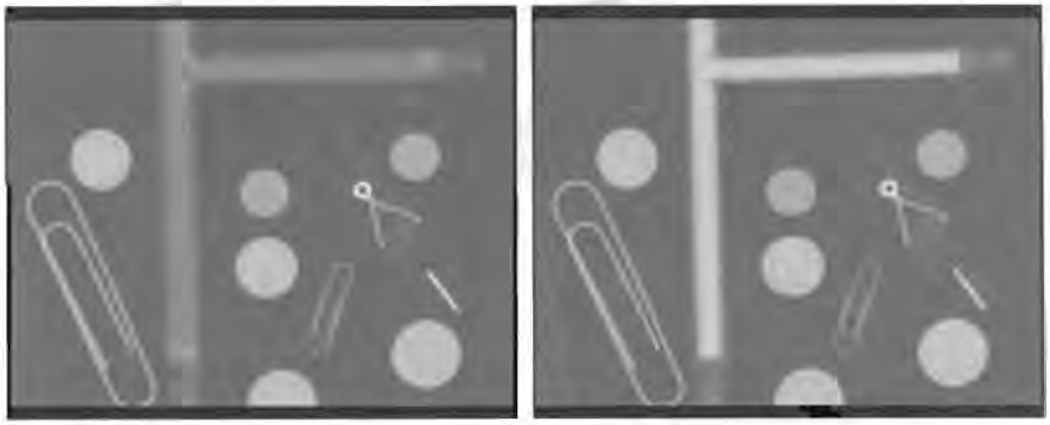

(a) (b)

Figure 7.16: Figure showing (a) the mask and (b) the contrast images with the smaller border widths that gave better results.

use the difference of histogram similarity measure in the final implementation. Prior to the final implementation the author did experiment with this measure but the time to run a single program far outweighed the results achievable using Matlab. The time taken to complete the program – that point at which the final subtracted image is displayed – varies depending on the input image size. When using the image shown in this chapter, the T-tube trial, the time to completion is just under 2 minutes (01 minute 54 seconds), while the experimental program using the difference of histogram measure took about 15 hours. This wait was not considered viable. However, with the use of a different programming language and dedicated hardware, it could be used to provide more accurate images in substantially less time.

This project was implemented using Matlab. The implementation was obviously not optimised for speed as mentioned earlier. A much faster more efficient version could be easily implemented using C or C++ and by incorporating dedicated hardware.

One of the main assumptions made is that gross patient motion is kept to a minimum. Should the movement be too severe, the search windows chosen will be too small, resulting in inaccurate displacement vectors. This in turn will have an effect on the warping process, thereby affecting registration and increasing the possible artefacts in the subtracted image. Larger search windows will result in a considerable increase in processing time. According to Buzug *et al.* (1998) the optimal size window should be of the order of 51 pixels square.

Chapter 8

Results

In this chapter different system parameters described in the previous chapters are documented. All the information in question could not be obtained but the reasons for this are discussed in Chapter 9. The hardware, software and imaging characteristics of the systems are therefore provided where possible. Following this, the phantom and patient trial findings are presented in conjunction with the program efficiency. Finally, the questionnaire that was directed towards clinical staff with both Lodox and conventional x-ray experience is included.

8.1 DSA system component comparison results

As mentioned in Chapter 3, subtraction of the image "background" remains a function of primary importance in any DSA system. The quality and limitations of each component of the system may vary among machines from different manufacturers, but essentially each performs a similar task. The digital system specifications for the Philips Integris Allura and the Toshiba Infinix VC angiography machines will be used as the basis for comparison with the Lodox system. From this, it will be possible to ascertain whether or not additional components need to be incorporated into the Lodox system to allow it to perform DSA successfully.

(a) (b)

Figure 8.1: (a) The Philips Integris Allura (Philips Medical Systems, 2002a) and (b) Toshiba (Toshiba, 1995) angiography systems.

8.1.1 Commercial systems

In commercial DSA systems, images are taken at specific intervals, producing a set of scans (frames). The clinician is then expected to find the "best fit" manually with the use of the cursor buttons, situated on the control console, to shift the mask image in order to improve alignment between it and the contrast image prior to subtraction. This simple correction is usually performed within a few seconds if performed by an experienced clinician. Automatic registration will therefore only be considered feasible if it can be performed at least as fast as the manual procedure.

In this section two commercially available angiography system specifications are investigated with a particular focus on the DSA capabilities of each system. The information has been collected from various sources: the Philips Integris Allura (Figure 8.1(a)) from ECRI (2001); Tremp (2002); Philips Medical Systems (2002a); den Boer *et al.* (2002) and Philips Medical Systems (2002b) ; the Toshiba Infinix VC (Figure 8.1(b)) from Toshiba (1999) and Hauschild (2002) and the Lodox system from De Beers (2001); Hering and Maree (2003); Lodox Systems (2002); Flash (2002) and Schindehutte *et al.* (1998). The Lodox system will be described in a separate section due to its construction differences.

Fluoroscopic sub-system

X-ray generator and tube

The generator of the Philips Integris Allura gives a maximum output power of 100 kW with a voltage range of 40 kV to 150 kV and a maximum amperage of 1250 mA. The Toshiba generator provides a power output of 100 kW to the tube with a voltage range from 50 kV to 125 kV and amperage range of 100 mA to 1250 mA.

The Philips Allura offers two focal spots of size 0.3 mm and 1.0 mm while the Toshiba tube has three focal spots that range in size from 0.3 mm to 1.3 mm.

Image intensifier and the Television system

The Philips Integris Allura offers a range of intensifier sizes for various applications. The sizes range from 17 cm to 38 cm with resolution ranges from 3.6 lp/mm to 6.2 lp/mm. The intensifier sizes for the Toshiba range from 13 cm to 40 cm with resolution ranges of 3.6 lp/mm to 5.8 lp/mm. Both the Philips Integris Allura and the Toshiba make use of CCD technology.

Image processing sub-system

The analogue-to-digital converter (ADC)

The Philips Integris Allura and the Toshiba both support bit depths of 9 and 10 bits (516 to 1024 grey levels). They offer frame rates of up to 60 fps for 9 bit images and up to 30 fps for 10 bit images. The sampling frequency of the Philips is of the order of 40 MHz while the Toshiba provides a much lower sampling frequency of 4.4 MHz.

Image processor and viewing station

The process of image registration and subtraction may be performed in the image processor (IPP) as well as correction of errors in images that are associated with the image capture and conversion. These images are then displayed on the viewing station. The digital viewing station (DVS) allows for basic image enhancement carried out by the clinician. The system capabilities offered by the Philips and Toshiba systems are summarised in Table 8.2 and are fairly standard.

Archiving of DSA images

Both systems are DICOM 3.0 compatible with the Philips Integris Allura providing 36 GB with optical disk storage and the Toshiba, 32 GB of storage space with digital VCR, CD-R and magneto-optical disk storage facilities.

X-ray exposure, dose and noise

Toshiba figures for the patient entrance dose rates were not available but it was assumed that they were within the FDA approved dose rate of 10 μGy. Philips gave an entrance patient dose measurement of 5,10,20 μGy/s depending on the mode used. At 6 fps they gave a entrance dose of 1.2 μGy/s as a reference value i.e. without any filtering. These values were obtained at 30cm from the image intensifier. The user dose rates were taken at eye level (about 67cm above the table height) with lateral projection and gave a reference dose of 0.325mGy/h. With filtering they have managed to decrease the dose rates by as much as 55% (den Boer *et al.*, 2002).

8.1.2 Lodox

A brief history

In 1999, Debex (Pty) Ltd, a subsidiary of De Beers South Africa, developed a low dosage x-ray machine called Lodox-MP (**LO**w **DO**sage **X**-ray - **M**edical **P**rototype) (Figure 8.2). A unit was initially installed in the trauma department at Groote Schuur Hospital in Cape Town in June of that year and a later model, Lodox-LACT (**LO**w **DO**sage **X**-ray - **L**imited **A**ngle **C**omputer **T**omography), in the Health Sciences Faculty of the University of Cape Town during April 2001. The uniqueness of Lodox lies in its ability to produce high definition x-rays at a considerably lower radiation dose than that of conventional and other digital x-ray machines currently available. This is beneficial to both the patients and the clinical staff concerned. Its value as an aid to trauma specific applications is discussed in Chapters 2 and 9 of this dissertation.

The Lodox unit consists of the x-ray scanner, a viewing and operating console and an electronics cabinet. An ionising x-ray emitting tube and a charge coupled de-

Figure 8.2: The Lodox system (Lodox Systems, 2002).

vice (CCD) detector array are mounted on either end of a C-arm that is connected to a base frame which in turn is attached to the floor and/or ceiling. A specifically designed patient trolley is capable of docking with the base frame, thus preventing it from moving and affecting the quality of the images scanned. The C-arm of the Lodox system is capable of rotating from zero through 90 degrees but only scans in one direction - along the length of the trolley. As the C-arm traverses the length of the trolley, the distance travelled having been specified by the user, the x-ray tube emits a fan beam of x-rays that are captured by the detectors using the time delay integration (TDI) technique (explained in Appendix B). The images are subsequently reconstructed and displayed by the image pre-processor computer and the diagnostic viewing station computer respectively. Interactive trackball and menu controls permit window level and width adjustments together with patient identification information display. The machine allocates exposure rates according to preset settings depending on body size and region chosen by the clinician for imaging. Lodox is capable of performing a full body scan in under 14 seconds.

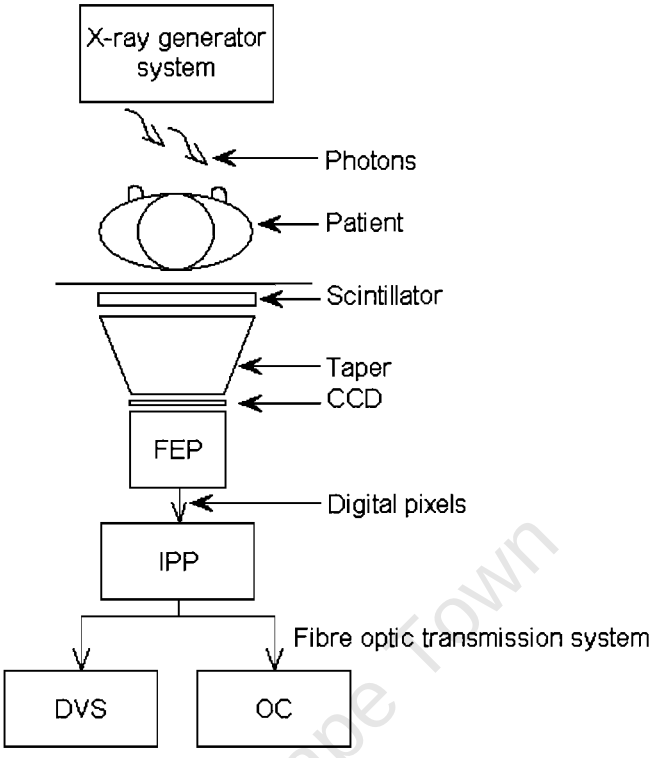

Figure 8.3: A block diagram of the Lodox system. Here CCD are the charged couple devices, FEP is the front end processor, IPP is the image preprocessor, DVS is the digital viewing station and OC the operator console

Fluoroscopic sub-system

X-ray generator and tube

The x-ray source assembly of the Lodox system consists of an x-ray tube, collimator, shutter and light source. The generator is capable of supplying and maintaining 30 kW of power to the tube and has an adjustable output in the range of 50 kV to 150 kV and 200 mA to 600 mA. The x-ray tube has two focal spots of size 0.7 mm x 0.8 mm and 1.2 mm x 1.4 mm.

Image capture unit

A detector box holding 12 CCD cameras is responsible for detecting the light from the scintillators (Appendix A). The Lodox system does not utilise image intensifiers as do the standard angiography systems. Instead it makes use of scintillators that absorb the x-rays and convert them into visible light. Fibre-optic tapers then focus this light information onto the CCDs. This effectively minimises the image-to-CCD size.

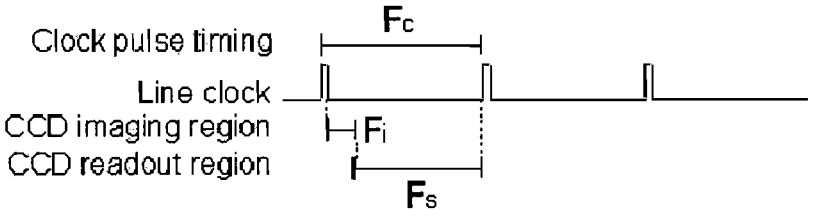

Figure 8.4: A schematic describing the timing allocation of various variables in the image capturing processes of the Lodox system.

Resolution is limited by the CCD size and the point spread function of the scintillator. The thickness of the scintillator influences the x-ray conversion. A thin scintillator will lessen the x-ray conversion, thereby increasing the resolution image distortion of the fibre optic noise in the CCD and electronics circuits. Scintillators like the one used in Lodox, such as CsI (Caesium Iodide), are useful for their large collecting areas and their high quantum efficiency above 20 keV (Hahn *et al.*, 2002).

Image processing sub-system

The analogue-to-digital converter (ADC)

The ADC is found in the detector headboard electronics. It converts the analogue signal into a 14 bit digital signal, with a sampling frequency of 2.75 MHz, which is then sent to the front end processor (FEP) which in turn transmits it to the image pre-processor (IPP) for data correction. In the line clock pulse (refer to Figure 8.4) a pulse is triggered every 360 to 420 μs (F_c) activating the CCDs to read in x-ray information. Between this pulse and the next, the CCD image is read into the register (F_i) and shortly afterwards read out of the output register into memory. It is during this latter stage (F_s) that the necessary sampling frequency is determined.

Image pre-processor (IPP) and digital viewing station (DVS)

After image correction, the Image Pre-Processor (IPP) passes the image to the diagnostic viewing station and the operator console. Here the clinician is able to adjust the image properties to provide a better view of the image as required. The operations available on the Lodox system can be referred to in Table 8.2. A few are mentioned here and include:

Zoom functions: these include a function to rotate the image in various directions.

Image manipulation: unsharp masking - flattens the image so that no grey-scale adjustments are necessary.

Palette function: enables the user to independently manipulate the grey scales.

Invert function: changes the view from a "black bone" to a "white bone" image.

Archiving of DSA images

Lodox is DICOM 3.0 compatible and provides at least 20 GB of storage space and CD-R capability. Once the available space on the hard drive is full the oldest images by date are

Contrast sensitivity, spatial and temporal resolution

Lodox is capable of processing 14 bit images which implies a grey level range of 16,384 grey levels. The spatial resolution is variable and depends on the scan mode selected. There are four modes available: normal, high, ultra-high and test. The differences lie in the binning process. Each pixel is 60 μm x 60 μm in size. These may be binned in 5 x 5, 3 x 3, 2 x 2, 1 x 1 averages, effectively producing larger pixels. Normal mode employs 5 x 5 pixel binning and offers a resolution of 0.67 lp/mm, high mode uses 3 x 3 pixel binning and gives a resolution of 2.88 lp/mm, ultra-high rnode allows 2 x 2 pixel binning, while in test rnode there is no binning. The latter two modes provide resolutions of 4.1 lp/mm and 8.31 lp/mm respectively. The time taken to complete a full body scan is 13 s and the delay time between scans is about 30s (Schindehutte *et al.*, 1998; Lease, 2001; de Villiers and de Jager, 2002). de Villiers and de Jager (2002) calculated the MTF of the Lodox system by firstly differentiating the edge spread function (ESF) of the system to obtain the PSF. The modulus of the Discrete Fourier Transform (DFT) of the PSF then provides the MTF values (de Villiers and de Jager, 2002). These values/curves can be seen in Figures E(a) through E(d) in the Appendices for each binning mode (1 x 1, 2 x 2, 3 x 3, 5 x 5 pixel binning). These values were not obtainable from the various manufacturers and so a comparison between the systems could not be made.

Table 8.1: Acceptable dose rates according to the FDA and those of Lodox (De Beers, 2001).

ENTRANCE DOSE [mGy]		
RADIOGRAPH	**FDA**	**Lodox**
LUMBAR SPINE (AP*)	5-7	0.2
CHEST (AP*)	0.08-0.3	0.1
HAND	0.05-0.3	0.025
SKULL	1-3	0.2

* antero-posterior view

X-ray exposure and dose and noise

The x-rays are adjustable from 60 kV_p to 160 kV_p. According to De Beers (2001), the maximum absorbed dose is 1 mGy (Schindehutte *et al.*, 1998), a patient entrance dose of 40 - 338 μG. The user dose rates were taken at eye level (about 67cm above the table height) with lateral projection and gave a reference dose of 0.7 - 2 μSv (or μG) (Flash, 2002; Hering and Maree, 2003). A SNR of at least 3 or higher is maintained at the detector to minimise the effects of quantum noise. This requires that the number of electrons in different stages of the camera must never drop below the number of x-ray photons detected. Image size is limited in order to reduce the low energy scatter electrons reaching the scintillator (Schindehutte *et al.*, 1998).

Table 8.1 sets out a comparison between the Food and Drug Administration (FDA) approved dosage rates for specific scans and the rates obtained by the Lodox system when performing those same scans. For a lumbar spine and skull scan, the FDA approved dose range is 5 - 7 mGy and 1 - 3 mGy respectively, with the Lodox giving a dose of 0.2 mGy in both instances. For chest and hand x-rays the FDA approved dose range is 0.08 - 0.3 mGy and 0.05 - 0.3 mGy respectively. Lodox comparative doses measure 0.1 mGy and 0.025 mGy for chest and hand scans respectively (Schindehutte *et al.*, 1998).

8.1.3 System comparison

Table 8.2 summarises the information from sections 8.1.1 and 8.1.2.

Table 8.2: Comparison table of two commercial DSA systems and Lodox.

MODEL	**PHILIPS** INTEGRIS ALLURA	**TOSHIBA** INFINIX VC	**Lodox** MP
PARAMETERS			
X-RAY GENERATOR	100 kW	100 kW	43 kW
POWER OUTPUT	40 - 150 kV 10 1000 mA	80 - 150 kV 630 - 1250 mA	125 kV (max) 300 mA (max)
X-RAY TUBE			
Material	Rhenium-tungsten		Rhenium-tungsten
Focal Spot [mm]	Two spot sizes: 0.3 and 1.0	Spot size range: 0.3 - 1.3	Two spot sizes: 0.7 x 0.8 1.2 x 1.4
IMAGE INTENSIFIER	40 cm - 4 lp/mm 31 cm - 4.6 lp/mm	13 - 31 cm 42-58 lp/mm	Not applicable
CAMERA TYPE	CCD	CCD	CCD
ADC			
Bit depth	10 bits	10 bits	14 bits
Sampling frequency	40 MHz	4.4 MHz	2.75 MHz
IMAGE MANIPULATION			
Edge enhancement	yes	yes	yes
Filtering	yes	yes	no

continued on next page

MODEL	PHILIPS	TOSHIBA	Lodox
	INTEGRIS ALLURA	INFINIX VC	MP
PARAMETERS			
Pan and or zoom	yes	up to 5x	yes
Roadmapping	yes	yes	no
Landmarking	yes	yes	no
Remasking	yes	no	no
Reregistration	real time	no	no
Region of interest(ROI) selection	mouse	no	no
Window and levels	yes	yes	yes
Replay	yes	yes	image recall
Invert function	yes	yes	yes
Pixel shift	yes	yes	no
ARCHIVING/STORAGE	36 GB (max) Optical disk Lazer imager Digital VCR	32 GB (min) Digital VCR CD-R Magneto-optical disk DVD-RAM	20 GB (min) CD-R
DICOM 3.0 COMPATIBLE	yes	yes	yes
CONTRAST SENSITIVITY	10 bits	8 - 10 bits	14 bits
Grey levels	1024	1024	16384
SPATIAL RESOLUTION	3.6 - 6.2 lp/mm	4.2 - 5.8 lp/mm	0.67 - 8.3 lp/mm
TEMPORAL RESOLUTION	15 - 60 fps for 512 x 512 images 7.5-30 fps for 1024 x 1024	60 fps (max) for 512 x 152 images 30 fps (max) for 1024 x 1024	Not applicable

continued on next page

MODEL	PHILIPS	TOSHIBA	Lodox
	INTEGRIS ALLURA	INFINIX VC	MP
PARAMETERS			
	images	images	
SNR	80 dB	60 dB	47 dB (min)
DOSE RATES			
PATIENT			
Mean Entrance Dose	1.2 μG/s	Not Available	40 - 338 μG
ATTENDING STAFF			
Max Dose	0.325 mG/h	Not Available	0.7 - 2 μGy

8.2 Blood flow velocity

At the outset of this thesis, the ability of Lodox to perform arterial imaging was questioned. If the velocity at which the C-arm of the Lodox system moves is too slow (the maximum velocity of the C-arm is 140 mm/s), the bolus flowing in the blood will dissipate too quickly for acceptable image contrasts to be obtained. In this case only venous imaging would be considered. Referring to Table 8.3, the average blood flow velocities at various anatomical locations in the body of a 70 kg man are tabled as found in a study conducted by Milnor (1989). It shows the blood velocity values associated with the main vessels of the trunk and those that feed the peripherals. Blood flow in the renal arteries blood flow has the highest velocity at 400 mm/s followed by that in the inferior vena cava at 210 mm/s while the blood within the femoral vein and superior vena cava have the slowest velocities at 40 mm/s and 90 mm/s respectively. Of interest is the femoral artery which exhibits an average velocity of 140 mm/s since this is a peripheral vessel that will be used to ascertain Lodox's ability to perform DSA.

Table 8.3: Table showing normal average blood flow velocities for a 70 kg man as referenced from Milnor (1989).

SYSTEMATIC VESSELS	VELOCITY (mm/sec)
Ascending Aorta	180
Descending Aorta	140
Renal Artery	400
Femoral Artery	120
Femoral Vein	40
Superior Vena Cava	90
Inferior Vena Cava	210

8.3 Phantom and Patient trials

Trials were conducted in order to test whether Lodox could practically carry out the DSA process and thereby confirm or negate assumptions and statements made in the previous chapters. These trials involved multiple phantoms and one trauma patient. Patient trials were not easy to obtain in the time span allocated for this thesis and therefore at this stage only one exists and it is included in this study. It is anticipated that more patient trials will be conducted in future to continue to test the system. This chapter sets out the methods and results of these trials, beginning with the first tube phantom used to develop the program, progressing onto a more formal phantom of a femur and finally, the patient trial.

8.3.1 Phantom trials

The two phantoms gave results pertaining mainly to gross and linear motion and were helpful in the program developmental stages of this dissertation. They were a T-tube phantom and a femoral phantom obtained from the radiology department at Groote Schuur Hospital.

T-tube trial

The first tests were conducted on a phantom consisting of masonite board with a clear T-shaped tubing attached to it and other circular and odd shaped objects exhibiting different radio-opaque properties. This phantom can been seen in Figure 8.5 and its acquired images in Figures 8.6(a) and 8.6(b). These images were used in the program development stage in particular. Because of the board's rigidity, only fairly gross translational movement was obtainable at first. Later, the board was warped and this gave a better perspective into a 3-D change in image information between the two scans. In this T-tube trial the main aim was to ascertain how much of the common information of the two images could be eliminated due to a fairly gross change in position between scans. Gross change is a relative measure but in this case it refers to a translation or rotation that will exceed the K x L pixel window width (search area) used in the processing procedure.

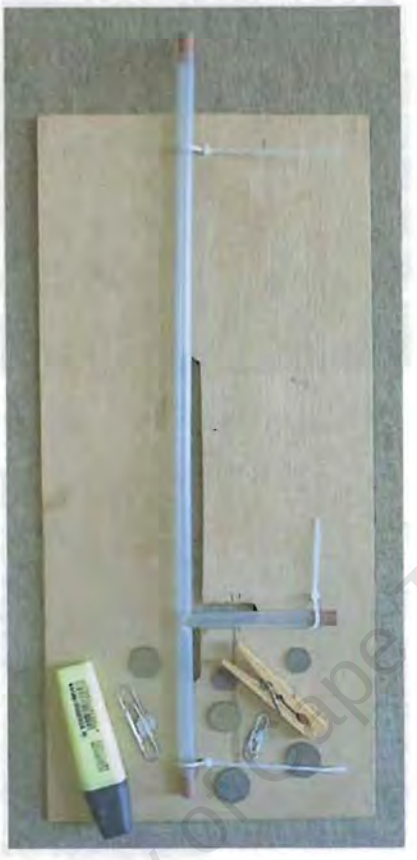

Figure 8.5: The masonite board with various objects used in the T-tube trial and program development.

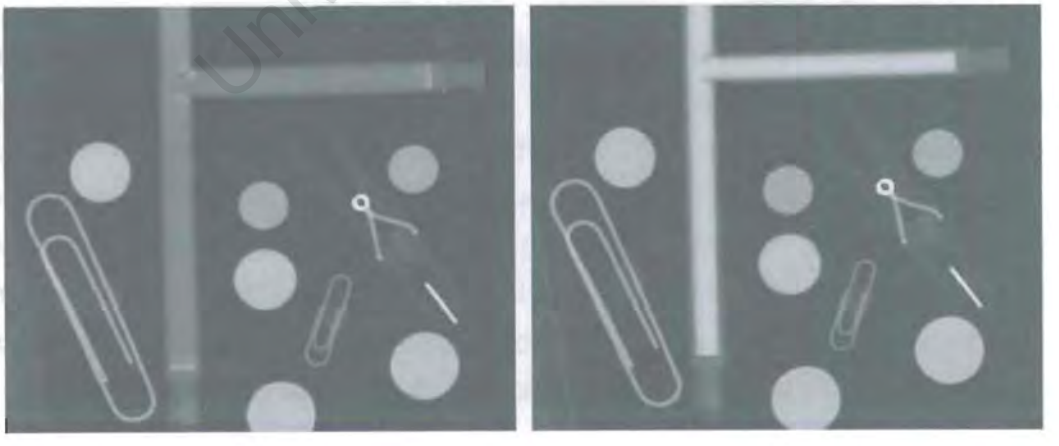

(a) (b)

Figure 8.6: The mask (a) and contrast (b) images of the T-tube trial.

Figure 8.7: An initial subtraction image before processing.

(a) (b)

Figure 8.8: (a) the final subtracted image. (b) is an inverted version of (a). The red and black lines represent two axes of rotation that are evident in the inverse image.

The initial mask and contrast images obtained were acquired as described in the final section of Chapter 2 – by scanning the objects before and after an injection of contrast medium into the tubing. Figures 8.6(a) and 8.6(b) show the mask and contrast images used in this data set. Figure 8.7 illustrates the results from the initial subtraction of the images, i.e. before any processing was performed on the images. The artefacts produced show a fair amount of shifting between the mask and contrast images. Figure 8.8(a), the processed subtraction image, is a vast improvement on the image in Figure 8.7, although it is not entirely clear of all artefacts.

The inverted views (such as in Figures 8.8(a) and 8.8(b)) sometimes offer a better perspective on the artefacts incurred during the processing and the subtraction stages, allowing for better clarity in the viewing of the contrast filled spaces. In this

case it reveals more clearly the axes of rotation that have resulted from the warping of the phantom that were not corrected for in the program. Two of these axes are indicated by the red and black lines in Figure 8.8(b).

The Matlab program took 01 minutes 08 seconds (Tables 8.4 and D.1) to run.

Femur-phantom trial

The next set of phantom images were obtained using a superior section and head of a femoral bone set in a material with the same attenuation factor as that of body tissue. Tubing was connected to this phantom which was then strapped to the trolley

(a) (b)

Figure 8.9: Phantom of the femoral head. (a) the mask image and (b) the contrast image.

to avoid inadvertent movement between scans, and a mask image was then acquired. Subsequently, contrast medium was injected into the tubing and a contrast image obtained using the Lodox system. Figures 8.9(a) and 8.9(b) show the initial mask

(a) (b) (c)

Figure 8.10: (a) The unprocessed subtracted image. (b) The processed subtracted image. (c) An inversion of (b).

and contrast images respectively. The subtraction results can be seen in Figures 8.10(a), 8.10(b) and 8.10(c).

In the initial subtraction seen in Figure 8.10(a) the artefact shadows appear to be distributed predominantly on the left side of the bony edges in the image. This would suggest translational movement and so a fairly accurately aligned and registered subtraction would be predicted. The movement was probably due to the manual cropping of the images and/or movement occurring during the injection of the contrast medium into the tubing.

The final subtraction of the mask from the contrast images in Figures 8.10(b) and 8.10(c) yielded a good subtraction, as expected, in that most of the background information was eliminated. The images exhibit no bony obstructions, very few artefacts, and the entire contrast tube is clearly visible. The clinician, however, would not be aware of the tube orientation with respect to the femur because of the complete subtraction of its surrounding structures. An example of the significance of this can be

demonstrated in a situation where all "background" information is removed, as in this case, and the position of an obstruction relative to the greater or lesser trochanter of the femur is not distinguishable but needed. This is an important consideration when planning surgical procedures and accurate entry points need to be ascertained for minimal invasion and better healing. The inverted image in Figure 8.10(c) reveals, more clearly, a few artefacts (along the bone edges) that could not be seen in Figure 8.10(b). The result was, however, considered satisfactory.

The Matlab program took 50 seconds (Tables 8.4 and D.1) to run.

8.3.2 Patient trial

Finally, a patient trial was conducted in order to test the imaging capabilities of Lodox in a dynamic situation and to ascertain its ability to track a bolus of contrast medium flowing through an artery as opposed to the veins which was conducted by Beningfield *et al.* (1999).

The patient was a 43-year old male who had been stabbed on the medial aspect of the thigh above the knee. On admission he was reported to have had no popliteal pulse (Appendix F).

An initial mask image was taken, Figure 8.11(a). A catheter was then inserted into the femoral artery. Its position was verified by running the roadmap scan seen in Figure 8.11(b). Finally the contrast medium was injected into the vessel through the catheter. The scan was activated after the first 2 ml of contrast had entered the vessel. The exposure continued throughout the injection process – no delay period was instituted – and the total scan took 10 seconds. Only 20 ml of contrast was needed to obtain a suitable scan as opposed to the usual 50 ml required in a standard angiogram (Buonocore *et al.*, 1983; Crummy *et al.*, 1980) and the results can be seen in Figure 8.11(c).

From the initial images taken, movement between the mask and roadmap images is identifiable. The change between the roadmap image and the contrast is less pronounced but is still evident.

(a) (b) (c)

Figure 8.11: Trauma patient images. (a) The mask image taken of the left lower limb of a trauma patient using Lodox technology. (b) A roadmap image taken prior to contrast injection to ascertain whether the catheter was positioned correctly. (c) The contrast image taken after contrast medium was injected into his femoral artery. The area of interest was in the popliteal region above the knee.

Figure 8.12: Image comparison. (a) indicates a few noticeable changes due to movement. The white arrows indicate these differences and direction of rotation on the mask image. In (b) the contrast image with similar markings for comparison.

Figure 8.13: Magnified image of the problem area of the patient study. The red arrow indicates the entry wound where the clot had formed. The white arrows indicate the blocked anterior tibial and peroneal arteries.

The markings i through v in Figures 8.12(a) and 8.12(b) indicate image changes in the limb that occurred through patient movement between scans. Eversion of the foot (arrow i) between scans resulted in lateral rotation observed at the ankle joint shown by the encircled region ii and lateral rotation of the femur (arrow v) through the hinge joint of the knee (arrow iv). The rotated femur gives the appearance of a change in angle in the 2-D plane – maybe even a rotation in that plane – a good example to illustrate the theory outlined in Chapter 5 relating to the results of 3-D movement in a 2-D plane. Another observation between the mask and roadmap images include the crossing over of the tibia and fibula due to foot eversion (also seen in the encircled region marked ii) between scans. This caused the tibia and fibula to appear closer together in the image (arrow iii). These movements would all contribute to expected artefacts in the subtraction result.

Figure 8.13 provides a closer view of the knee region of the contrast image. Cropped images of Figures 8.11(a) and 8.11(c) were used for faster processing. The resultant

angiogram showed signs of clotting in the region of entry (red arrow in Figure 8.13) above the knee. As a result the degree of the vessel's patency is seen to be compromised. Because the entire limb was scanned, occlusions in the anterior tibial and peroneal arteries were also noticed since these vessels appear to end their course prematurely, just inferior to the knee. The white arrows in Figure 8.13 indicate these points. At surgery the patient had a through-and-through injury of the popliteal artery (see Figure 8.16). It was also confirmed that a portion of the clot in the popliteal artery above the knee had in fact dislodged itself and subsequently blocked the lower arteries, stemming the blood flow through them.

(a) (b)

Figure 8.14: (a) An initial unprocessed subtracted image. (b) The final subtraction image, from the Patient trial, after processing.

Figure 8.14(a) shows the initial subtracted image prior to any image correction and Figure 8.14(b) shows a corrected subtraction. The artefacts obtained in Figure 8.14(a), especially those along the bony edges, unlike the initial subtracted image of the femoral phantom in Figure 8.10(a), do not indicate linear translational motion alone. A complete subtraction of all background information after processing was not expected

(a) (b) (c)

Figure 8.15: (a)A section of the contrast image. (b)The same section but after subtraction of the mask. (c) An inversion of (b).

due to this. The artefacts however, although not entirely eliminated in Figure 8.14(b), were diminished and the visibility of the vessels containing the contrast medium was improved from that in the uncorrected subtraction of Figure 8.14(a). It should be noted, however, that the artefacts associated with the medial aspect of the fibula and lateral aspect of the tibia did slightly obscure the points of stemmed blood flow in the vessels of concern – the peroneal and anterior tibial arteries.

A comparison between the contrast image Figure 8.15(a) and the final subtracted image and its inverse (Figures 8.15(b) and 8.15(c)) can be now be made. It is noted that the vessels in the finally subtracted image of Figure 8.15(b) are enhanced and the areas of concern are more clear although not without obstructions as mentioned above. In Figure 8.15(c), the inverted version of Figure 8.15(b), the vessels are slightly more visible (the peroneal artery running down the medial aspect of the fibula) than in the

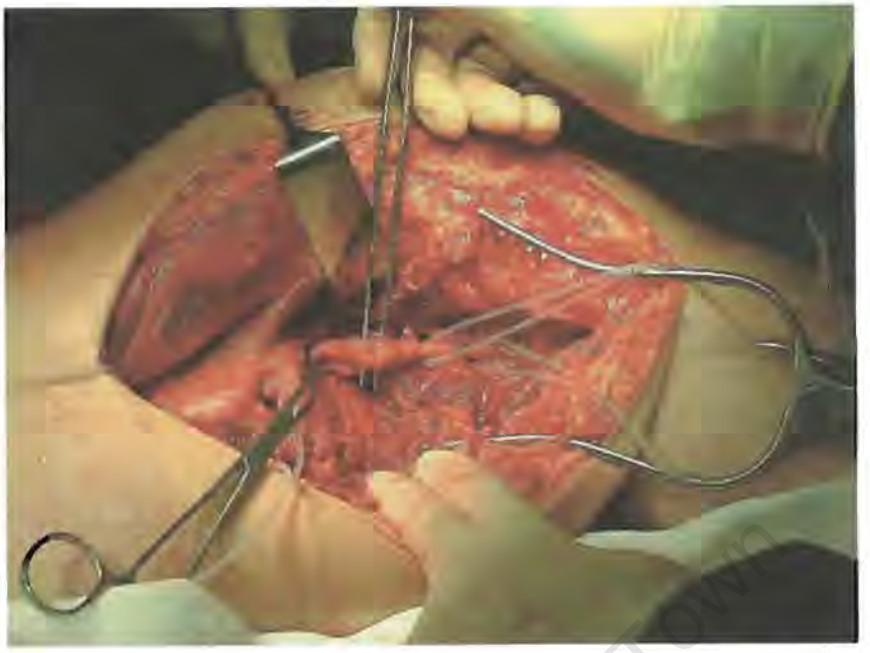

Figure 8.16: The surgical procedure: the forceps show the 'through-and-through' wound in the artery

non-inverted image and so the bony artefacts are less obtrusive and therefore slightly more acceptable.

The Matlab program took 02 minutes 41 seconds (Tables 8.4 and D.1) to run.

Finally the injured artery, seen in Figure 8.16 with the forceps positioned through the wound in the popliteal vessel, and the lower vessels of the anterior tibial and peroneal arteries were resected and reanastomosed. The patient was subsequently discharged from the hospital with a completely functional limb.

The subtraction of the images was only performed post-operatively. The images produced by Lodox were therefore imaged with sufficient clarity for surgical planning purposes without the use of DSA. The surgeons and clinicians, however, were adamant that DSA is still preferred if it were available since cases are not always as well defined and DSA images can depict finer detail. This definition was demonstrated to a small degree in the inverted Figure 8.15(c).

Table 8.4 lists the run times of each trial. This time includes all iterations until the final image is displayed. A comparison table of the run-times and results when using different border widths and automatic and manual cropping is listed in Appendix D. Table 8.4 shows that the T-tube Phantom of size 896 x 1598 was cropped to size 732

Table 8.4: Table summarising the timing of the running of each program

TEST	NO. OF CONTROL POINTS PROCESSED	TIME TAKEN
T-TUBE PHANTOM size: 896 x 1598 cropped size: 732 x 879	159	01min 08 sec
FEMORAL PHANTOM size: 2304 x 1600 cropped size: 1118 x 447	131	00 min 50 sec
PATIENT TRIAL size: 3712 x 956 cropped size: 1734 x 639	274	02 min 41 sec

x 879 and so took 01min 08 sec to run. The Femoral Phantom, size 2304 x 1600 was cropped to size 1118 x 447 and took 50 seconds to run while the in the Patient Trial the original image was cropped from size 3712 x 956 to 1734 x 639 and ran over a period of 02 min 41 sec. The number of control points selected in each case is also recorded since they affect the processing speed. These amounted to 159, 131 and 274 points respectively.

8.4 Questionnaire to clinicians familiar with Lodox

Three clinicians, all experienced users of Lodox in their own right and with some insight into angiography and DSA, were asked the same set of questions pertaining to the Lodox machine and what it can do at present regarding DSA. They were: Professor Steve Beningfield, SB, (head of Radiology at Groote Schuur Hospital); Ms Gillan Bowie, GB, chief radiographer at GSH; and Dr Andrew Nicol, AN, head of the Trauma Unit at GSH. The questions focused on their views of the current Lodox system at GSH and how they felt it compared to standard angiography systems and their DSA facilities. These questions addressed the suitability of Lodox for angiography applica-

tions, patient motion issues, radiation dose rates, timing and DSA usefulness. Their answers are summarised below.

Q: *In your estimation, how suitable is Lodox for angiography applications?*

SB Lodox is capable of imaging peripheral structures and extremities as well as carrying out arteriograms and venograms but would not be suitable for imaging visceral, head, chest and abdominal, regions which require a frame-rate type acquisition with a minimum frame rate of 3 fps. Associated with this however, one could 'cheat' by injecting the contrast from a more superior position to give more time. For venograms, table tilting is helpful in keeping the blood in a region of the veins of a longer time. It should be possible to acquire a mask image and then run an arteriogram followed by a venogram on the returning blood (containing the contrast) in the region. Often, images of similar regions for comparison are required for example in imaging a limb, left and right limb images are usually captured in order that differences between the vasculature in the two limbs is evident. Angiography gives immediate or real-time feedback. Lodox does not do this - it scans in 1-D and sums these to form a 2-D image so the progress of the bolus cannot be followed on the monitor by using frame capture.

Angiography systems are capable of scanning in specified modular regions, different anatomical regions, at one time. The benefits of this afford the clinician the opportunity to make corrections if necessary thereby salvaging the process. In Lodox this is not the case and the process is one of 'all-or-nothing'.

Angiography systems usually have a pump (or pressure injector) interfaced to the generator for timing the contrast injection with the commencement of the actual exposure.

Lodox exhibits highly acceptable image quality. Angiography requirements for imaging are of the order of 1024 grey levels while the Lodox resolution exceeds this by more than a factor of 10 at 16, 384 grey levels.

Lodox requires less parameters than regular angiography systems in the acquisition procedure but as mentioned above there is the risk of the 'once-off' scan.

GB Angiography systems offer real-time imaging, Lodox does not, so the clinician cannot watch the contrast dissipation in real-time. Lodox produces a static image since no frames are acquired at any stage. Contrast in the venous return of the limbs can't be seen. This is only possible in the head and you then need real-time fluoroscopy.

Images are too course - cannot see small vessel branches in the region of interest (ROI) only the large ones. In Lodox can't give a continual supply of contrast to wash the region which is a problem if the blood flow rate is too fast.

Image transfer from digital to film is not satisfactory for fine work. It is however suitable for gross work but there is a significant loss of information of arterioles etc in the transfer.

C-arm movement limitations mean it is often difficult to swing from an AP to a lateral scan especially with regard to a trauma patient where movement is often not an option. The C-arm is only capable of movement in 2 planes and so no projections are possible however, angling of the tube in a projection study is still limited in an angiography system. C-arms are not generally as flexible as a moveable tube on a conventional x-ray system.

Lodox can't do spot films nor does it scan small images repeatedly. It does not give the option of displaying a series of images on one film for comparative purposes but this would also be more cost effective.

AN Definitely. The benefits of running a full limb scan in our study, helped us assess the lower vessels that were occluded with clots that otherwise would have been missed because the upper part of the lower limb would probably only have been scanned. There were no issues associated with timing C-arm velocity and patient movement. The image quality was completely satisfactory and the film produced could pick up where the tibial and peroneal artery patency was compromised. There is also no need for a pressure injector. Hand injected contrast is sufficient for the purposes of peripheral imaging in this case.

Q: *What is your experience pertaining to patient motion issues as relates to Trauma?*

SB Trauma patients can be particularly problematic (more problematic than the general patient) in terms of movement, if not unconscious, they may experience involuntary limb twitches and thrashing movements.

GB Trauma patients are usually seriously injured so movement is not generally a huge problem. If they thrash about the bands attached to the trolley can be used.

AN Movement of patients in imaging using Lodox has not proved to be problematic however, the patients scanned thus far have been selected and so those with movement issues have not been scanned.

Q: *Are radiation dose rates a concern to you?*

SB Definitely. Have experienced skin burns in procedures involving multiple projections in angiographic procedures so awareness is necessary. Philips and Toshiba offer grid control which lowers exposure rates. Image quality is however a fundamental priority that no one is prepared to compromise on.

GB Not at all especially when image quality is jeopardised. There is awareness however when dealing with pregnant women and paediatrics, and 'trade-offs' often result since dose rates that are too low produce mottley, undesirable images.

AN This is a concern since many staff perform multiple x-ray scans per shift and often do not exit the resuscitation area throughout this time due to the demand. These are susceptible to excess exposure and so a reduction of exposure is definitely attractive.

Q: *What is the maximum time that can be taken between the injection of the contrast medium into the vessels and the initiation of the exposure and thus the scan?*

SB There is an interval of about 14 seconds after the contrast is injected into the vessels in which the scan can take place. In the first few seconds the region is not sufficiently saturated with contrast since it is still washing through into the region. The best time to start the scan is in the 8 to 14 second interval in normal angiography.

One could conduct a trial run involving an injection of contrast into a vessel in the pelvic or abdominal region. The time it takes the bolus to reach the knee would be recorded and then used to determine when to start the scan after contrast injection by calculating the blood flow rate.

Typically 100 ml of contrast at 8 ml/sec is administered resulting in a total of 14 sec scan.

GB This is dependent on too many factors to say, blood flow rate, patient age, degree of trauma etc. One minute is too long.

AN The exposure was activated after first 2 ml of contrast was injected into the femoral artery and continued throughout the injection process. No delay was therefore employed in the study and the results are completely satisfactory.

Q: *How long would you be prepared to wait for an image to be displayed on a monitor?*

SB About 10 seconds. One minute is too long.

GB Almost instantaneous, Lodox is too slow at present.

AN It normally takes a radiographer 5 - 10 minutes to develop film from normal scans so one minute would be satisfactory.

Q: *If DSA was available for use in Trauma would you use it and/or would you find it helpful?*

SB Definitely. Windowing doesn't compare to DSA in terms of clarity. There is a significant improvement when using DSA in vessel imaging.

GB Most after hours work in trauma involves the use of angiograms so it would definitely prove useful.

AN Definitely since the clarity is better and in the case of the images taken in the patient study, the occlusion of the anterior tibial and peroneal arteries would have been clearer not being obscured by the tibia.

Chapter 9

Discussion

9.1 Lodox and the needs of trauma

The Lodox-MP System is a digital X-ray imaging system developed specifically for emergency medical centres (De Beers, 2001). Some of its major attributes appear in the 'needs list' mentioned in Chapter 2 and include:

(1) operation in a variety of orientations;
(2) low dose;
(3) rapid image acquisition;
(4) simple operation;
(5) almost real-time display of
(6) high contrast images that are
(7) DICOM 3.0 compatible.

From Chapter 8 it is noted that the C-arm of the Lodox system is capable of rotating from zero through 90 degrees but may only scan in one direction – along the length of the trolley. This allows for oblique and lateral scans according to Schindehutte *et al.* (1998) and the Appendix F case report. These orientations are limited in that the arm cannot scan in multiple directions but should be suitable for most imaging purposes although this may complicate the acquisition of certain lateral scans in terms of patient positioning.

Although most radiographers are not concerned about dose rates unless the image quality is compromised (Section 8.4), the low dose output by the Lodox system is favoured amongst those concerned and provides a safer working environment for the resuscitation room staff. Professor Beningfield and Dr Nicol, in response to the questionnaire set out in Section 8.4, both expressed a preference in systems that could produce good images with lower x-ray dosage.

These dose rates were compared with those of the Philips Allura system which gave a mean entrance dose to the patient of 1.2 μGy/s, and a mean dose to the staff of 0.325 mG/hr. Unfortunately, as mentioned before, the Toshiba values were not available. The Lodox dose ranges were 40 - 338 μGy and 0.7 - 2 μGy respectively – well below the FDA approved patient entrance doses of 10 R/min (100 mGy/min or 1.66 mGy/s – 23.24 mGy in 14 seconds)) and as documented in Section 4.1.4, a user dose of 20 mSv per annum. It should be noted however that the Philips rates stated above relate to a fluoroscopic system and so should be very low in comparison to the Lodox system which is not designed to function as such. Unlike the Philips measurements, Lodox does not have measurement rates in per second units because it does not run multiple scans per second but rather performs one complete scan to produce a single image. This therefore indicates one exposure per scan. Because of the differences in these systems, drawing exposure comparisons is not a straight forward task and the FDA criteria are used more as a guide than the other system specifications.

In terms of time, Lodox can acquire a full body scan in under 14 seconds (Section 8.1.2) and generally takes less than 15 seconds to display the scanned image on the monitor for inspection (Lodox Systems (Pty) Ltd, 2003). According to the responses in Section 8.4, this is acceptable as the images no longer need to be developed in order to be read.

Lodox offers a simple interface and makes use of fewer parameters than regular angiography systems (Section 8.4), making it easy to learn and use. Although this is a subjective statement it appears that staff learning to use the Lodox system in the Milpark Hospital in Johannesburg and GSH in Cape Town have not found it excessively difficult. According to Virginia Sanders, the Lodox inhouse radiographer, who is responsible for the training of new Lodox users, it is very easy to learn if there is prior basic computer literacy. Otherwise basic computer skills need to be learnt before the

Lodox system can be grasped. This however would need to be confirmed by formal testing.

In terms of real-time display, the time taken for Lodox to display its images after acquisition varies depending on the image size, but as mentioned above will be under 15 seconds for a full body scan. From Section 8.1.2 it is shown that Lodox provides spatial resolution up to 8.3 lp/mm depending on the scanning mode and the binning used in the image acquisition process. This was compared to the commercial systems investigated which give maximum spatial resolution values of 6.2 lp/mm and 5.8 lp/mm for the Philips Allura and Toshiba systems respectively. Lodox resolution is therefore acceptable in this regard especially where peripheral vessel imaging is concerned. Unfortunately, the MTF values of the various systems could not be obtained and so the image quality could not be compared for this parameter. The line-pairs-per-millimetre rating does however provide a basic means for comparison.

All the systems utilise CCD technology and are DICOM 3.0 compatible. DICOM compatibility is a necessity in that it allows for inter-departmental and even inter-hospital communication and information exchange.

According to the emergency room angiogram (ERA) reports summarised in Chapter 2 and Ms Bowie's statements made in Section 8.4, angiography is a tool that is readily used in trauma. Essentially, by incorporating DSA into the Lodox system, one would be providing a form of ERA to the trauma unit that uses the Lodox system. Advantages of Lodox being able to perform an ERA lie in its ability to image an entire limb in one scan, magnify areas for investigation and use decreased amounts of contrast medium in order to obtain a sufficiently clear contrast image – 20 ml as opposed to 50 ml in standard angiography images (see Section 8.3.2 and Appendix F). This latter statement is inconclusive due to insufficient trials being conducted. MacFarlane *et al.* (1989) reported similar findings, however, and a decrease in the required amounts of contrast medium used in this study is worth noting. The degree of consistency in future trials will need to be observed.

Lodox does not offer a fluoroscopic facility as do the conventional DSA systems. In conventional DSA, fluoroscopy is used to enable the clinician to monitor the position of a catheter that is being inserted into a vessel. In other words, low dose x-rays are used to obtain roadmap images for the clinician. Peripheral vessels are more

readily accessible than deeper vessels and so require less monitoring when inserting a catheter into them. One or two roadmap images (frames) could be sufficient to ascertain whether the catheter has been successfully inserted into the required vessel. Lodox, With it low dosage x-rays, is capable of performing the latter which was successfully demonstrated in the patient trial reported in Chapter 8. The lack of fluoroscopy should not therefore be a major limitation to the Lodox system as long as peripheral vessel imaging remains its focus.

9.2 Lodox and DSA system components and imaging characteristics

Lodox compares favourably with the other systems – the Integris Allura and the Toshiba Infinix VC – used for comparative purposes in this dissertation. In this section, the following topics will be discussed: the generator, analogue-to-digital converter and it's sampling frequency, the image preprocessor, digital viewing station, storage, temporal resolution, noise and blood flow velocities

9.2.1 The Generator

The generator supplies electrical power to the x-ray tube as well as feedback to ensure effective dose regulation and safe operation.

From the information in Table 8.2 it was noted that the Lodox generator uses a substantially lower power output of 43 kW than does the Philips Allura and the Toshiba Infinix VC at 100 kW. This is acceptable in that the Lodox system is specifically designed to produce low dosage x-rays and runs at a considerably lower sampling frequency of 2.75 MHz as opposed to the 40 MHz (fluoroscopic sampling rate) sampling frequency of the Philips but is more comparable with the 4.4 MHz of the Toshiba system. The generator output therefore, does not need to be as high as in a regular fluorocopic or standard x-ray system. The Lodox x-ray tube is a standard CT tube with rectangular focal spots of size 0.7mm x 0.8mm and 1.2 mm x 1.4 mm as opposed to the square spots in both the Philips system (0.3 mm and 1.0 mm) and the

Toshiba model (three focal spots at 0.3 mm - 1.3 mm). Under normal x-ray image capture the difference between the small focal spots of the different systems would be significant with the small focal spot of Lodox producing less sharper images than that of the other systems. However, with the technology used in the process of image development in Lodox (TDI – Appendix B), the image contrast is not compromised in any way.

The kVs and mAs used in specific image acquisition modes are slightly higher in Lodox than in other systems (Lodox: 125 kV (max), 300 mA (max); Philips Allura and the Toshiba Infinix: 80 to 150 kV, 630 to 1,250 mA). This is due to the slightly larger focal spots and the requirements of the scintillator which is not as sensitive as the intensifiers found in the Philips and Toshiba machines to x-ray photons. The scintillator is suitable for its purpose in Lodox and is not as bulky as an image intensifier would be. Due to the electronics the output image is still of a very high quality, even though the dose rates are low (as discussed above and in Chapter 4). An acceptable resolution at 14 bits in comparison to the 8 to 10 bits of the other systems exists (Chapter 4). Lodox is therefore able to display 16,384 grey levels – a difference of 4 bits but actually offers 15,360 grey levels of extra information compared to the other systems.

9.2.2 Analogue-to-digital converter (ADC) and its sampling frequency

An ADC converts the analogue signal obtained from the CCDs and into digital form for processing and storage. The accuracy of its conversion and its spatial resolution output are dependent on its bit depth and its sampling frequency.

The differences in the ADCs of the compared systems can be seen in Table 8.2 where the Philips and Toshiba systems provide bit depths of 10 bits and a sampling frequency of 40 MHz and 4.4 MHz respectively while the Lodox system offers a bit depth of 14 bits and a sampling frequency of 2.75 MHz. In terms of the Lodox technology this sampling frequency was adequate to ensure the least amount of noise introduced in the conversion process. In the line clock a pulse is triggered every 360 to 420 μs activating the CCDs to absorb x-ray information. In conventional systems the CCD information is clocked out as quickly as possible and is referred to as frame

transfer. It is therefore possible for conventional systems to run a sampling frequency of 40 MHz. Lodox essentially integrates lines of information obtained at a certain rate, set by the sampling frequency, to form a *single* image that can be compared to a time lapse photograph. Conventional systems, however, scan multiple frames at a certain sampling frequency producing, as Rutherford *et al.* (1995) expressed, cineradiography or rapid sequence filming. Therefore Lodox does not need as high a sampling frequency rate, because this would only introduce noise.

9.2.3 The image processor

The image processor processes the raw images that are passed to it from the ADC. It is the digital viewing station (DVS) that offers quick image manipulation capabilities such as window level adjustments, edge enhancement, pixel shifting, etc. (see Table 8.2).

The Lodox system does not provide as broad a spectrum of processing capabilities as the Philips Allura or the Toshiba Infinix systems. These however could be incorporated provided they are in compliance with the Lodox capabilities. What it does offer (see Table 8.2) is sufficient for basic DSA viewing such as zoom functions, unsharp masking, a palette function and an invert function. It does not allow for multiple images to be viewed simultaneously on the monitor nor does it offer the clinician the option of printing multiple images onto one film for comparative purposes. This appears to be one of its major draw-backs as far as the radiographers are concerned (*cf.* Ms Bowie's comments in Section 8.4).

9.2.4 The digital viewing station (DVS)

The image quality on the DVS is definitely acceptable and of a high standard, although it appears that, depending on the level of detail required, a hard-copy does not exhibit the same detail. This implies some loss of information. Ms G Bowie found this to be the case although Dr Nicol found the film copies satisfactory for the purposes of the patient study (Section 8.4). Lodox offers all the basic necessary viewing capabilities needed by clinicians for improved analysis of the displayed images (Section 8.2).

9.2.5 Storage

Lodox provides the least storage space of 20 GB when compared to Philips Allura and Toshiba Infinix. The Philips Allura and the Toshiba allow 36 GB and 32 GB respectively. It should be noted however that the latter systems will be storing a series of contrast image frames (minimum number of 28 frames if the image capture is taken over 14 seconds at a rate of 2 fps) in conjunction with the mask image for one DSA acquisition set. Lodox uses a maximum of three images: the mask, roadmap (if needed) and one contrast image per acquisition set. Less storage space should not prove problematic and extra space could quite easily be added if required (Sections 8.1.1 and 8.1.2).

9.2.6 Temporal Resolution

Because the original focus of Lodox was to perform a full body scan for multiple traurna screening (Section 8.1.2), its scanning technology differs from the standard angiography systems. In Lodox the scan takes place as the C-arrn traverses the trolley, building an image line by line. This is not so with regular scanning where an area is imaged repeatedly to produce multiple frames (see Section 9.2.2 above). This impacts on the number of images that can be scanned in a specific time frame and so, with regard to the parameter of frarne rate or temporal resolution, there is no comparison between Lodox and the standard angiography systems.

The advantage of having multiple frames lies in being able to find a "best fit" contrast image. This will decrease the processing needed in order to improve image alignment between the mask and contrast images. With Lodox, this "choice" is not available and so the two acquired images must be "forced" to align. This is a definite drawback but one that is solvable with the use of software. An advantage lies in the decreased amount of storage space needed to store a set of patient data (this is emphasised by the values stated in Table 8.2 where Lodox uses a minimum of 20 GB while the Philips and Toshiba systems use a maximum of 36GB and a minimum of 32 GB of storage space respectively).

9.2.7 Noise

Noise is a signal carrying no useful information as defined in Section 4.1.5. The effects of noise on an image is expressed as the signal-to-noise ratio (SNR). In digital systems an acceptable SNR is in the order of 1000:1 or 30 dB as stated in Section 4.1.5. Lodox has a minimum SNR of 45 dB (well above the accepted SNR) while the Philips Allura and Toshiba have SNRs of 80 dB and 60 dB respectively which are substantially higher but required with higher sampling frequencies. Lodox does not require as high a SNR as in the Philips and Toshiba systems where DSA images are captured at a high frame rate during which additive noise is quite substantial.

9.2.8 Blood flow velocity

The blood flow rate was required to determine whether the Lodox C-arm is capable of moving at speeds that would allow its detectors to track a bolus of contrast medium through the vessel(s) into which it was injected. This would indicate if Lodox was capable of performing an arterial DSA operation in addition to venous angiography which was carried out by Beningfield *et al.* (1999) as mentioned in Chapter 2.

The data found on blood flow velocity showed the velocity in the arteries of the lower peripheral extremities to be 120 mm/s with an increase in velocity as the vessels are located deeper and more proximal to the heart. Because the C-arm is able to move at a maximum velocity of 140 mm/s, it was expected that the bolus chasing through the femoral artery was indeed possible. This was confirmed in the patient trial reported in Chapter 8 where Dr Nicol found that the C-arm of Lodox moved at a suitable velocity, if not slightly faster, than required for the purposes of the contrast scan. It took the clinicians 10 seconds to acquire each scan from which they were suitably informed on the injury details for successful surgery.

From Section 8.2 and Section 8.4 it can be determined that the Lodox system would be incapable of visceral imaging where, in the renal arteries for example, the blood reaches velocities of 400 mm/s (Table 8.2). In order to image these regions, Lodox would need to be capable of scanning small anatomical regions repeatedly, thereby creating a multiple frame exposure which is not possible with its current technology. According to Dr Nicol (Section 8.4) and the results from the patient trial in Chapter

8, this is not a concern since for the purposes of trauma, peripheral imaging is what is most often required. Also, the ability to image an entire region such as a limb in a single scan is preferred for comparative overviews. In the patient trial of Chapter 8, the lower vessel occlusions would not have been so readily determined had the entire limb not been imaged. Usually, acquiring an image covering an area of this size would require two standard angiograms which would also take at least double the time and involve moving the patient.

9.3 Registration approach

For the purposes of this thesis feature (intrinsic) based control point selection, as argued by Buzug *et al.* (1998) and Meijering (2000, 2001), was utilised as opposed to the more conventional regular grid process outlined in Section 6.2. Meijering (2001) described it as a process whereby the control points are selected at positions where the probability of introducing artefacts is highest and where large contrast variations exist between neighbourhoods resulting in better displacement estimates.

A set of sample points reduces the computational time required in running the registration and subtraction program as mentioned in chapter 6. The other alternative would be to calculate the displacements of each and every pixel in the image. In the case of Lodox images, that could pertain to image sizes of 22 MB or an image of 2307 x 6016 pixels when scanning with normal resolution – 5 x 5 binning. Raw images could be as large as twenty-five times that, depending on the binning selected prior to image acquisition. This would have a massive impact on the processing time required to process these images. Even when using the template matching technique and a selection of control points, the time taken to process images of this magnitude would far exceed the accepted time allowances.

Unlike the regular grid process, this method of feature based control point selection results in an irregular distribution of displacement vectors. Meijering (2001) pointed out two approaches to finding the overall displacement vector field but they are dependent on the reliability of the local displacement vector field found. If sufficiently reliable, linear interpolation was the cheapest computational approach involving triangulation of the set of control points to find a suitable transformation. More complex

cases may require thin-plate splines which would be more computationally expensive but would produce more accurate approximations. The alternative approach would be regularisation where the final control point vectors are dependent on their neighbouring control points.

9.3.1 Similarity measures

Not all similarity measures would prove optimal for the purposes of DSA. The reasons as to why each may or may not be suitable are discussed in the relevant sections of Chapter 6. All the measures described were, on average, insensitive to grey level offsets. The phase correlation measure was less sensitive to noise than the cross correlation measure. Of the difference based measures the DSC measure was insensitive to an influx of contrast. This was unlike the cross correlation measure that was sensitive to an introduction of edges which are introduced with an injection of contrast into the vessels of interest. Mutual information was considered best for multimodal images only.

Meijering (2000) pointed out that in contrast to all the similarity measures that have been used in registration and subtraction of images, histogram-based measures consider relative frequencies of difference values. They are thus insensitive to mean grey-level offsets and local dissimilarities caused by contrasted vessels. These measures therefore do not require exclusion templates as used by Cox (2000) and are computationally inexpensive, not requiring tuning of parameters as in the DSC measure. They yield very smooth match surfaces which allow for efficient optimisation. Of the functions outlined the EHD was shown to be the most adequate for registration in DSA because it involves only one calculation – squaring. It was therefore considered computationally cheap while yielding accurate results and therefore best suited for use in DSA.

9.4 Program and results

The program developed in Chapter 7 was used to show proof of concept and its performance was tested in the experimental trials reported in Chapter 8. The ability

of Lodox to track the flow of contrast in a peripheral artery was also tested. An unexpected result was the relatively small amount of contrast medium required for acceptable enhancement of vessels.

The automatic cropping of some images proved to be unsatisfactory. Images of results obtained when using the automatic crop function may be found in Appendix D. Section D.2 gives results pertaining to the comparison test of the two border widths when utilising manual cropping techniques. As shown in Appendix D.1, the T-tube images with a broader border provided better results. The initial automatic crop was satisfactory even though it introduced a translational shift. This shift was obvious when observing the lower-most "coin" structure in Figures D.1(c) and D.1(d). In observing the difference images in Figure D.3, the upper-right section in Figures D.3(a) and D.3(b) shows an almost eliminated coin and plug in the tubing while most of the structures in the images below, which are surrounded by the smaller border (Figures D.3(c) and D.3(d)) still contain well defined boundaries.

In the case of the femoral phantom the automatic cropping function proved unsatisfactory in isolating the bony structure. The image was therefore much larger than necessary which resulted in unnecessary processing and longer run-times. In this scenario, the subtracted images with the smaller border (Figures D.5(g) and D.5(h)) yielded a slightly better result in that the lateral aspect of the femoral shaft is less apparent than in the subtracted figure with the broader border (Figures D.5(e) and D.5(f)). The automatic cropping in the patient trial images was totally unacceptable as it did not capture any part of the image that was in fact of interest – the popliteal section – and so further processing was not warranted. This is a testimony to the program's lack of robustness across different images when using automatic cropping.

Section D.2 depicts the results obtained when using the different border widths around manually selected regions for processing. These results were better overall than those of Section D.1 where the images obtained with the smaller border yielded fewer artefacts than their broader-border counterparts. This may be debatable in the patient trial subtraction results in Figure D.13 where the opposite seems to be apparent. In general, though, the contrast filled vessels are viewed with more clarity in the lesser border images as seen in Figures D.9(c) and D.11(g) of the T-tube and femoral trial results respectively. The smaller border and manual cropping was therefore preferred.

The manual cropping produced better results but, due to human operator inaccuracies, introduced a certain amount of pixel shifting. The figures in Appendix C show the program's ability to correct for gross translational shifts in four different directions between two images. The results of the femoral phantom trial in Chapter 8 (Figure 8.10(b)) also demonstrated the program's ability to address gross translational movement correction with satisfactory results (satisfactory in terms of the elimination of information common to the images being subtracted). These results allow an assumption to be made: that the artefacts introduced in the subtracted images of the T-tube (Figure 8.8(a)) and patient trials (Figure 8.14(b)) were due to other forms of motion (such as 3-D rotation) that were not as accurately corrected for as may be necessary.

9.4.1 Phantom trials

The main focus of the phantom trials was primarily to test for gross changes due to linear movement between scans. Other smaller changes due to the warping of the board in the T-tube trial were also added for more detailed testing before implementing the patient trial images. From Chapter 5 we are reminded that gross translation in this dissertation refers to a translation or rotation that exceeds the K x L pixel window width (search area) used in processing.

T-tube phantom trial

In the T-tube trial linear shifting, rotational and 3-dimensional movement were introduced by the manual cropping of the image and by the warping of the board. This affected the accuracy of the registration and therefore the degree of subtraction and the resultant development of artefacts. These artefacts are evident in the pre-processed subtracted image of Figure 8.7. They were largely eliminated in the final subtracted image shown in Figure 8.8(a) after both gross and finer movement had been accounted for in the processing procedure. The artefacts not entirely eliminated revealed more clearly the different axes of rotation (indicated by the red and black lines drawn in Figure 8.8(b)) that would need to be considered. In this case the artefacts did not obscure any information regarding the tube but they did illus-

trate the effects of movement in the third dimension on an image in the 2-D plane. The outcome of this trial was fairly satisfactory. The gross movement was definitely accounted for as only the smaller local changes caused artefacts as a result of the warping of the board. These changes could be looked at in more detail when developing this program further. Further outcomes of adjusting for pure translational movement can be seen in Appendix C where the shifted images are corrected and subtraction of the common information is complete. The time taken to process this information was just satisfactory at 01 minute and 08 seconds. This however could be considerably decreased.

Femoral phantom trial

Correction of the simple translational movement predicted by the shadows in the initially subtracted image produced an expected result – an accurate subtracted image. The movement was probably due to the manual cropping of the images and/or movement occurring during the injection of the contrast medium into the tubing although this was kept to a minimum due to the strapping. This illustrates one of the means of patient related solutions of immobilisation described in Chapter 5.

The registration and subtraction of the images acquired of the femoral phantom were satisfactory as seen in Figures 8.10(b) and 8.10(c) in that most of the background information was eliminated. The images exhibit no bony obstructions, very few artefacts, and the entire contrast tube is clearly visible. This trial did indicate the importance of providing the clinician with a means to identify the vessel's orientation with regards to its surrounding anatomical structures. As mentioned in Chapter 8, this is an important consideration when planning surgical procedures and accurate entry points need to be established. In the subtracted image almost all artefacts were eliminated as well as the background information common to both images. The contrast filled tubing was all that remained.

There needs, therefore, to be a function that will enable the clinician to vary the degree of background information viewable behind the contrasted vessels in the subtracted image. A slider would be appropriate in this case. The adequate subtraction also indicated that the grey level differences between the mask and the contrast im-

ages did not appear to be too much of a concern, and that the algorithm was fairly insensitive to the variations in grey level difference values between the images.

It took a satisfactory 50 seconds to run this trial about 18 seconds less than its predecessor trial – the T-tube trial. This was due to the difference in the number of control points selected and is discussed in Section 9.5.

9.4.2 Patient trial

The patient trial was conducted in order to test the imaging capabilities of Lodox in a dynamic situation and also ascertain whether it is capable of tracking a bolus of contrast medium flowing through a peripheral artery.

Cropped images of the full figures (Figures 8.11(a) and 8.11(c)) were used for faster processing. Because the scan imaged the entire limb, occlusions in the anterior tibial and peroneal arteries were observed. This might have not been the case otherwise.

The contrast bolus could be tracked throughout the scan, producing a satisfactory contrast image that was used to ascertain the patient's vessel integrity and patency. The amount of contrast medium used was considerably less at 20 ml compared to the expected amount of 50 ml usually used in an angiography scan. This was an unexpected result and had not been considered before the trial but is a definite benefit in terms of cost and speed of acquisition. It does need to be further investigated as mentioned in the patient trial section of Chapter 8. Similar findings by MacFarlane *et al.* (1989) regarding this feature, provide more confidence in terms of the expected outcomes in future trials.

A roadmap image was able to be performed to monitor the catheter's path prior to contrast injection. This could be done at little risk to the clinician due to the low radiation doses used by Lodox.

Normally a delay is required between the contrast injection and the activation of the scan. The bolus needs to be injected at a fixed rate and hence the use of automatic injectors that are synchronised to the imaging generators (Section 3.1.2). With Lodox, an automatic injector appears to be superfluous and the scan may be activated immediately. In this trial the scan was activated after 2ml of contrast had been admin-

istered. This would necessitate two clinicians in order to run the operation but would decrease the time needed to perform a DSA scan.

The 3-D movement between the mask and roadmap images (as outlined in Chapter 5) was evident in the various changes that resulted in the image due to the patient everting his foot between scans. This was depicted in the change in appearance of the femoral shaft angle and the crossing over of the tibia and fibula near the ankle joint which caused these bones to appear closer together in the shafts inferior to the knee (see Figure 8.12(a)). This would definitely affect the alignment and therefore the registration of the images and, as expected, the subtraction was not as accurate as desired. The artefacts introduced could not be associated with rotation around one set of axes nor with one imaging plane. Despite this, the artefacts in the final subtracted image (Figure 8.14(b)) were diminished and the visibility of the vessels containing the contrast medium was improved from that in the uncorrected subtraction of Figure 8.14(a).

The inverted subtraction image (Figures 8.15(c)) proved the most favourable in identification of the blocked vessels and entry wound. In the non-inverted image (Figure 8.15(b)), the artefacts caused by the bony edges obscured the terminal points of the anterior tibial and peroneal arteries. In both the inverted and non-inverted subtraction images, however, the entry wound was enhanced and therefore could be seen with more clarity than in the contrast image. This therefore was a satisfactory result despite the unwanted artefacts introduced.

The actual subtraction was carried out post-operatively and so it is noted that the DSA images were not essential to the procedure being performed successfully. The clinicians were questioned in this regard and their responses can be read in the questionnaire in Chapter 8. Each one stressed the need for DSA images as most cases would not be more complicated than this one and the subtracted images undoubtedly offer better clarity which they prefer.

The lateral displacement of the leg was used as an example in Chapter 5 to illustrate the effects that artefacts, introduced due to misregistration at bone edges on subtraction, might have in falsely resembling vessels. In this trial the artefacts simply obscured the vessel's termination but the lack of clarity was observed. In immobilis-

ing the patient's leg (Section 5), by strapping it to the trolley for example, foot eversion could have been avoided to some degree at least.

As regards the artefacts produced in these trials, the following were noted as areas for future improvement:

- Better weighting of control points and use of the correct similarity measure was necessary. The difference of histogram measure set out in Chapter 6 would contribute to more accurate displacement vector formation (as mentioned before, this was computationally very expensive and so not implemented directly in this dissertation).
- Spurious displacement vectors also need to be corrected for as outlined in Chapter 6. This will allow for a better interpolation of the intermediate pixel values since the formation of the Delaunay triangulation is dependent on these vectors. The local transformations developed will consequently provide more accurate localised warping. This in turn will result in better registration, producing subtraction images containing fewer artefacts, distortions and detail obstructions.

The final subtracted image took 2 minutes 41 seconds to be displayed (Tables 8.4 and D.1). This is far from ideal and illustrates the need for a more efficient program and specific hardware. This trial did however demonstrate the capability of Lodox to perform DSA with relevant software and hardware additions.

9.5 Speed and efficiency of the program

From Table 8.4 it is noted that the difference in the timing between each trial was related to the number of control points selected for processing (this is mentioned in Section 6.2). These in turn were dependent on the detail (edges) present in each image rather than the image size itself. This can be seen when comparing the T-tube outcome with that of the femoral phantom results. Here, the femoral phantom produced a larger cropped image of size 1118 x 447 while the T-tube gave a cropped image size of 732 x 879 but the number of control points in the femoral phantom trial

was 131 compared with 159 in the T-tube trial. The time difference was 18 seconds (Femoral trial: 50 seconds, T-tube trial: 1 minute 08 seconds). It should be noted, though, as mentioned in Chapter 6, that the more control points processed, the more accurate the results will be and so a compromise must be made.

The average time taken to run the trials was calculated at 1 minute 33 seconds. As an operational function, this would be considered unacceptable since the maximum tolerable waiting time is one minute according to the response in Section 8.4. In order to reduce the time taken to acquire the final subtracted images and to display them on the monitor for the purposes of diagnosis and surgical planning, dedicated hardware is needed. Meijering (2001) managed to decrease the processing time in this way. Using a more suitable programming language such as Visual C++ would also decrease the processing time since Matlab is only an interpreter of C. This decrease in processing time is critical if this facility is to be used by clinicians. Unless the subtraction and display can take place at the same speed or faster than the manual application on the standard DSA systems, Lodox would not be suitable for DSA applications in the trauma environment where time is critical.

From the questionnaire set out in Chapter 8 it can be deduced that DSA, although not critical in observing vessel obstructions when viewing Lodox generated images, is preferred amongst clinicians since they feel that in more complicated situations it allows for more clarity of contrast-filled spaces. In addition, as pointed out by Ms Bowie, most after hours work in trauma involves the use of angiograms. All clinicians agreed that Lodox was at least reasonably suitable in its present state for angiography applications and as Dr Nicol pointed out, the occlusions in the tibial and peroneal arteries would not have been so readily observed had Lodox not scanned the entire limb. Regular angiography systems do not allow for imaging regions of this size, requiring two images to be scanned in order to observe the amount of information displayed in a single Lodox image.

Chapter 10

Summary

The purpose of this dissertation was to investigate the possible incorporation of a DSA (Digital Subtraction Angiography) facility into the current Lodox system.

One of the initial requirements was to ascertain whether there was a need for DSA in the trauma unit and whether it would prove to be a helpful aid to the clinicians working there. This was indeed the case and the clinicians questioned regarding this were all emphatic about its appropriateness.

Secondly, a component audit was conducted, comparing the existing Lodox system and two standard, commercially available systems that currently perform DSA. The systems used in this regard were the Philips Integris Allura and the Toshiba Infinix VC systems. The comparisons showed that Lodox did indeed have the relevant components and was capable of performing standard, though basic, angiography in its current form. One of the criteria for ascertaining this was whether the C-arm could scan at sufficient speed to accommodate arterial blood flow. This was also deemed adequate though only for peripheral imaging.

Subsequently, a program was developed, using Matlab, to perform a basic subtraction routine so that studies could be conducted in order to confirm the aforementioned theoretical findings. In so doing, a literature search into the issues associated with patient motion and image registration was conducted and the algorithms employed were investigated and implemented. This was successful, with the exception of the

program's processing time. It was not, however, the intention of this dissertation to develop a fully functional DSA facility so this was not a concern.

Lodox is already capable of acquiring ERA (Emergency Room Angiogram) images as proved in the case report of Appendix F. Consequently, DSA is not the only means of vessel imaging in Lodox. It is however a preferred requirement amongst clinicians who feel that in more complicated situations it allows for better clarity of contrast filled spaces. All clinicians agreed that Lodox was at least reasonably suitable for angiography applications.

From the questionnaire, it is noted that x-ray dosage is not a primary concern and is often neglected, consideration among clinicians particularly when a trade-off between it and image quality is necessary. Professor Steve Beningfield and Dr Andrew Nicol, however, both expressed a preference in systems that could produce good images with lower x-ray dosage.

It is therefore not essential for Lodox to have a DSA facility in order for clinicians to obtain adequate information for the purposes of surgical planning. All clinicians, however, expressed a keen desire for a facility to be included if possible since it does offer improved vessel visibility.

Since it can be concluded that the incorporation of a DSA facility into the Lodox system is indeed feasible, certain recommendations follow as a result of this study.

These recommendations are to implement a quick, almost real-time subtraction algorithm to the system's software programs since the one developed for the purposes of this study is too computationally expensive (the reasons are stated in Chapter 8). This would involve the addition of dedicated hardware. A slider operation that will allow clinicians to vary the degree of background information viewable on the subtracted image should be included into the program. Finally, a program that will allow the user to view multiple images on the digital viewing station (DVS) at any one time, and enable the printing of multiple images onto one film needs to be investigated and implemented. This has been a request from numerous clinicians using the system as it will allow them to compare different views of the image structure at once.

Future research into this topic could address the possibility of including another tube into the C-arm technology (and therefore another detector box) so that one scan will

produce two images for subtraction (the mask and the contrast) - one that superseded and another that succeeded the bolus. This will solve many issues related to patient motion and acquisition time. More patient trials need to be conducted in order to thoroughly test the system and its new capability. Finally, although the image quality on the DVS is excellent, some clinicians have found the hard-copies too coarse when fine detail is required. This needs to be investigated in more detail and corrected if necessary.

Appendix A

Component Details

A.1 X-ray tube

For any x-ray system the target material used in the x-ray tube is an important consideration because photon production in the x-ray tube is derived from interactions of the electrons with the anode. Common materials used for the target and filters include: molybdenum, rhodium and tungsten. Molybdenum produces a narrow beam spectrum while others generate a larger proportion of higher energy photons. The quality of the x-ray beam s a description of the penetrating power of the beam.

"X-rays are produced when rapidly moving electrons are stopped." Tungsten is often used as a target material because it has a high atomic number resulting in more efficient x-ray production. The number of electrons (i.e. the current between the anode and cathode) produced is controlled by varying the heating current through a tungsten filament which is surrounded be a cylindrical focussing cup at the same potential as the filament. The tube is highly evacuated to ensure that the life span of the filament is not comprornised by the collisions of particles in the tube with it. The electrons are accelerated towards the tungsten target embedded in the copper anode. (Brown *et al.*, 1999).

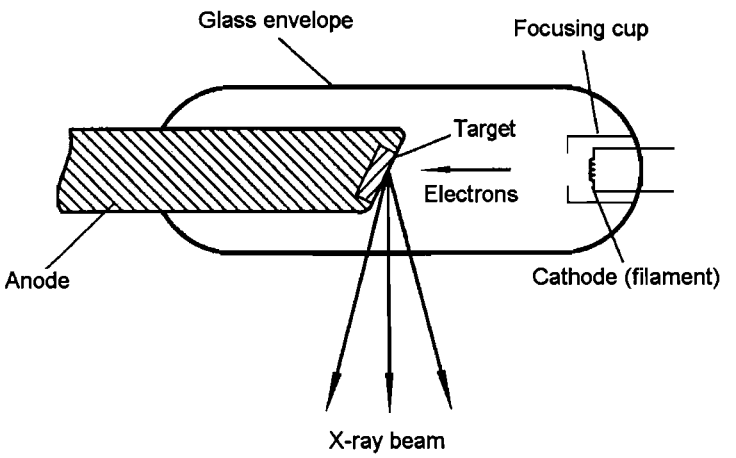

Figure A.1: Schematic diagram of an x-ray Tube (Brown *et al.*, 1999)

A.2 Image intensifier

An image is projected onto the transparent window of a vacuum tube. On the vacuum side of this window is a sensitive layer called the photocathode. Light radiation causes the emission of electrons from the photocathode into the vacuum. These electrons are then accelerated by an applied DC voltage towards a luminescent/phosphor screen situated opposite the photocathode. This screen's phosphor then converts the high energy electrons back to photons which corresponds to the distribution of the input image radiation but with an amplified flux (Siebert, 2002).

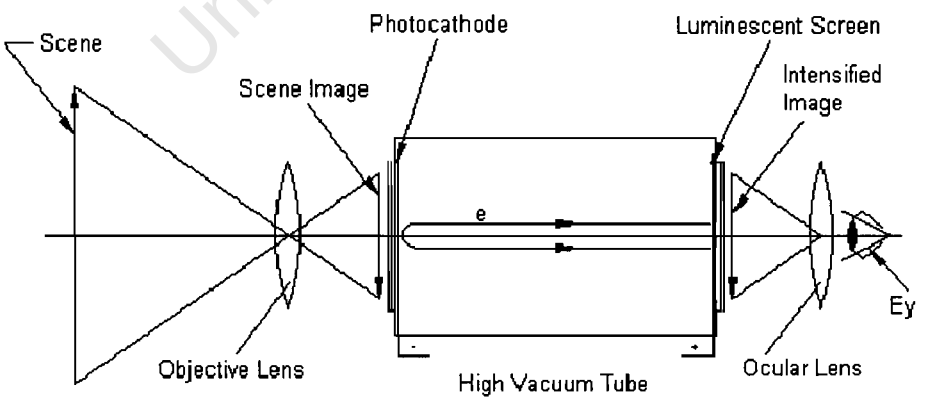

Figure A.2: Schematic diagram of an Image Intensifier

A.3 Scintillators

Scintillators are essentially detectors that convert X-ray energy into visible light. They consist of bulk crystalline alkali hallide materials (activated alkali halides produce light) such as NaI and CsI but also can be made from plastics and gases. These are activated by a small amount of either thallium or sodium impurity. The role of the impurity is to energetically produce luminescent centres between the valence and conduction bands of the host crystal. These materials can be made into large area crystals, have good X-ray stopping power, and are efficient light producers.

Plastics are used almost exclusively as anti-coincidence shields due to their low efficiency in detecting low energy X-rays Hahn *et al.* (2002).

A.4 Computed Radiography (CR)

Computed Radiography (CR) is a capturing process for digital radiographic images. Exposure involves a storage phosphor plate that is placed in a cassette instead of a piece of film. This phosphor plate captures and "stores" the x-rays after which the image is "developed" in a CR reader instead of a film processor. The CR reader extracts the information it finds in the plate to produce a digital image.

CR technology has existed since the early 1980s and has been accepted as a digital image acquisition process that produces images equivalent to conventional x-ray film-screen systems (Lumisys, Inc., 2000).

Appendix B

Time-delayed Integration

To image a field of view larger than the size of the detector it is necessary for the detector to traverse the area of interest in steps. In order to facilitate smoother implementation, a continuous scanning slot detector design is usually appropriate.

Referring to Figure B.1, the charged coupled device (CCD) sensitive area is divided into a matrix of size mxn; only four columns are illustrated in figure B.1 for simplicity. A thin beam of x-rays is allowed to strike the scintillator at a point directly above a pixel (as if the x-rays were forced through a stationary radio-opaque sheet with a very narrow slot, the length of the columns, cut in it) in the first column generating a charge in each pixel in that column. This charge is represented by the narrow block over the first column, in figure B.1, and is proportional to the intensity and the time interval between micro-steps.

Just prior to the detector stepping to the second position, the charges in each pixel of every column are transferred to the neighbouring pixels of the following column in the direction indicated by the arrow in figure B.1 with the charge accumulated in the pixels of the final column (column four), if any, being transferred to the Shift Register (SR) for temporary storage.

The charge created from the detectors new position is then added to the previous charge. At the end of the three such transfers, the charge in the fourth column is four times the original charge and is transferred to the corresponding pixel buffer in the analogue serial register on the proceeding clock pulse.

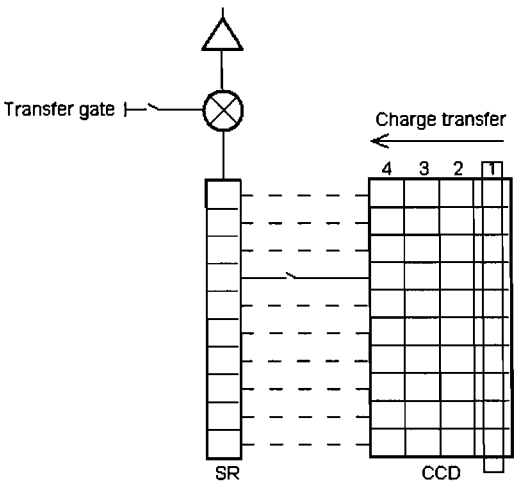

Figure B.1: A simplified schematic of CCDs operating in TDI mode (Tesic *et al.*, 1997)

The contents of the SR thus represent one line of the complete image. Before the next line of transfer into the SR can take place, the charge there must be sent to the CCD chip via the transfer gate and the associated reset switch, where charge-to-voltage conversion takes place. To accomplish this task in time, the SR clocking rate must be at least n times faster, for a CCD with n rows, than the line rate. Control of charge transfer by means of clock voltages allows for pixel size manipulation, i.e. if two column transfers into the SR are allowed before the signal is clocked out of it, the effective pixel size in the scan direction will increase by a factor of two. Similarly, by resetting the transfer gate on alternate SR clock cycles, the pixel size in the transverse direction can be doubled. Utilising both of these features enables the pixel area and the output signal to quadruple in size (Tesic *et al.*, 1997).

Appendix C

Gross Translational Correction Testing

Figure C.1: The image used to test the translation correction of the developed program.

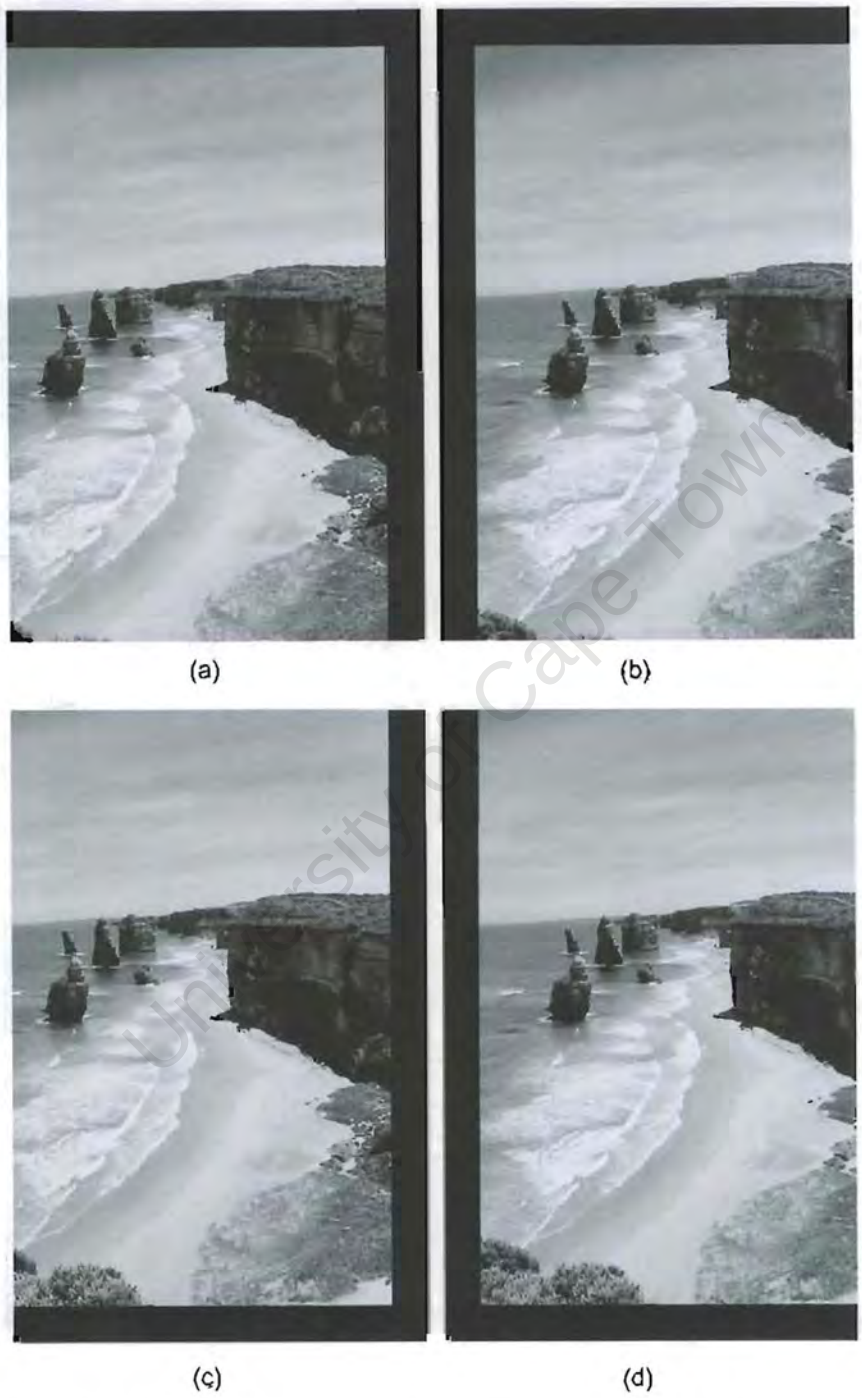

Figure C.2: Linearly shifted images used to test the gross translational shifting section of the program developed for this dissertation. (a) a lower-Left shift (A); (b) a lower-right shift (B); (c) an upper-left shift; (C) and (d) an upper-right shift (D).

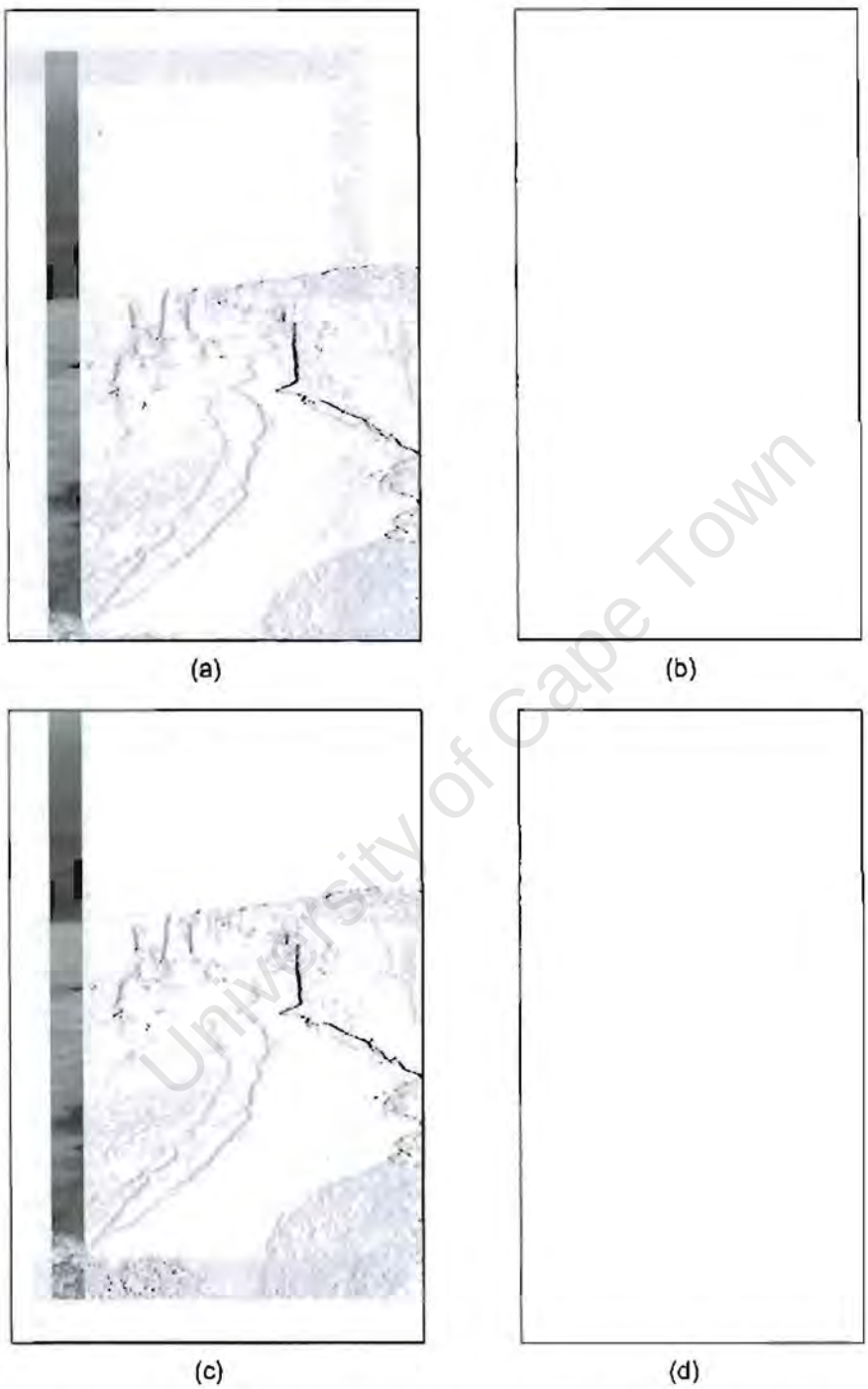

Figure C.3: The subtracted results of different combinations of the shifted images above. The subtraction before linear shifting (left hand side figures) and after linear shifting (right hand side figures (a) and (b) are the results of subtracting image B from A; (c) and (d) are the results of subtracting image D from C; (b) and (d) show the results of perfect alignment i.e. a complete subtraction and therefore no image artefacts.

Figure C.4: The subtracted results of different combinations of the shifted images above. The subtraction before linear shifting (left hand side figures) and after linear shifting (right hand side figures (a) and (b) are the results of subtracting image D from A; (c) and (d) are the results of subtracting image D from B; (b) and (d) show the results of perfect alignment i.e. a complete subtraction and therefore no image artefacts.

Appendix D

Crop Results Using Two Border Widths

D.1 Automatic crop results

D.1.1 T-tube tests

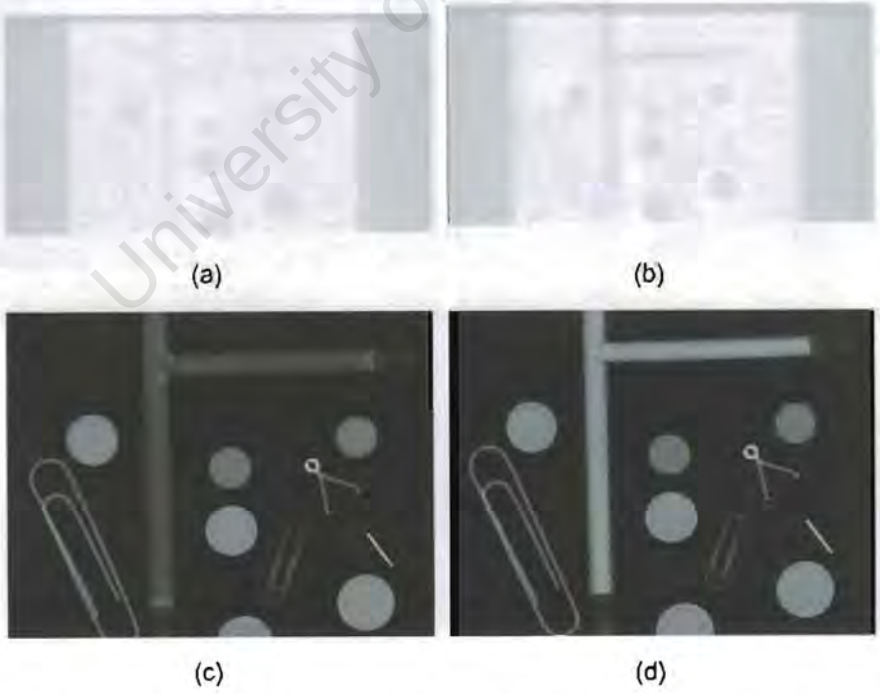

Figure D.1: (a) the mask image of the T-tube phantom directly after a scan; (b) the contrast image of the T-tube phantom obtained from the scan; (c) the T-tube mask image cropped using the automatic cropping function; and (d) the T-tube contrast image cropped using the automatic cropping function.

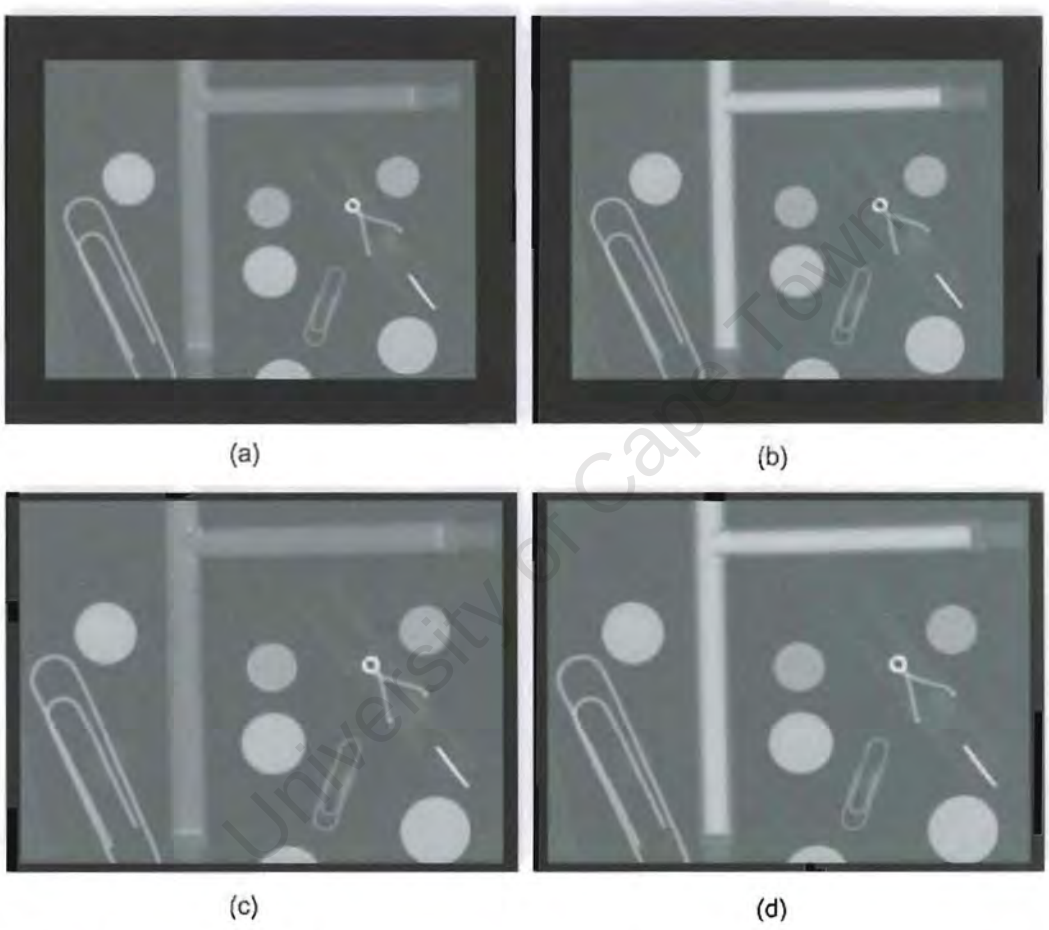

Figure D.2: (a) the automatically cropped T-tube mask image with the broader of two border types; (b) the automatically cropped T-tube contrast image with the broader of two border types; (c) the automatically cropped T-tube mask image with the smaller of two border types; and (d) The automatically cropped T-tube contrast image with the smaller of two border types.

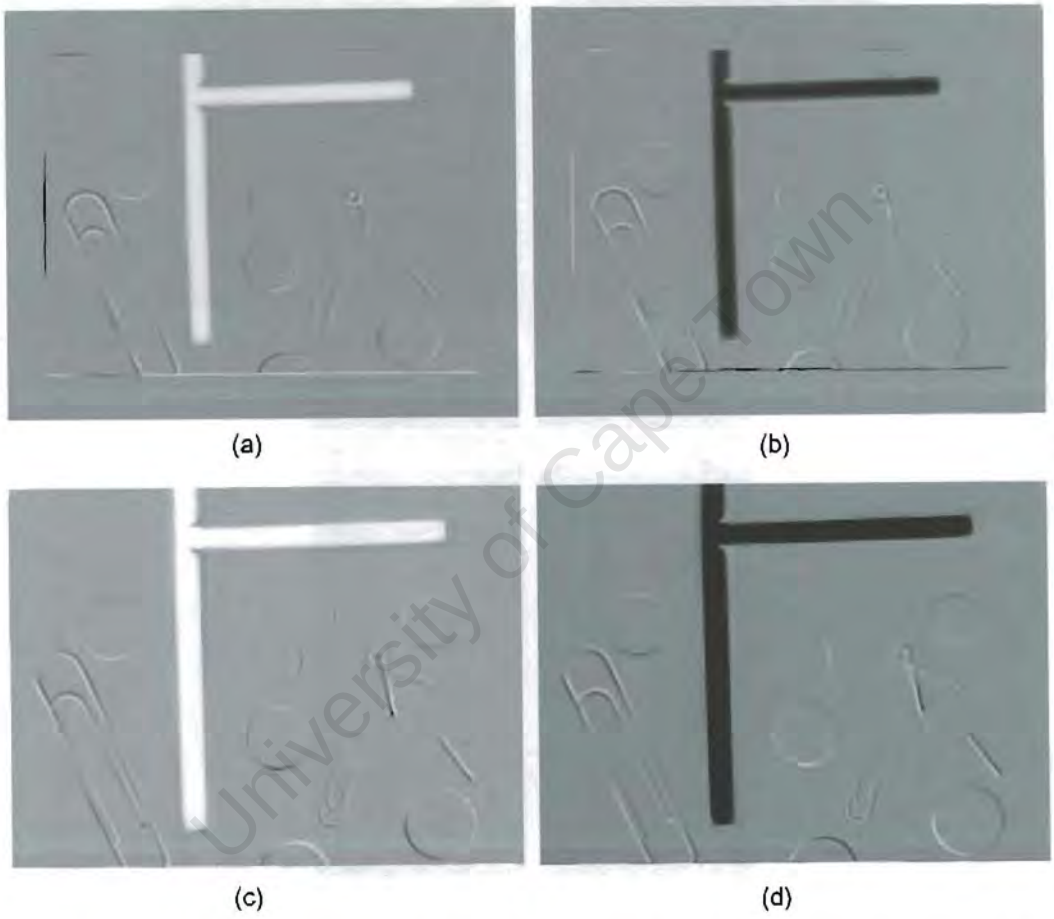

Figure D.3: (a) the automatically cropped T-tube subtracted image of the mask and contrast images that are surrounded by the broader of the two border types; (b) the inverted image of (a); (c) the automatically cropped T-tube subtracted image of the mask and contrast images that are surrounded by the smaller of the two border types; and (d) the inverted image of (c).

D.1.2 Femoral phantom tests

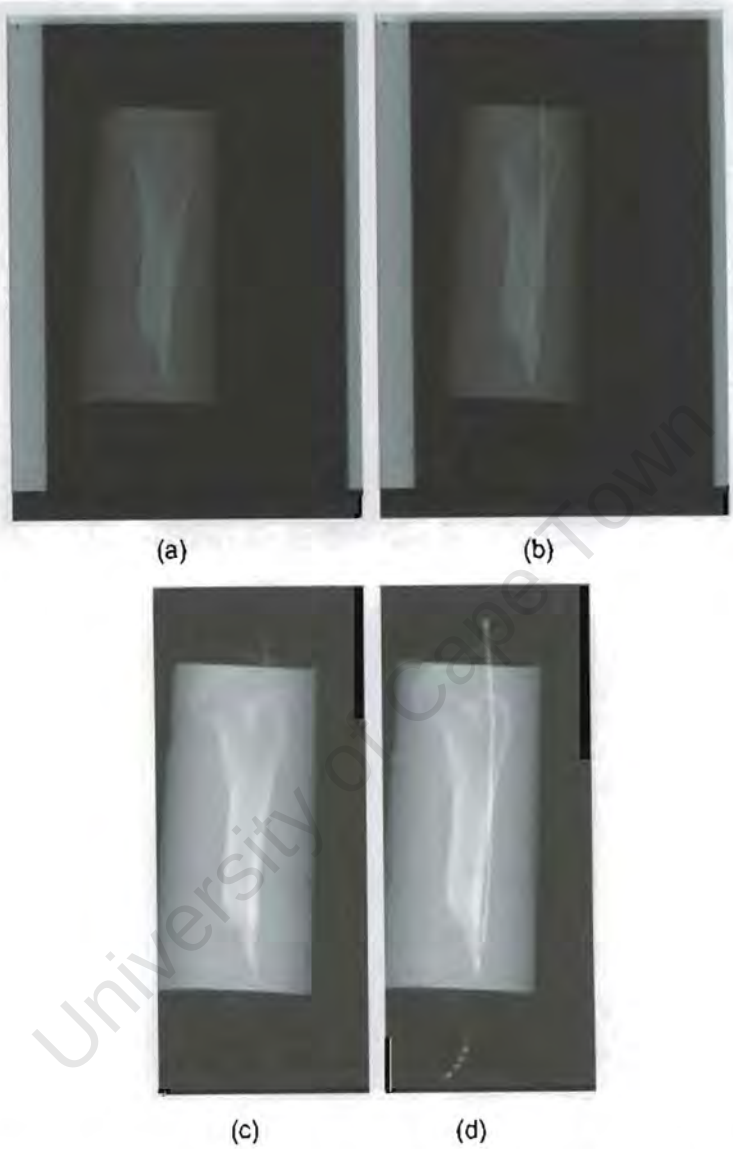

Figure D.4: (a) the mask image of the femoral phantom, directly after a scan; (b) the contrast image of the femoral phantom, obtained from the scan; (c) the femoral mask image cropped using the automatic cropping function; and (d) the femoral contrast image cropped using the automatic cropping function.

Figure D.5: (a) the automatically cropped femoral phantom mask image with the broader of two border types; (b) the automatically cropped femoral phantom contrast image with the broader of two border types; (c) the automatically cropped femoral phantom mask image with the smaller of two border types (d) The automatically cropped femoral phantom contrast image with the smaller of two border types; (e) the automatically cropped femoral phantom subtracted image of the mask and contrast images that are surrounded by the broader of the two border types; (f) the inverted image of (e); (g) the automatically cropped T-tube subtracted image of the mask and contrast images that are surrounded by the smaller of the two border types; and (h) the inverted image of (g).

D.1.3 Patient trial tests

Figure D.6: (a) the mask image from the patient trial, directly after a scan; (b) the contrast image from the patient trial, obtained from the scan; (c) the patient trial mask image cropped using the automatic cropping function; and (d) the patient trial contrast image cropped using the automatic cropping function.

D.2 Manual crop results

D.2.1 T-tube tests

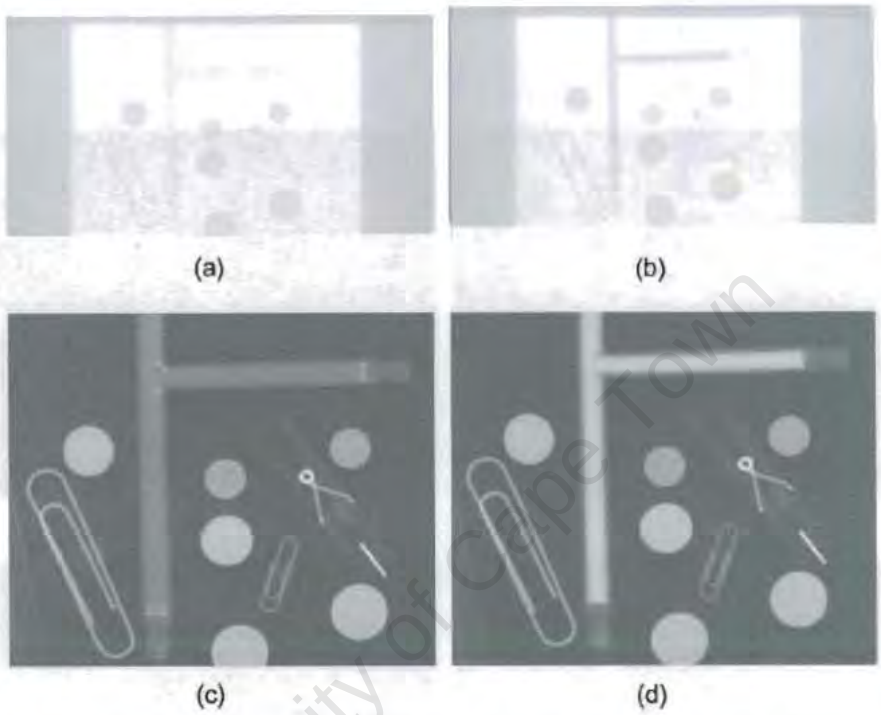

Figure D.7: (a) the mask image of the T-tube phantom directly after a scan; (b) the contrast image of the T-tube phantom obtained from the scan; (c) the T-tube mask image cropped using manual cropping; and (d) the T-tube contrast image cropped using manual cropping.

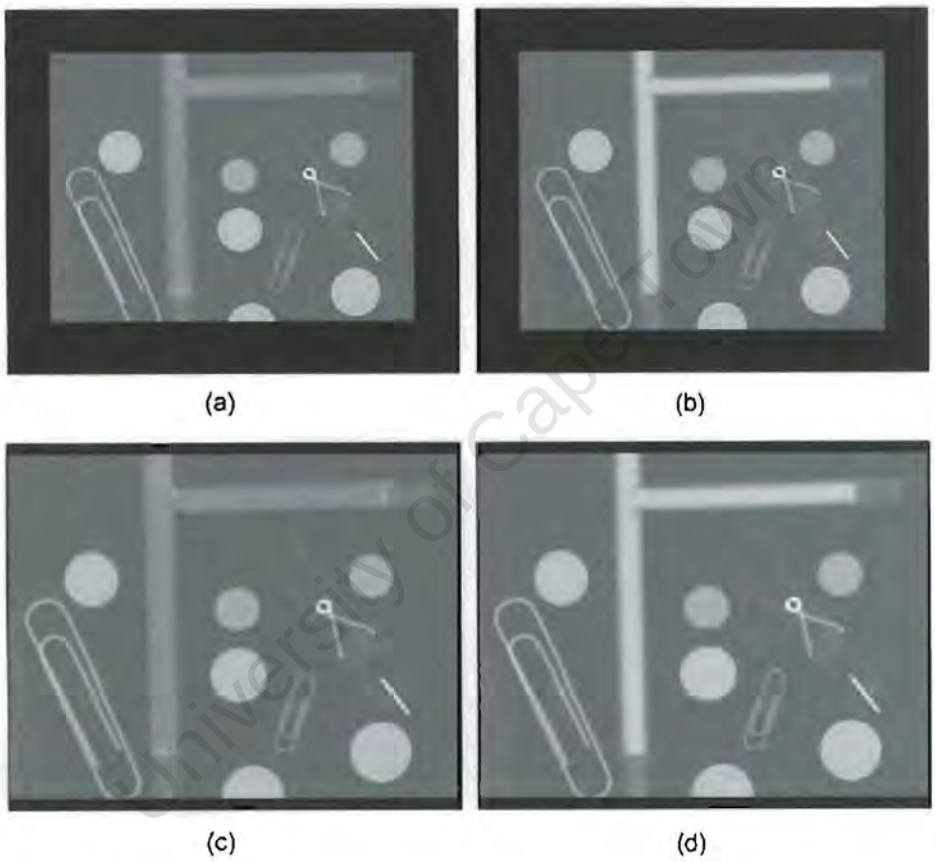

Figure D.8: (a) the manually cropped T-tube mask image with the broader of two border types; (b) the manually cropped T-tube contrast image with the broader of two border types; (c) the manually cropped T-tube mask image with the smaller of two border types; and (d) the manually cropped T-tube contrast image with the smaller of two border types.

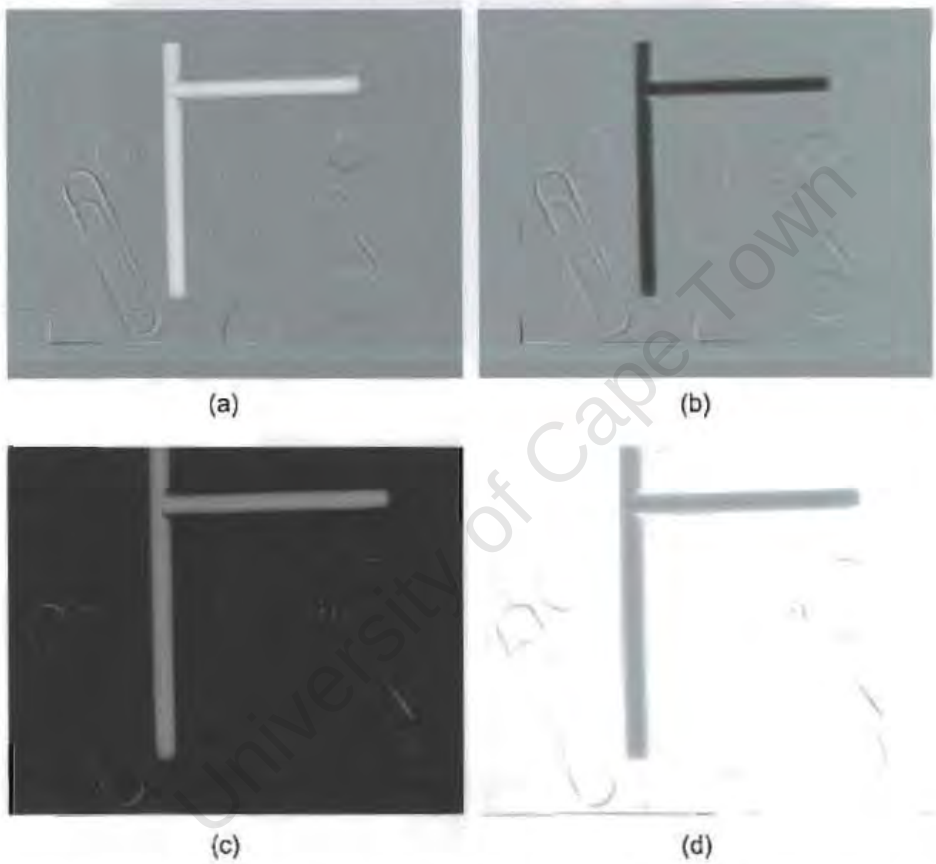

Figure D.9: (a) the manually cropped T-tube subtracted image of the mask and contrast images that are surrounded by the broader of the two border types; (b) the inverted image of (a); (c) the manually cropped T-tube subtracted image of the mask and contrast images that are surrounded by the smaller of the two border types; and (d) the inverted image of (c).

D.2.2 Femoral phantom tests

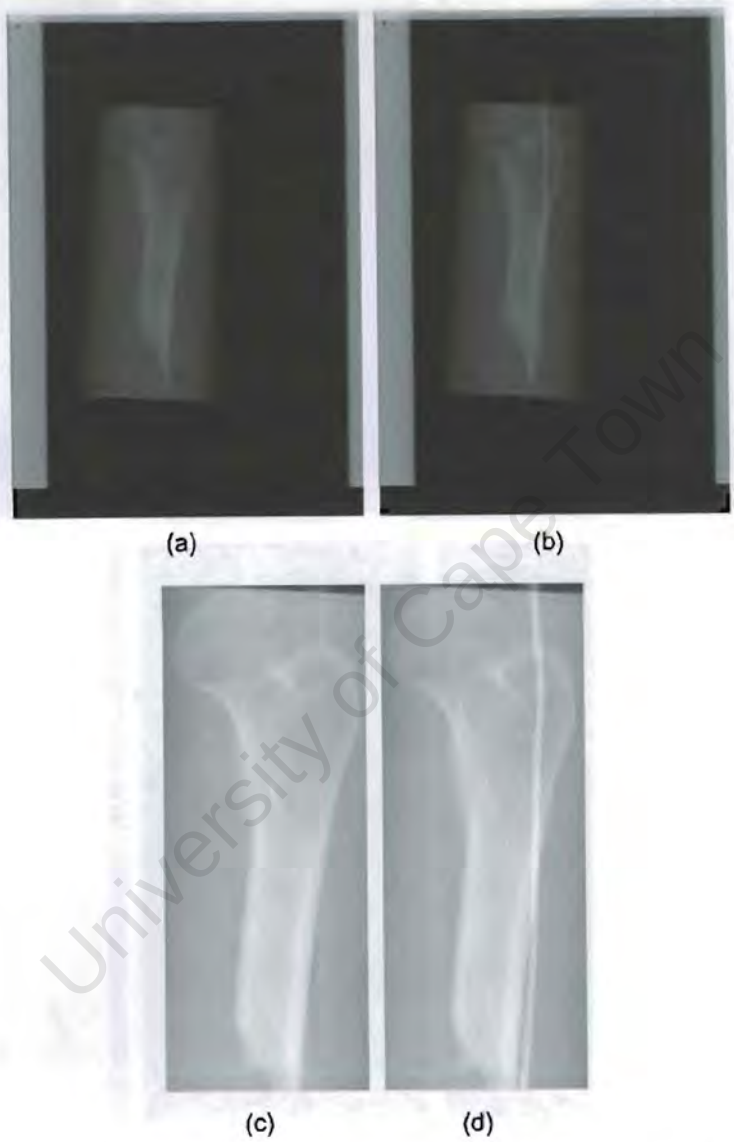

Figure D.10: (a) the mask image of the femoral phantom directly after a scan; (b) the contrast image of the femoral phantom obtained from the scan; (c) the femoral phantom mask image cropped using manual cropping; and (d) the femoral phantom contrast image cropped using manual cropping.

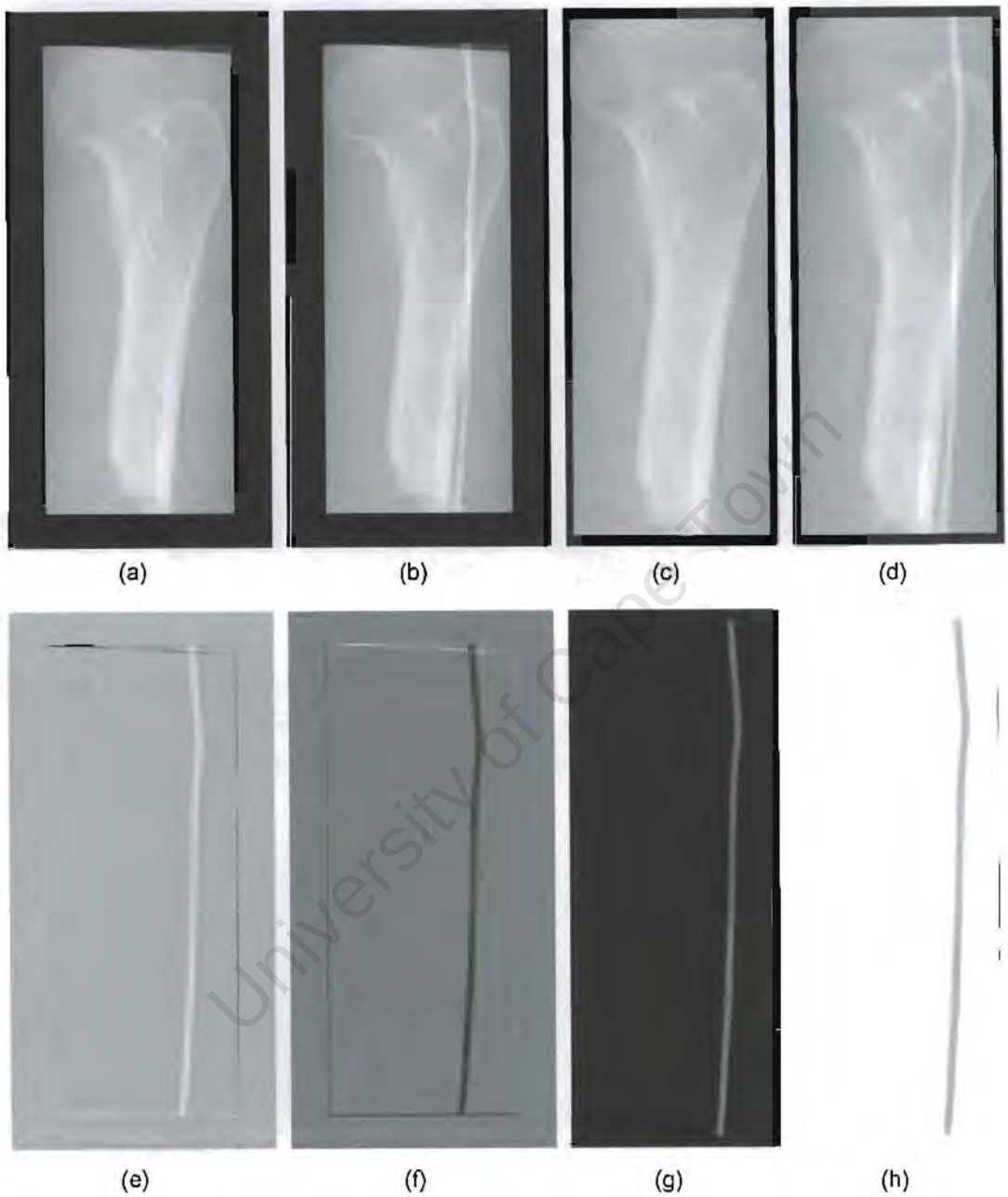

Figure D.11: (a) the manually cropped femoral phantom mask image with the broader of two border types; (b) the manually cropped femoral phantom contrast image with the broader of two border types; (c) the manually cropped femoral phantom mask image with the smaller of two border types; (d) the manually cropped femoral phantom contrast image with the smaller of two border types; (e) the manually cropped femoral phantom subtracted image of the mask and contrast images that are surrounded by the broader of the two border types; (f) the inverted image of (e); (g) the manually cropped femoral phantom subtracted image of the mask and contrast images that are surrounded by the smaller of the two border types; and (h) The inverted image of (g).

D.2.3 Patient Trial tests

(a) (b) (c) (d)

Figure D.12: (a) the mask image from the patient trial, directly after a scan; (b) the contrast image from the patient trial, obtained from the scan; (c) the patient trial mask image cropped using manual cropping; and (d) the patient trial contrast image cropped using manual cropping.

Figure D.13: (a) the manually cropped patient trial mask image with the broader of two border types; (b) the manually cropped patient trial contrast image with the broader of two border types; (c) the manually cropped patient trial mask image with the smaller of two border types; (d) the manually cropped patient trial contrast image with the smaller of two border types; (e) the manually cropped patient trial subtracted image of the mask and contrast images that are surrounded by the broader of the two border types; (f) the inverted image of (e); (g) the manually cropped patient trial subtracted image of the mask and contrast images that are surrounded by the smaller of the two border types; and (h) the inverted image of (g).

Table D.1: Table summarising the timing of the running of each program

TEST		CROPPED MATRIX SIZE			TIME TAKEN		
	MATRIX SIZE	**AUTOMATIC CROP**	**MANUAL CROP**	**Difference**	**AUTOMATIC CROP**	**MANUAL CROP**	**Difference**
T-tube Phantom	896 x 1598						
BROADBORDER		816 x 1020	867 x 1071	51 x (51)	01 min 34 sec	01min 54 sec	00 min 20 sec
NARROWBORDER		640 x 863	732 x 879	(92) x (16)	01 min 13 sec	01min 08 sec	00 min 05 sec
Difference		176 x 157	135 x 192		00 min 21 sec	00 min 46 sec	
Femoral Phantom	2304 x 1600						
BROADBORDER		2244 x 1020	1275 x 612	969 x 408	08 min 03 sec	01 min 22 sec	06 min 41 sec
NARROWBORDER		2090 x 861	1118 x 447	972 x 414	07 min 00 sec	00 min 50 sec	06 min 10 sec
Difference		154 x 159	157 x 165		01 min 03 sec	00 min 32 sec	
Patient Trial	3712 x 956						
BROADBORDER		-	1887 x 765	-	-	04 min 03 sec	-
NARROWBORDER		-	1734 x 639	-	-	02 min 41 sec	-
Difference		-	153 x 126	-	-	01 min 22 sec	-

Appendix E

MTF curves for Lodox

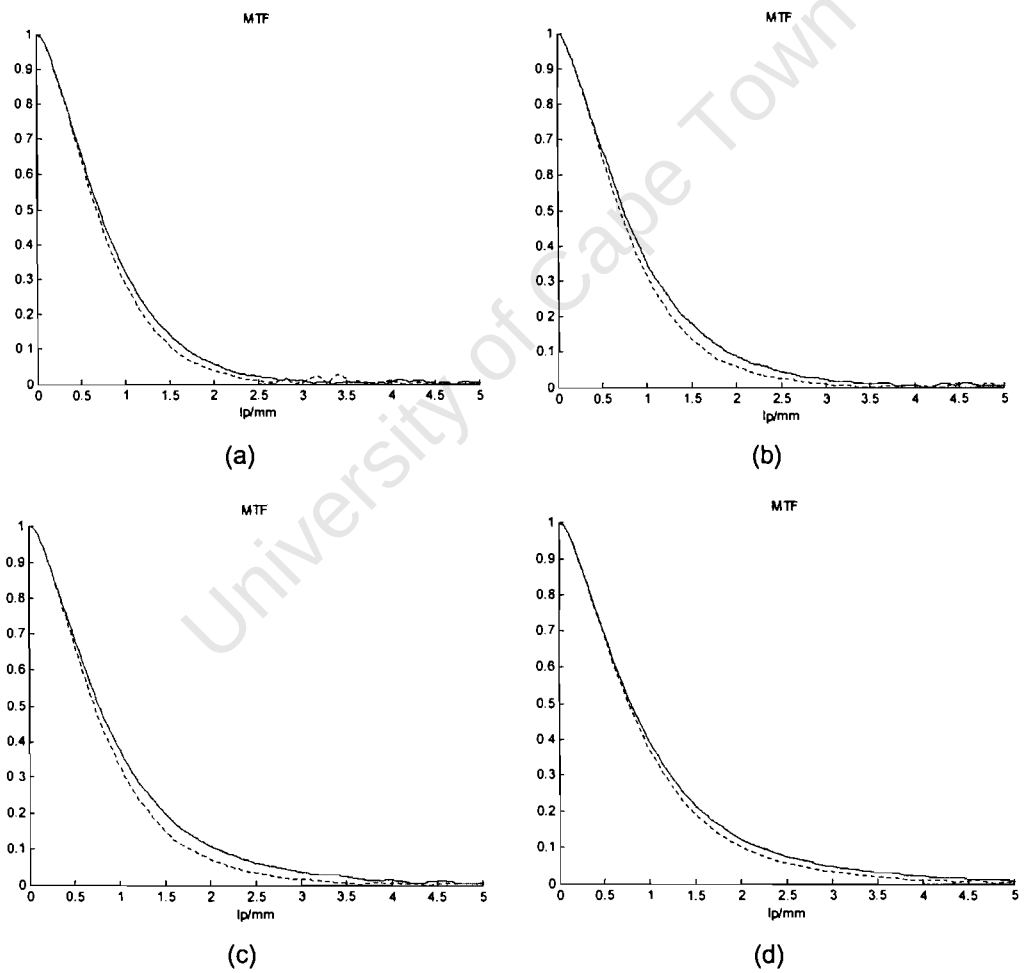

Figure E.1: MTF value graphs for Lodox at the various modes. The dotted line indicates values obtained in the scanning direction (along the length of the trolley) while the solid line indicates measurements obtained at right angles to this. (a) normal mode (5x5 binning); (b) high mode (3x3 binning); (c) ultra-high mode (2x2 binning); and (d) test mode (1x1 binning) (de Villiers and de Jager, 2002)

Appendix F

Case Report Study

Emergency Room Arteriogram with a New Trauma Digital X-ray machine [Lodox]: A Case Report

By: Andrew J. Nicol, PCS [SA], Steve J Beningfield, F.F.Rad [D] SA, Pradeep Navsaria, PCS [SA] and Rene Zellweger, MD.

Keywords: Digital radiography, Emergency room arteriogram, Arteriography, Lodox, Popliteal artery.

INTRODUCTION

An emergency room arteriogram [ERA] can be a simple, accurate and cost effective technique for the examination of patients with likelihood of a lower extremity vascular injury after trauma O'Gorman *et al.* (1984); Itani *et al.* (1992); MacFarlane *et al.* (1989). The ERA is typically performed by the emergency unit staff without a vascular radiologist and the need to transport the patient to an angiography suite. Conventional single exposure radiographs are, however, limited to the site of potential injury, with usually no or little information regarding the status of the distal vasculature. A new trauma digital X -ray machine, Lodox [Lodox(Pty)Ltd, Industrial Development

Corporation, Johannesburg, South Africa] has been developed. Lodox consists of an X-ray tube mounted on a C-arm, which emits a low dose fan beam. An X -ray detector unit is sited on the other end of the C-arm comprising scintillator arrays linked to charge coupled devices. An image is taken by scanning the C-arm over the required anatomical portion of the patient whilst continually reading the output of the detectors (Figure 8.2). The C-arm travels at speeds of up to 14 cm per second and allows for the rapid acquisition of X-rays of parts or all of the body. The mean digital radiation dose is typically 6% that of a conventional X-ray (Beningfield *et al.*, In press) The X-ray image is displayed on a computer controlled operating and viewing system with standard DICOM 3 (digital imaging and communication in medicine 3) capability. We report the use of the Lodox machine to obtain an emergency room angiogram in a patient with an acute arterial injury.

CASE REPORT

A 43 year-old man was admitted to the Groote Schuur Hospital Trauma Centre after having been stabbed in the left thigh two days earlier. On arrival he was noted to be fully conscious with a blood pressure of 127/72 mmHg, a pulse rate of 107 beats per minute, and a hemoglobin of 8.5 g%. The secondary survey revealed an incised 3 cm wound over the medial aspect of the left thigh. The limb was cool but with normal sensation and motor function. No pulses were palpable below the femoral pulse on the left side. The tip of the left 1st toe revealed an area of cutaneous gangrene suggestive of an embolic phenomenon. The pulses in the right leg were present and normal. An emergency room arteriogram was performed using the Lodox machine. The patient was placed supine on the table and an 18-gauge plastic intravenous cannula was inserted retrograde into the common femoral artery by direct puncture. A drip extension set was securely attached to the cannula so as to keep the operators hands away from the area to be visualised. Thirty ml of a non-ionic water-soluble iodinated contrast medium [Ultravist 300, Schering (Pty) Ltd, Berlin, Germany] was rapidly injected by hand intra-arterially. The Lodox machine was activated to image the left limb when almost all the contrast had been injected. A digital computerised image of the arterial system of the limb appeared within 10 seconds (Figure 8.11(a)). This revealed an intimal injury to a segment of the above- knee popliteal artery. With the Lodox unit

areas of concern may be magnified. The area of the trifurcation showed a cut- off of the anterior tibial and peroneal arteries, with a patent posterior tibial artery (Figure 8.13). The time taken to perform the angiogram was in the region of 10 minutes and did not result in any major delay in the patient being taken to surgery.

The patient was taken to theatre for a popliteal artery and trifurcation exploration. He was found to have a through-and-through stab wound to the above-knee popliteal artery. The injured segment was excised and a primary anastomosis performed. The trifurcation exploration revealed clot in both the anterior tibial and peroneal arteries. This was removed with an arterial embolectomy catheter. Intraoperative doppler signals were present in the both the anterior and posterior tibial arteries in the left foot at the end of the procedure. The patient's subsequent course was uncomplicated and the patient was discharged home three days post-operative. His follow up visit two weeks later revealed good foot pulses in the left foot, with an ankle brachial index of 1.

DISCUSSION

The Lodox machine is situated in our resuscitation room and provides partial and whole body digital X-rays of trauma patients in an efficient and timeous manner. The fact that the C-arm moves down the patient whilst scanning has made us aware of the potential for performing ERA. The C-arm may also be rotated through 90 degrees for oblique or lateral X-rays. The entire limb can be acquired in a single high quality angiogram without "stitching" of individual images. ERA provides a very quick and effective means of identifying the site of the injury. Itani *et al.* (1992) have shown that the sensitivity and specificity of conventional emergency arteriography to be 95.5 % and 97.7 % respectively. The only problem with ERA using conventional X-rays is that the entire limb cannot be visualised in one exposure and repeat films may have to be performed to identify specific areas of concern.

The Lodox ERA has the potential use in patients with arterial trauma as a "road map" to plan surgery. This is obviously not an appropriate procedure in patients who present with massive bleeding or a rapidly expanding hematoma, but is useful in patients with hard signs of an arterial injury, including absent pulses, a bruit or a

threatened limb. Patients with diminished pulses, and shotgun injuries with a viable limb, have formal angiography performed in the vascular suite. In our experience intra-operative arteriography is far more time consuming than ERA. This case report illustrates the usefulness of Lodox in being able to generate digital angiographic images of high quality. In this case the operative strategy was altered as a result of the Lodox ERA to include a trifurcation exploration.

References

Allard, D., 2003. Radiation basics.
URL http://www.hps.org/publicinformation/ate/q1055.html

Ashburner, J., Friston, K., 2001. Spatial transformation of images , 2–35.

Baum, E., Speidel, J., 2000. Novel video coding scheme using adaptive mesh based interpolation and node tracking. Institute of Telecommunications, University of Stuttgart.
URL http://www.inue.uni-stuttgart.de/publications/pub_2000/baum_Tagung-Austral_Video-Coding.pdf

Beningfield, S., Potgieter, H., Nicol, A., In press. Report on a new type of trauma full-body digital x-ray machine. *Emergency Radiology* .

Beningfield, S., Potgieter, J., Shackleton, M., Hering, E., de Jager, G., Bowie, G., Marshall, M., Cox, G., Pagliari, G., Coetzee, N., 1999. Evaluation of a new type of direct digital radiography machine. *South African Medical Journal* 89 (11), 1182–1188.

Brody, W., Butt, G., Hall, A., Macovski, A., 1981a. A method for selective tissue and bone visualisation usind dual energy scanned projection radiography. *Medical Physics* 8 (3), 353–357.

Brody, W., Enzman, D., Deutsch, L., 1981b. Intravenous carotid arteriography using line scanned digital radiography. *Radiology* 139, 297–300.

Brown, B., Smallwood, R., Barber, D., Lawford, P., Hose, D., 1999. *Medical Physics and Biomedical Engineering*. Medical Science Series, Institute of Physics Publishing, 1st ed.

Buonocore, E., Pavlicek, W., Modic, M., Meaney, T., O'Donovan, P., Moodie, L. G. N. D., Yiannikas, J., 1983. Anatomic and functional imaging of congenital heart disease with digital subtraction angiography. *Radiology* 147, 647–654.

Buzug, T., Weese, J., Strasters, K., 1998. Motion detection and motion compensation for digital subtraction angiography image enhancement. *Philips Journal of Research* 51 (2), 203–229.

Campbell, F., Robson, J., 1968. Application of fourier analysis to the visibility of gratings. *Journal of Physiology (London)* Image Courtesy of Izumi Ohzawa, Ph.D. University of California School of Optometry from The Internet site of the John Moran Eye Center, Department of Ophthalmology at the University of Utah. http://insight.med.utah.edu/Webvision/.

Chiang, J., Sullivan, B., 1993. Coincedent bit counting a new criterion for image registration. *IEEE Transactions on Medical Imaging* 12 (1), 30–37.

Cohen, G., Wagner, L., Rauschkolb, E., 1982. Evaluation of a digital subtraction angiography unit. *Radiology* 144 (3), 613–617.

Cox, G., 2000. *Designing Hypothesis Tests for Digital Image Matching*. Ph.D. thesis, University of Cape Town, South Africa.

Cox, G., de Jager, G., 1994. Automatic registration of temporal image pairs for digital subtraction angiography. *SPIE Image Processing* 2167, 188–199.

Crummy, A., Strother, C., Sackett, J., Ergun, D., Shaw, C., Kruger, R., Mistretta, C., Turnipseed, W., Lieberman, R., Myerowitz, P., Ruzicka, F., 1980. Computerized fluoroscopy: Digital subtraction for intravenous angiocardiography and arteriography. *The American Journal of Physiology* 135, 1131–1140.

De Beers, 2001. Lodox Workshop.

de Villiers, M., de Jager, G., 2002. *Determination of the Detective Quantum Efficiency of the Lodox System version 6*. Tech. rep., for Lodox (Pty)Ltd.

den Boer, A., de Feijter, P., Hummel, W., Hoornaert, B., Kroon, J., 2002. *Integris: DoseWise Additional beam filtering in Cardiac fluoroscopy*. Tech. rep., Philips Medical Systems Nederland B.V.

Dougherty, L., Asmuth, J., Blom, A., Axel, L., Kumar, R., 1999. Validation of an optical flow method for tag displacement estimation. *IEEE Transactions on Medical Imaging* 18 (4), 359–363.

Douglas, T., Solomondis, S., Sandham, W., Spence, W., 2002. Ultrasound image matching using genetic algorithms. *Medical and Biological Engineering and Computing* 40, 168–172.

ECRI, 2001. Digital imaging systems angiographic/cardiovascular. *Healthcare Product Comparison System* , 1–33.

Fitzpatrick, J., 1988. The existence of geometrical density-image transformations corresponding to object motion. *Computer Vision Graphics and Image Processing* 44 (2), 155–174.

Flash, G., 2002. *Dose Readings for the Lodox System*. Tech. rep., Lodox (Pty)Ltd.

Gaines, P., 2001. Emergency vascular radiology. *The British Institute of Radiology* 13 (2), 79–88.

GE Medical Systems, 2003. Dose.
URL `http://www.gemedicalsystems.com/rad/xr/education/dose.html`

Goodman, P., 2002. A century of radiology.
URL `http://www.xray.hmc.psu.edu/rci/ss1/ss1-4.html`

Goshtasby, A., Stockman, G., Page, C., 1986. A region based approach to digital image registration with subpixel accuracy. *IEEE Transactions on Geoscience and Remote Sensing* GE-24 (3), 392–397.

Hahn, G., Hupke, R., Kohl, G., Leppert, J., 2002. Developing an ultrafast radiation detector for CT scanning.
URL `http://w4.siemens.de/FuI/en/archiv/zeitschrift/heft1_97/artikel03/`

Harrington, D., 1982. Digital subtraction angiography. *The American Journal of Physiology* 139, 781–786.

Hauschild, R., 2002. Personal correspondent - Toshiba.

Hemmendorff, M., Knutsson, H., Andersson, M., Kronander, T., 1999. Motion compensated digital subtraction angiography. *SPIE Image Processing* , 3661–148.

Hering, E., 1990. Radiography physics and equipment. Groote Schuur hospital, University of Cape Town, South Africa.

Hering, E., Maree, G., 2003. *DOSE SURVEY: StatScan LODOX*. Tech. Rep. Serial number: LDX 89001, Groote Schuur Hospital, Cape Town.

Hinz, M., Toennies, K., Grohmann, M., Pohle, R., 2002. Active double-contour for segmentation of vessels in digital subtraction angiography.
URL http://isgwww.cs.uni-magdeburg.de/bv/pub/pdf/spie2001paper_revision.pdf

Itani, K., Burch, J., Spjut-patrinely, V., Richardson, R., Martin, R., Mattox, K., 1992. Emergency center arteriography. *The Journal of Trauma* 32 (3), 302–307.

Kaut-Roth, C., Faulkner, W., 2002. Equipment.
URL http://www.t2star.com/angio/Neuro3.htm#Equipment

Lancaster, J., 2003. Physics of medical x-ray imaging.
URL http://ric.uthscsa.edu/personalpages/lancaste/DI-II_chapters/

Lease, A., 2001. *Feasibility of Using Lodox Technology for Mammography*. Master's thesis, University of Cape Town, South Africa.

Lehmann, L., Alvarez, R., Macovski, A., Brody, W., 1981. Generalised image combinations in dual kvp digital radiography. *Medical Physics* 8 (5), 659–667.

Lodox Systems, 2002.
URL http://www.lodox.com

Lodox Systems (Pty) Ltd, 2003. Lodox statscanner product specification. document number:Q02-200000-756.

Lumisys, Inc., 2000. Technical references.
URL http://www1.lumisys.com/support/techref/crfaqNew.html

MacFarlane, C., Boffard, K., Saadia, R., Wilkinson, A., 1989. Emergency room arteriography: a useful technique in the assessment of peripheral vascular injuries. *Journal of Royal College of Surgeons Edinbrough* 34, 310–313.

Maes, F., Collignon, A., Vandermeulen, D., Marchal, G., Suetens, P., 1997. Multimodality image registration by maximisation of mutual information. *IEEE Transactions on medical imaging* 16 (2), 187–198.

Maintz, J., Viergever, M., 1998. A survey of medical image registration. *Medical Image Analysis* 2 (1), 1–37.

Meijering, E., 1999. A fast technique for motion correction in digital subtraction angiography.
URL www.isi.uu.nl/research/sequence/sequence-project.html

Meijering, E., 2000. *Image Enhancement in Digital X-Ray Angiography*. Ph.D. thesis, Utrecht University.

Meijering, E., 2001. Reduction of patient motion artefacts in digital subtraction angiography evaluation of a fast and fully automatic technique.
URL www.radiology.rsnajnls.org/cgo/content/abstract/219/1/288maxtoshow

Meijering, E., Niessen, W., Viergever, M., 1999. Retrospective motion correction in digital subtraction angiography a review. *IEEE Transactions on Medical Imaging* 18 (1), 2–19.

Milnor, W., 1989. *Hemodynamics*. Williams & Wilkins, 2nd ed.

Nicer, 2003. The encyclopaedia of medical imaging.
URL http://www.amershamhealth.com/medcyclopaedia/

Nicol, A., 2002. Personal correspondent - trauma head of department.

Norton, J., Bollinger, R., Chang, A., Lowry, S., Mulvihill, S., Pass, H., Thompson, R. (Eds.), 2001. *Surgery. Basic science and clinical evidence*. Springer-Verlag New York Inc.

O'Gorman, R., Feliciano, D., Bitondo, C., Mattox, K., Burch, J., Jordan, G., 1984. Emergency center arteriography in the evaluation of suspected peripheral vascular injuries. *Archives of Surgery* 119, 568–573.

Ovitt, T., Christenson, P., Fisher, H., Frost, M., Nudelman, S., Roehrig, H., Seeley, G., 1980. Intravenous angiography using digital video subtraction : X-ray imaging system. *American Journal of Radiology* 135, 1141–1144.

Philips Medical Systems, 1989. *DVI Student Manual 1 & 2*. Philips Medical Systems.

Philips Medical Systems, 2002a. Cardio vascular x-ray Integris Allura.
URL http://www.medical.philips.com

Philips Medical Systems, 2002b. Philips specifications document for the Ingeris Allura.

Robb, G., Steinberg, I., 1939. Visualisation of the chambers of the heart, the pulmonary circulation and the great blood vessels in man. *American Journal of Radiology* 41, 1–17. Citing Crummy, A., Strother, C., Sackett, j., Ergun, D., Shaw, C., Kruger, R., Mistretta, C., Turnipseed, W., Lieberman R., Myerowitz, P., Ruzicka, F., 1980. Computerized Fluoroscopy: Digital Subtraction for intravenous Angiocardiography and Arteriography. *The American Journal of Physiology* 135, 1131-1140.

Rutherford, R., Johnson, G., Johnston, K., Kempczinski, R., Krupski, W., Moore, W., Perry, M., Comerota, A., Dean, R., Glovicski, P., Johansen, K., Riles, T., Sumner, D., Taylor, L. (Eds.), 1995. *Vascular Surgery*, vol. 1. WB Saunders Company, 4th ed.

Schindehutte, M., Morris, M., Singhal, A., Bolg, M., 1998. *Strategic Assessment of the Market Opportunity for Lodox in Trauma Centers in the USA*. Tech. rep. Confidential study completed for De Beers, Johannesburg, South Africa, 173 pages.

Shackford, S. R., Rich, N. H., 1996. *Trauma*, Appleton & Lange, vol. III, chap. 43 Management in specific injuries. pp. 1011–1046.

Siebert, M., 2002. Introduction to image intensifier tubes.
URL `http://www.akzent-optronic.de/prod/bv/eein.htm`

Skinner, D., Whimster, F. (Eds.), 1999. *Trauma: A companion to Bailey and Love's short practice of surgery*. Arnold.

Smith, S., 1999. *The scientist and engineer's guide to digital signal processing*. California Technical Publishing, 2nd ed.

Sprawls, P., 1977. *The physical principles of diagnostic radiology*. Baltimore : University Park Press.

Sprawls, P., 2002. Evaluating digital radiographic detail (blurring) with a contrast-detail phantom.
URL `http://www.emory.edu/X-RAYS/Sprawls/technology/detail.htm`

Stremler, F., 1990. *Introduction to communication Systems*. Addison Wesley, 3rd ed.

Tangkuampien, J., 2001. Development of registration and subtraction algorithm for chest x-rays images. Undergraduate electrical engineering thesis from the University of Cape Town, South Africa.

Tesic, M., Piccaro, M. F., Munier, B., 1997. Full field digital mammography scanner. *European Journal of Radiography* 31, 2–17.

Toshiba, 1995. Interventional angiography system, Infinix VC, product brochure.

Toshiba, 1999. Interventional angiography system, Infinix VC, systems data.

Tremp, P., 2002. Personal correspondent - Philips.

Trevert, E., 2001. The x-ray century.
URL `http://www.emory.edu/X-RAYS/century.htm`

van Rooyen, T., 2001. *The Science of Radiation Protection.* Tech. rep., Radiation Safety Division - National Accelerator Centre, South Africa.

Venot, A., Devaux, J., Herbin, M., Lebruchec, J., Dubertret, L., Raulo, Y., Roucayrol, J., 1998. An automated system for the registration and comparison of photographic images in medicine. *IEEE Transactions on Medical Imaging* 7 (4), 299–303.

Venot, A., Leclerc, V., 1984. Automated correction of patient motion and gray values prior to subtraction in digitized angiography. *IEEE Transactions on Medical Imaging* MI-3 (4), 179–187.

Viola, P., Wells III, W., 1995. Alignment by maximisation of mutual information. *International conference on Computer Vision* , 16–23Citing Cox, GS., 2000. Designing Hypothesis Tests for Digital Image Matching. PhD from the University of Cape Town, South Africa.

Watson, D., 1981. Computing the n-dimaneional delaunay tessellation with application to voronoi polytopes. *The Computer Journal* 24 (2), 167–172.

Zuiderveld, K., ter Haar Romeny, B., ten Hove, W., 1992. Fast techniques for automatic pixel shift and rubber sheet masking in digital subtraction angiography. In: A. Todd-Pokropek, M. Viergever (Eds.), *Medical Images: Formation, Handling and Evaluation*, Springer-Verlag, Berlin, Germany, vol. 98 of *NATO ASI Series F: Computer and Systems Sciences*, pp. 667–685, pp. 667–685. Citing Meijering,

E., 2000.*Image Enhancement in Digital X-Ray Angiography*. Ph.D. thesis, Utrecht University and Puentes, J., Roux, C., Garreau,M., Coatrieux, JL., 1998. Dynamic Feature Extraction of Coronary Artery Motion Using DSA Image Sequences. *IEEE Transactions on Medical Imaging* 17 (6), 857-871.